Single mode optical fiber based devices and systems for mid-infrared light generation, communication and metrology

by

Ojas P. Kulkarni

A dissertation submitted in partial fulfillment
of the requirements for the degree of
Doctor of Philosophy
(Electrical Engineering)
in The University of Michigan
2011

Doctoral Committee:

Professor Mohammed N. Islam, Chair
Professor Fred L. Terry, Jr.
Professor Michael J. Welsh
Professor Herbert G. Winful

To my parents – *Mrs. Prachi* and *Mr. Prashant Kulkarni*

ACKNOWLEDGEMENTS

First of all, I would like to thank my research advisor, Prof. Mohammed N. Islam, for giving me the opportunity to pursue my Ph.D. in his group. Over the years, he has given me his precious time guiding me in my research. His insight and intuition in conducting research has helped me immensely in achieving my goals. Through his mentoring, I have developed many valuable skills in problem-solving and communication, which I can benefit from throughout my life.

I would also like to thank my committee members, Prof. Terry, Prof. Welsh and Prof. Winful for their advice and inputs in the conference room as well as in the class room.

A large part of my day-to-day interactions in the lab have revolved around some wonderful colleagues and now friends: Vinay Alexander, Malay Kumar, Chenan Xia, Zhao Xu, Jeremiah Mauricio, Xiuquan Ma, Dong-Joon Lee. I really appreciate the advice and inputs you provided and will always cherish the lighter moments we shared to be able to enjoy my time during my doctoral research. I would like to take this opportunity to wish them all the very best for their future endeavors.

A special mention is needed of Dr. Michael J. Freeman of OmniSciences, Inc. for providing immensely fruitful discussions regarding experiments. His expertise in Optics and Electronics was instrumental is successfully designing and carrying out experiments.

I would like to thank the funding agencies, Tellabs, Inc., Coherix, Inc, and OmniSciences, Inc. for financially supporting me and my experiments during the course of my doctoral studies. I would also like to thank the staff of Lurie Nanofabrication facility, particularly Brian Vander Elzen, for their help during the clean-room processing.

I have also made life-long friends during my stay in the wonderful city of Ann Arbor whom I would like to thank for providing great company through these years: Akshay Sheorey, Shaun D'Souza, Sakina Zabuawala, Pari and Sulabh Dhanuka, Tushar Bansal, Alok Jain, Rushali Parikh, Saumil Shah, James Easter, Nidhi Kumar and Yusuf Murgha. Also my friends from back home in India, Hrishikesh Raje, Bhushan Dabir, Nithin Johnson, Vidya Ramachandran and Devendra Naik, who have inspired me over the years with their achievements and success.

Finally, I would like to thank my family members, who have whole-heartedly supported me in all my pursuits, both academic and personal, throughout my life. My parents, Prachi and Prashant Kulkarni, and my sister, Prajakta, have been unwavering in their trust and confidence in my abilities and for that I am very grateful. Last but not the least, my grandparents, Pratibha and Kalidas Kulkarni, have showered me with their love and blessings that has pushed me to always remember to be a humble human being.

TABLE OF CONTENTS

LIST OF FIGURES

Figure

LIST OF TABLES

Table

Chapter I

Introduction

The invention of light guiding by refraction dates all the way back to 1840s and was first demonstrated by Daniel Colladon and Jacques Babinet [1]. The concept of using total-internal reflection to confine light inside a core of higher refractive index medium such as glass surrounded by a transparent cladding layer of lower index medium was first proposed by Narinder Singh Kapanny and is considered the invention of "Fiber Optics" [2]. However, commercial application of glass fibers was made possible by the work of Charles K. Kao, winner of the 2009 Nobel Prize in Physics, who predicted the possibility of making fibers with attenuation less than 20 dB/km and hence suitable for communication in the early 1960s [3]. Today fibers with losses on the order of 0.2 dB/km at 1550 nm are manufactured by using high purity glass material and provide a low-loss medium for long-distance communication using lasers.

Optical fibers can be classified on a number of criteria. The most basic of them is the fiber material used for the core. Different fibers have different loss, dispersion and nonlinear response characteristics depending on the material properties and its purity. Fused silica based optical fibers are currently the most commonly used fibers due to the abundance of the raw material and excellent light transmission capabilities. Plastic fibers, fluoride fibers and tellurite fibers are some other examples of different materials used in fiber fabrication depending on the application requirements. Another classification criterion for fibers is active versus passive fibers. Active fibers usually contain specific amounts of doping materials to extract stimulated processes required for lasers and amplifiers. For example, ytterbium (Yb), erbium (Er) and thulium (Tm) dopants are common in the fabrication of gain fibers used for building fiber lasers and amplifiers. A new class of fibers called photonic crystal fibers has also emerged in the last decade or

so, which uses light guiding by periodic structures as against to total internal reflection and have the advantage of the flexibility in tailoring the dispersion properties of the fiber.

Fibers can also be classified on the basis of the number of modes that can propagate in the core. Modes can be considered as the different eigenfunctions of the Maxwell's equations governing electromagnetic wave propagation as applied to fiber geometry [4]. The modal properties of the fiber depend on the physical dimensions the fiber such as core diameter and refractive index difference between the core and cladding material. Multimode fibers usually have a larger core diameter and are used for light delivery applications in imaging [5]. An important class of optical fibers is single mode fibers that can support propagation of light only in a single mode approximated by the fundamental Gaussian shape and are called single mode fibers.

Single mode optical fibers have several unique properties that make them suitable for a number of applications compared to other physical layer media. In addition to delivering light with very low loss, single mode fibers transmit light in a fundamental Gaussian beam shape which allows for the preservation of a single spatial mode beam profile at the output. Typical single mode fibers confine the light beam in a core of diameter ~10 μm allowing for generation of high intensity beams inside the glass medium making them suitable for study of nonlinear phenomenon. This unique property has fuelled the field of nonlinear fiber optics since the 1970s with the demonstration of stimulated Raman, Brillouin and soliton effects.

In my thesis, I will demonstrate systems and devices based on properties of single mode fibers, such as high nonlinearity, mode selectivity and single spatial mode output beam quality with potential applications in remote sensing, communication and optical metrology.

1.1. MID-INFRARED SUPERCONTINUUM LASER

Fiber lasers have recently grown to prominence for their capacity to efficiently generate kilowatt levels of power. The structure of optical fibers allows for excellent mode overlap between the pump and the signal beams to generate high power levels in relatively small pump and signal interaction lengths. Coupled with the nonlinear properties of the fiber material, a variety of fiber based devices have been demonstrated.

Particularly, supercontinuum light sources have attracted considerable attention for fiber based broadband light generation. The process of supercontinuum generation is the result of propagation of high intensity light pulses in a suitably dispersive medium, which results in the interplay of numerous nonlinear processes such as self-phase modulation, modulation instability, stimulated Raman scattering, etc. to give rise to a continuum of wavelengths at the fiber output [6,7]. Such a light source has advantages in that it possesses the broad wavelength nature of an incandescent lamp, while providing flexibility in spatially manipulating the output beam. Consequently, such light sources provide a high level of directionality and intensity for applications such as LIDAR [8], chemical sensing [9], etc.

In remote chemical sensing applications, the laser output invariably travels through the atmosphere before being detected by suitable detectors. To increase the strength of the received signal, it is required that the wavelength of the light source suffer minimal attenuation while passing through the atmosphere. From this standpoint, studies have been conducted, which suggest specific wavelength ranges where the atmosphere is relatively transparent called the atmospheric transmission windows [10]. Of particular interest are the three windows extending from 2-2.4 μm, 3-5 μm, and 8-12 μm. The transmission windows in the 2-5 μm range are attractive due to their proximity to the 1.55 μm telecommunication band where the large scale of manufacturing provides commercial-off-the-shelf components with high reliability and competitive pricing.

With the intention of leveraging mature telecommunication technology, our research group has worked extensively in the past few years developing a novel broadband supercontinuum light source extending from 800 – 4500 nm. Typical supercontinuum lasers use specialty mode-locked source which are capable of generating high peak power, ultra-short pulses suited for nonlinear processes. However, it was demonstrated by Xia et al. in [11] that the need for mode-locked lasers can be eliminated by using a novel two-step pulse break up process which uses the physics of the fiber to initiate high peak power pulse generation starting from approximately nanosecond long quasi-cw light pulses of moderate intensity. The technique makes use of the anomalous dispersion regime of optical fibers, where longer wavelengths travel slower than shorter wavelengths contrary to the normal dispersion regime, where the reverse occurs. This

particular regime is of significance to the observation of nonlinear phenomenon since the fiber can support soliton pulses through the interplay between dispersion and nonlinearity [12]. Instability in the medium caused by high intensity pulses propagating through an anomalously dispersive medium, such as fused silica SMF with 1.55 μm wavelength input, leads to modulation of the beam amplitude initiated by background noise, which causes quasi-cw pulses to break up into higher intensity sub-picosecond pulses similar to those observed at the output of mode-locked lasers. Such process is termed as modulation instability initiated pulse break-up. Subsequently, stimulated Raman processes, which denote energy transfer to longer wavelengths based on phonon interaction in the fiber glass medium and soliton self-frequency shift, which corresponds to intra-pulse Raman energy transfer from the shorter wavelength components to the longer wavelengths, in a suitable nonlinear medium leads to generation of light over a continuum of wavelengths and hence termed as supercontinuum generation. The extent of the long wavelength edge of the continuum starting from 1.55 μm wavelengths depends on the fiber material absorption edge. For example, wavelengths up to 2.8 μm have been generated in fused silica fibers starting from nanosecond long input pulses by carefully adjusting the length of the fused silica SMF used in the pulse break-up stage and the high nonlinearity medium [11]. In order to shift the spectrum further, low mid-infrared loss medium such as ZBLAN fluoride fibers can be used. Continuum extending out to 4.5 μm has been demonstrated in these fibers [13].

However, the efficiency of energy transfer from 1.55 μm to longer wavelengths, particularly beyond 3.8 μm is relatively poor. For example, the ZBLAN based 10.5 W supercontinuum source demonstrated in [14] generates almost no light beyond 3.8 μm. The long wavelength edge is predicted to be limited by the high material absorption in ZBLAN at wavelengths beyond 4.2 μm. Modifications in the properties of the ZBLAN fibers such as the numerical aperture and core diameter reduction can lead to higher nonlinearity in the fiber core and lower bend-induced loss in the fiber at longer wavelengths and hence lead to extension of the continuum long wavelength edge closer to the material absorption edge, as will be demonstrated in my thesis. Larger wavelength shifting can also be achieved by generating higher peak power 1.55 μm pulses at the input of the ZBLAN fiber compared to ~6.1 kW pulses used previously. However, such

increase is usually associated with the advent of damage to various system components and limitations from the nonlinearity in the power amplifier system.

In chapter 2, I will discuss results of a novel technique to efficiently shift light from 1.55 μm to beyond 3.8 μm. The method involves breaking the continuum process into two stages separated by an intermediate amplification stage. Such parsing of the supercontinuum generation process will be shown to provide additional boost to the wavelength shifting process by moving the supercontinuum pump closer to the material absorption edge. In this scheme, higher efficiency Tm-amplifiers are used to amplify wavelength components around 2 μm at the output of a standard SMF-based supercontinuum source. Coupling of the amplifier ~2 μm pulses leads to long wavelength generation with ~2.5 times the efficiency of previously demonstrated Er:Yb based amplifier systems operating at 1.55 μm. Experiment and simulation results will be presented to demonstrate the successful implementation of the two-stage continuum process in wavelength generation >3.8 μm.

1.2. BROADBAND SURFACE-NORMAL OPTICAL MODULATOR

Another application for fiber-based broadband light sources is in the area of optical networks [15]. Typical network configurations use wavelength-division multiplexing to support multiple users on a single physical connection by using wavelength allocation to users. The availability of broadband lasers can increase the capacity of the physical network by allowing more number of users to be connected to a single central unit housing the light source [16]. Such sharing of network resources amongst users can lead to reduction in operation costs. Cost sharing of network components can help in the large scale commercial deployment of passive optical networks in the last mile, which refers to the leg of the network connecting users to a central office. Increasing the capacity in the last mile can lead to reduction in the bottleneck of current networks and allow for higher speed connectivity to end users [17]. Wavelength division multiplexing is particularly advantageous in these architectures as it allows for independent operation of remote terminals unlike in the case of time-division multiplexed networks, where synchronization between different users is necessary. An additional advantage in WDM-PONs is that the network components need not operate at the aggregate network capacity

speeds, but instead operate at individual user link speeds. Such WDM-based passive networks are currently under experimental deployment in several parts of the world. However, large-scale deployment is yet not feasible due to complexity involved in channel assignments. For example, each user needs to operate at a specific wavelength for accommodation with a central office. Any drift in operating wavelength can cause collision of information packets with other users on the network.

To solve the above problem, devices capable of operation over a larger wavelength band are sought for the user terminal. One approach is to generate a carrier for the upstream communication link at the central office and provide it to the user, where broadband modulators, also referred to as "colorless" modulators, imprint local data on to the carrier and reflect it back to the central office [18]. Some examples of previously demonstrated colorless modulators include reflective semiconductor optical amplifiers [19] or injection locked Fabry-Perot lasers [20]. However, due to the active nature of both these devices, there is risk of accidental lasing in the network due to reflections in the fiber link from passive components in the network.

The ideal component choice for remote terminal, therefore, is a passive, reflective and colorless modulator. The requirement for wavelength independent operation suggests non-resonant electro-optical effects as ideal candidate due to their relative insensitivity to the wavelength of incident light. Free-carrier dispersion is one such effect observed in semiconductors at wavelengths above the band-edge. Devices based on the free-carrier effect have been demonstrated in both waveguide and surface-normal configurations [21, 22]. However, waveguide modulators are currently not pursued for low-cost applications due to the associated complexity of assembly, drive circuitry and packaging of coupling optics, which makes large-scale manufacturing difficult [23]. Surface-normal devices such as VCSELs and LEDs on the other hand are cheaply available as their manufacturing has been shown to benefit from economies of scale.

In chapter 3, I describe a surface-normal, broadband, GaAs-based optical modulator which uses the single mode properties of the delivery fiber in optical networks to create amplitude modulation. The devices splits the incident fundamental Gaussian light beam from a standard SMF and phase modulates two halves independently using the variation in charge carrier density across a pin-junction diode. A fraction of the phase modulated

light is not coupled in to the fiber due to the higher-order mode rejection properties of single mode fibers and leads to phase to amplitude modulation conversion, which can be observed using a detector. The device is fabricated in GaAs material and the performance is compared with a similar device fabricated in Silicon. Device characterization results in terms of modulation depth, frequency response and insertion loss are presented. Also, using a supercontinuum laser, the wavelength response of the modulator is characterized. Such a measurement is performed for the first time to my knowledge and provides a potential application of broadband supercontinuum sources as described in my thesis.

1.3. OPTICAL PROBE FOR DEFECT DETECTION IN BORES

Fibers as an efficient medium of light delivery have found illumination applications in a number of fields, such as in vivo surgery where direct access is limited. Optical probes used in medicine [24] and part manufacturing metrology [25] are two prime examples. Fiber based probes provide the flexibility and small physical dimensions for endoscopic imaging [26] as well as surgical applications [27]. The fiber-based biomedical probe demonstrated by Herz et al. in [28] has a cross-sectional dimension as small as 5 mm, allowing it to reach inside arteries, etc. Borescopes used for inspection of inner diameter surfaces of cylindrical parts also provide substantial advantage over previously used labor-intensive techniques such as wax-film and coordinate measuring machines (CMM) [29].

In chapter 4, I describe an optical probe based on scattering for detection of porosity defects, commonly found in cast metal parts, inside cylindrical bores as small as 5 mm in diameter. The technique is novel in its multiple angle defect inspection allowing not only detection of surface defects but also classification of the defect based on depth information. In this case, I use the spatial coherence of the output beam from a single-mode fiber to be able to generate unique features in the scattering profile from various types of surface defects and hence be able to detect and classify defects based on their scattering signatures. The probe design is explained in details and characterization of the proposed technique is carried out for a number of samples. Finally, a particular problem of interest to the automotive industry, in porosity detection inside transmission valve body spool bores is carried out and results and analysis are presented.

References

[1] Jeff Hecht, "Illuminating the Origin of Light Guiding," Optics & Photonics News 10(10), 26- (1999)

[2] Regis J. Bates, *Optical Switching and Networking Handbook*, New York: McGraw-Hill, (2001)

[3] Jeff D. Montgomary, "History of Fiber Optics," in *Fiber optic data communication: technological trends and advances*, Casimer DeCusatis, ed. (Academic Press, 1st Edition 2002), pp. 9-16

[4] John Gowar, Optical Communication Systems, 2nd ed. (Prentice/Hall Inc. Upper Saddle River, NJ 1993)

[5] B. A. Flusberg, E. D. Cocker, W. Piyawattanametha, J. C. Jung, E. L. M. Cheung and M. J. Schnitzer, "Fiber-optic fluorescence imaging," Nature Methods – **2**, 941-950 (2005)

[6] R. R. Alfano, *The supercontinuum laser source: fundamentals with updated references*, 2nd ed. (Springer, New York, 2006)

[7] A. Mussot, T. Sylvestre, L. Provino, and H. Maillotte, "Generation of a broadband single-mode supercontinuum in a conventional dispersion-shifted fiber by use of a subnanosecond microchip laser," Opt. Lett. **28**, 1820-1822 (2003)

[8] G. Méjean, J. Kasparian, E. Salmon, J. Yu, J. –P. Wolf, R. Bourayou, R. Sauerbrey, M. Rodriguez, L. Wöste, H. Lehmann, B. Stecklum, U. Laux, J. Eislöffel, A. Scholz, A. P. Hatzes, "Towards a supercontinuum-based infrared lidar," Appl. Phys. B 77, 357-359 (2003)

[9] H. Li, D. A. Harris, B. Xu, P. J. Wrzesinski, V. V. Lozovoy, and M. Dantus, "Standoff and arms-length detection of chemical with single-beam coherent anti-Stokes Raman scattering," Appl. Opt. **48**, B17-B22 (2009)

[10] Craig M. Payne (Ed.), Principles of Naval Weapons systems, 2nd Ed., Annapolis, MD, Naval Institute Press, 2010

[11] C. Xia, M. Kumar, M. –Y. Cheng, O. P. Kulkarni, M. N. Islam, A. Galvanauskas, F. L. Terry, Jr., M. J. Freeman, D. A. Nolan, W. A. Wood, "Supercontinuum generation in silica fibers by amplified nanosecond laser diode pulses," IEEE J. of Sel. Top. In Quant. Elect., Vol. 13, No. 3, May/June 2007

[12] G. P. Agrawal, *Nonlinear Fiber Optics*, 3rd edition, (Academic, San Diego, 2001).

[13] C. Xia, M. Kumar, M. –Y. Cheng, R. S. Hegde, M. N. Islam, A. Galvanauskas, H. G. Winful, F. L. Terry, Jr., M. J. Freeman, M. Poulain, and G. Mazé, "Power scalable mid-infrared supercontinuum generation in ZBLAN fluoride fibers with up to 1.3 watts time-averaged power," Opt. Express **15**, 865-871 (2007)

[14] C. Xia, Z. Xu, M. N. Islam, F. L. Terry, Jr., M. J. Freeman, A. Zakel, and J. Mauricio, "10.5 W time-averaged power mid-IR supercontinuum generation extending beyond 4 μm with direct pulse pattern modulation," IEEE J. of Sel. Top. Quantum Electron., Vol. 15, No. 2, March/April 2009

[15] T. E. Stern, G. Ellinas and K. Bala, *Multiwavelength Optical Networks: Architectures, design, and control*, 2nd edition, (Cambridge University Press, 2009)

[16] B.C. Collings, M.L. Mitchell, L. Boivin, W.H. Knox, "A 1021 channel WDM system," IEEE Photon. Tech. Lts., Vol. 12, No. 7, July 2000

[17] A. Banerjee, Y. Park, F. Clarke, H. Song, S. Yang, G. Kramer, K. Kim, and B. Mukherjee, "Wavelength-division-multiplexed passive optical network (WDM-PON) technologies for broadband access: a review [Invited]," J. Opt. Netw. **4**, 737-758 (2005)

[18] M. Presi, R. Proietti, K. Prince, G. Contestabile, and E. Ciaramella, "A 80 km reach fully passive WDM-PON based on reflective ONUs," Opt. Express **16**, 19043-19048 (2008)

[19] T. –Y. Kim, S. –K. Han, "Reflective SOA-Based Bidirectional WDM-PON Sharing Optical Source for Up/Downlink Data and Broadcasting Transmission," *Photonics Technology Letters, IEEE* , vol.18, no.22, pp.2350-2352, Nov.15, 2006

[20] Z. Xu, Y. J. Wen, W. –D. Zhong, C. –J. Chae, X. –F. Cheng, Y. Wang, C. Lu, and J. Shankar, "High-speed WDM-PON using CW injection-locked Fabry-Pérot laser diodes," Opt. Express **15**, 2953-2962 (2007)

[21] A. Liu, L. Liao, D. Rubin, H. Nguyen, B. Ciftcioglu, Y. Chetrit, N. Izhaky, and M. Paniccia, "High-speed optical modulation based on carrier depletion in a silicon waveguide," Opt. Express **15**, 660-668 (2007)

[22] O. Solgaard, A.A. Godil, B.R. Hemenway, D.M. Bloom, "All-silicon integrated optical modulator," IEEE J. Sel. Area Comm. Vol. 9, No. 5, pp. 704-710, 1991.

[23] N. C. Helman, J. E. Roth, D. P. Bour, and D. A. B. Miller, "Misalignment-tolerant surface-normal low-voltage modulator for optical interconnects at 1.55μm," in *Conference on Lasers and Electro-Optics/International Quantum Electronics Conference and Photonic Applications Systems Technologies*, Technical Digest (Optical Society of America, 2004), paper CThH4

[24] G. J. Tearney, M. E. Brezinski, B. E. Bouma, S. A. Boppart, C. Pitris, J. F. Southern, and J. G. Fujimoto, "In Vivo Endoscopic Optical Biopsy with Optical Coherence Tomography," Science: 276 (5321), 2037-2039 (1997)

[25] H. K. Tonshoff, I. Inasaki (Eds.), *Sensors in manufacturing*, (Wiley-VCH Verlag GmbH, Weinheim, 2001)

[26] T. Xie, S. Guo, Z. Chen, D. Mukai, and M. Brenner, "GRIN lens rod based probe for endoscopic spectral domain optical coherence tomography with fast dynamic focus tracking," *Optics Express*, **14**, 3238-3246 (2006)

[27] M. R. Treat, S. L. Trokel, R. D. Reynolds, V. J. DeFilippi, J. Andrew, J. Y. Liu, and M. G. Cohen, "Preliminary evaluation of a pulse 2.15-μm laser system for fiberoptic endoscopic surgery," Lasers in Surgery and Medicine 8: 322-326 (1988)

[28] P. R. Herz, Y. Chen, A. D. Aguirre, K. Schneider, P. Hsiung, J. G. Fujimoto, K. Madden, J. Schmitt, J. Goodnow, and C. Petersen, "Micromotor endoscope catheter for in vivo, ultrahigh-resolution optical coherence tomography," Opt. Lett. **29**, 2261-2263 (2004)

[29] D. Steiner, R. Katz, "Measurement techniques for the inspection of porosity flaws on machined surfaces," *Journal of Computing and Information Science in Engineering*, **7**, 85 (2007)

Chapter II

All-fiber integrated mid-infrared supercontinuum light source based on higher efficiency Tm-amplifiers

Light generation in the mid-IR wavelength range from 2-5 μm is beneficial for a number of applications, including spectroscopy [1,2], explosive and chemical detection [3], remote sensing and ranging [4], free-space communications [5], and medicine [6]. However, efficient broadband sources extending over a range of wavelengths in the mid-IR are not easily available due to lack of reliable components in the mid-infrared wavelength range unlike in the telecommunication bands extending from 1.3-1.6 μm.

Of particular interest are light sources capable of generating wavelengths in the so-called atmospheric transmission windows [7], where losses during propagation are minimal. The transmission windows are found in regions where atmospheric constituents such as CO_2, water-vapor, etc. do not absorb light. Fig. 2.1 below shows the atmospheric transmission in the visible to mid-infrared wavelength range. High transmission is observed in the 2-2.5 and 3.5-4.2 μm wavelength ranges. Light sources in these wavelengths are suited for applications requiring long distance propagation through the atmosphere.

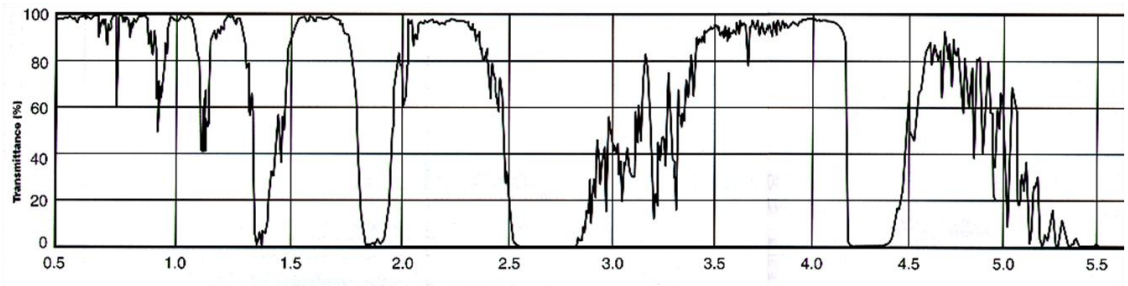

Fig. 2.1 Atmospheric transmission in the visible to mid-infrared wavelength range (Source: Santa Barbara Research Center)

2.1. Background

Currently available solid-state laser technologies operating in the mid-IR wavelength range include quantum cascade lasers (QCL) [8], optical parametric oscillators (OPO) [15, 16] and rare-earth doped ZBLAN fiber lasers [24]. In comparison, SC sources are attractive because they can cover multiple wavelength bands, thus increasing the sensitivity and selectivity of spectroscopic studies.

One technique to reliably generate mid-IR SC is by shifting light from a near-IR laser into the mid-IR wavelengths using nonlinear optical processes. In ZBLAN fibers, SC extending to ~6.28 μm has been demonstrated by pumping ~2 cm length of fiber with mode-locked 1480 nm pulses of ~50 MW peak power and 20 mW average power [9]. Another mid-IR SC fiber laser demonstration based on ZBLAN fiber used a 1550 nm mode locked Er-doped laser and generated ~5 mW in the wavelength range from 1.8-3.4 μm [2]. Fibers based in high nonlinearity materials such as tellurite have also been used for SC generation. For example, continuum extending from ~0.8-4.87 μm with 90 mW output average power has been demonstrated by coupling 110-fs long, 1.55 μm pulses in to 0.8 cm length of tellurite photonic crystal fiber (PCF) [10].

A novel technique to eliminate the need of mode-locked lasers for high peak power pulse generation has been previously demonstrated. In this technique, modulation instability in standard SMF is used to initiate pulse break-up of quasi-continuous wave laser diode pulses [11]. Typically, one nanosecond long 1.55 μm laser diode pulses are first amplified through two or more stages of Er/Er:Yb fiber amplifiers. After initiating pulse break-up in a few meter lengths of standard SMF, SC extending from 0.8-4.4 μm has been generated in ~7 m length of ZBLAN fiber, with 23 mW average power output [32]. Also, using linear scaling of the time-average power with the pulse repetition rate, up to 10.5 W average power output in a continuum extending from 0.9-3.8 μm has been demonstrated [12]. More recently, by using ~20 kW 1.55 μm peak power pulses and longer lengths of ZBLAN fibers (~12 m), a high average power spectrum extending out to ~4.2 μm has been achieved using all 1.55 μm amplification stages [13].

In this chapter, I demonstrate an all-fiber integrated mid-IR supercontinuum laser, based on a Tm-doped power amplifier stage. The motivation to incorporate a TDFA stage is driven by the higher pump-to-signal conversion efficiency demonstrated in Tm-doped

gain fibers compared to EYFAs. For example, slope efficiency as high as 56% is demonstrated in LMA Tm-doped gain fiber [40] compared to LMA-EYFAs, which have demonstrated slope efficiencies of ~38% [43] in comparable fiber geometries. Also, shifting the SC pump from 1.55 to ~2 μm is pursued with an attempt to generate a longer extending SC in the mid-IR wavelengths.

Various techniques to generate ~2 μm light pulses for input to TDFAs have been demonstrated. For example, by using a mode-locked Er fiber laser with polarization-maintaining components operating at 1557 nm followed by an EYFA, a Raman shifting soliton pulse to ~2 μm in 12 m length of high numerical aperture (NA) fiber has been demonstrated in the past [20]. A subsequent dispersion-managed large mode area TDFA stage generates pulses with up to 230 kW peak power at ~2 μm. Another approach generates ~750-fs long ~1.95 μm pulses using a saturable absorber based on carbon nanotubes in the Tm-doped fiber laser cavity [21]. Techniques using ~1.55 μm laser diode pulses instead of mode-locked lasers have also been demonstrated. One approach involves successive orders of cascaded Raman wavelength shifting in germanium-doped fused silica fibers with NA of ~0.41 [22]. In this approach, up to 3 orders of shifting from 1.53 μm leads to light generation at 1.94 μm. Another demonstrated technique involves gain-switching a Tm-doped fiber cavity with a modulated 1.55 μm pump to generate 10-ns long 2 μm pulses [23].

In our approach, ~1-ns long laser diode pulses at 1.55 μm are amplified to ~2.5 kW peak power. Pulse break-up through modulation instability, and long wavelength shifting through Raman processes in ~25 m length of standard SMF gives rise to ~2 μm pulsed light components for input to a Tm-doped fiber amplifier. The technique eliminates the need of mode-locked lasers for high peak power pulse generation at ~2 μm and uses all standard telecommunication wavelength fiber-coupled components. Also, due to absence of a regenerative cavity, the system does not require any bulk 2 μm optical isolators to prevent feedback from spontaneous emission or spurious reflection from subsequent TDFA or SC generating stages.

2.2. Motivation

From a mid-IR light generation perspective, the motivation to switch from an Er:Yb power amplifier system to a Tm-amplifier are manifold. One of the main reasons is the higher pump-to-signal conversion efficiency recently demonstrated in Tm-amplifiers. For example, Tm-amplifier slope efficiencies of up to 53% have been demonstrated for 790nm pumped systems in continuous-wave mode of operation in comparison to ~38% of maximum demonstrated slope efficiency from commercially available Er:Yb gain fibers [43]. Also up to 300 W output light generation has been demonstrated from a Tm-fiber laser. The higher efficiency obtainable in Tm-systems is due to a cross-relaxation process that occurs during stimulated absorption [18]. Fig. 2.2 shows the transitions Tm-systems when excited by 790 nm pump light.

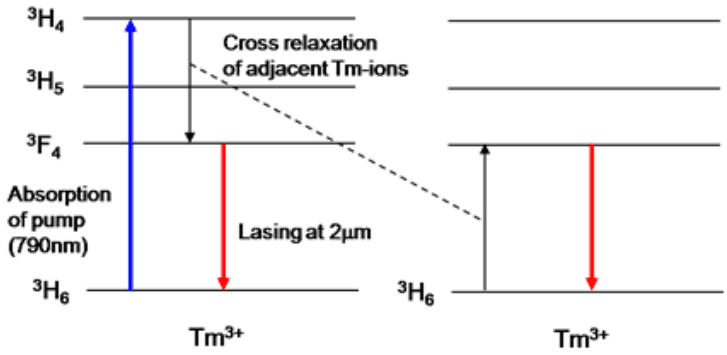

Fig. 2.2 Quasi-three-level Tm-doped fused silica fiber amplifier system with cross relaxation of adjacent Tm3+ ions when pumped with 790 nm light

As shown, the ground $^3H_6$ state ions can be excited to an upper level, $^3H_4$ using 790 nm pump photons. However, when excited ions relax into the $^3F_4$ meta-stable state, the subsequent relaxation of the ion leads to bumping an additional ground state Tm-ion to the meta-stable state through cross-relaxation between adjacent ions and both ions contribute to the stimulated emission process around 2 μm. As a result, up to two signal photons can be made available for every pump photon used by the system giving rise to theoretical quantum efficiency >100%.

Another incentive to switching to a Tm-amplifier is that by pumping the supercontinuum generating fiber at 2 μm instead of 1.55 μm, one can expect to get a longer wavelength shift in the mid-infrared for same peak power pulses. This can be used to an advantage either by generating a longer extending mid-IR spectrum, or by operating

at a lower peak power setting so as to prevent peak-power related damage in the system. On the same lines, it could also reduce the length of specialty mid-infrared fiber that is required for efficient light generation and hence reduce system cost. Another underlying advantage is cutting off the amplification of the spontaneous emission going from an Er:Yb mid-amp to Tm-power-amp, where gain could be robbed away from signal pulses by spontaneously emitted components. By switching to a Tm-amplifier system, all light below ~1.9 μm, including ~1.53 μm amplified spontaneous emission is absorbed in the Tm-gain fiber, thus reducing the impact of ASE in the output.

2.3. Challenges

One of the basic requirements for implementing a Tm-based mid-infrared supercontinuum system is a pulsed 2 μm source. In my approach, I have used a standard telecommunications-component based light source in which nanosecond laser diode pulses at 1.55 μm are amplified to a few kW peak power. Pulse break-up using modulation instability, self-phase modulation and Raman processes in a reasonably long length of standard SMF gives rise to an off-the-shelf, reliable and versatile system for 2 μm light generation.

The proposed architecture for the Tm-based mid-infrared supercontinuum laser is shown in Fig. 2.3.

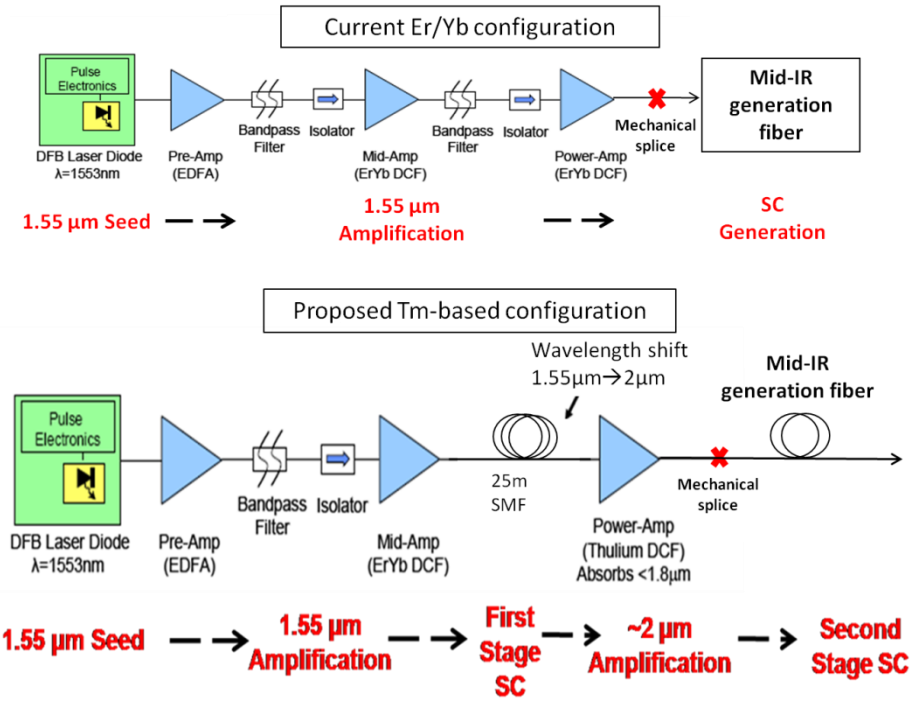

Fig. 2.3 Proposed system architecture for replacing Er:Yb power amplifier with Tm-amplifier for more efficient mid-infrared supercontinuum generation

In concept, the novelty of the approach lies in reversing the order of the modulation instability-based pulse break-up process and the power amplifier stage. In previously demonstrated Er:Yb systems, all amplification stages are stacked together to give rise to high peak power 1.55 µm pulse generation up to ~20 kW, followed by ~2 m fused silica single mode fiber, which initiates the pulse break-up process. Subsequently, ZBLAN fibers with low loss in the 1.5-4 µm region are used for supercontinuum generation in the mid-IR. In the new Tm-based system, it is proposed to switch the pulse break-up stage to before the power amplifier. Due to the lower peak power (up to 3 kW) available from the Er:Yb mid-amplifier stage, a longer length of fused silica single mode fiber is required for generation of 2 µm light components for input to a Tm-amplifier, which has a gain band extending from 1.91-2.13 µm. The amplified Tm-output is then coupled in to suitable length of ZBLAN fiber for mid-infrared supercontinuum generation.

In practice, once the ~1 ns long 1.55 µm light pulses have under gone spectral shift to 2 µm, it is unclear whether amplification of wavelength selective components of different parts of the pulse can generate enough peak power to further sustain the supercontinuum generation process in to the mid-IR. Such a scheme has never been demonstrated in a quasi-cw regime and is one of the foremost risks to the successful implementation of the

Tm-based architecture. Another question that arises is whether the Tm-based system could demonstrate power scalability in a manner similar to the demonstrated Er:Yb system by increasing the pulse repetition rate and pump power. The novelty of the two-stage continuum generation also raises doubt regarding the stability and efficiency of the subsequent mid-IR generation processes. In addition, components for Tm-amplifier have become available only recently, making their performance in the proposed architecture unpredictable.

In the remainder of this chapter, I will demonstrate how the above challenges were mitigated successfully. I have demonstrated a mid-IR supercontinuum laser based on Tm-amplifier with a fused silica supercontinuum input. The laboratory set-up has shown successful generation of a spectrum extending from 1.9 to >4.5 μm wavelengths at the output of ~8.5 m length of ZBLAN fiber with power scalable generation of up to 0.7 W average power in band IV wavelengths. The band IV generation efficiency of the demonstrated system has been optimized to >2.5 times that of the previously demonstrated Er:Yb system [13]. All components of the system have been shown to perform stably for a continuous period of 2-hours without the need for any human intervention and any apparent damage to system components.

2.4. Tm-system set-up

2.4.1. Fused silica continuum based 2 μm light source

The experimental set-up for 2 μm light generation is shown in Fig. 2.4 and consists of an amplified 1.55 μm source followed by a spectrum shifting standard SMF fiber. The seed laser consists of a 1553 nm distributed feedback (DFB) laser diode with ~1-ns long pulses output at a repetition rate adjustable from a few MHz down to ~10 kHz. The laser diode pulses are amplified through two stages – a single mode Er-doped fiber amplifier (pre-amp) followed by a cladding pumped Er:Yb doped mid-amp. The pre-amp stage consists of ~2 m length of 4/125 μm gain fiber pumped by up to 400 mW at 980 nm. A 100 GHz line width optical add-drop multiplexer at the signal wavelength is used to filter out amplified spontaneous emission (ASE) generated in the pre-amp stage. The mid-amp stage consists of ~5 m of cladding pumped 7/130 μm Er:Yb co-doped fiber pumped by a single 10W 976 nm laser diode.

A near-IR continuum starting from 1.55 µm is first generated in standard SMF. The mid-amp is used to boost the peak power level of the optical pulses to few kW level and the output is spliced to ~25 m length of standard SMF. For the case of the mid-amp output, the peak power of the pulses can be estimated from their duty cycle and the measured average power at the output of the amplifier. For example, with a pulse width of ~1-ns and a pulse repetition rate of 500 kHz, 1 W output from the mid-amp corresponds to ~2 kW peak power of the individual pulses.

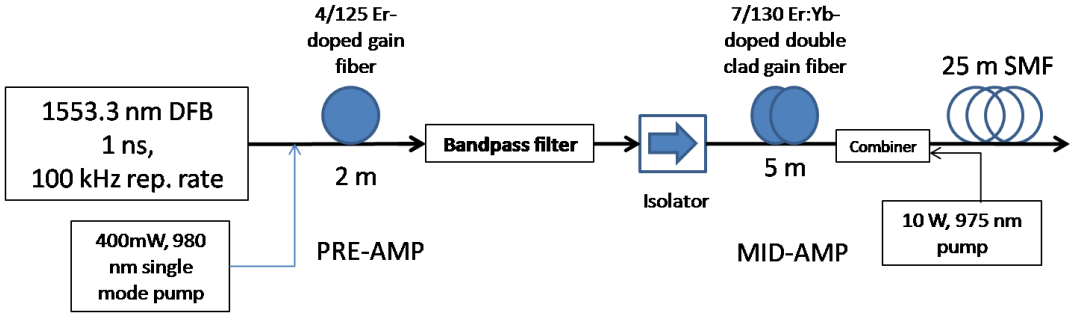

Fig. 2.4 Experimental set-up for fused silica supercontinuum based 2 µm source

The output of the standard SMF-based 2 µm light source is spliced to a large mode area-TDFA, which serves as the power-amp. LMA gain fiber is chosen to reduce nonlinear effects in the amplifier and has core/cladding dimensions of 25/250 µm. The gain fiber has a low core NA of ~0.1 to reduce the multi-modedness in the fiber at 2 µm wavelength, which is achieved in Tm-doped fibers by a raised refractive index pedestal layer surrounding the fiber core [40]. The gain fiber has rated peak absorption of 5 dB/m at 793 nm and a 4.5 m length is chosen to provide sufficient pump depletion. The mode conversion from standard SMF to LMA gain fiber is achieved by a pump-combiner/mode adapter with a 10/125 µm fiber at the input and a 25/250 µm passive fiber matched geometrically to the Tm-gain fiber at the output. The output of the Tm-gain fiber is spliced to a second pump-combiner/mode adapter, which has a dual-clad output fiber with 10/125 µm core/cladding diameters allowing for convenient coupling to the ZBLAN fiber. In addition, the output combiner combines two fiber-coupled 35 W, 790 nm pump lasers with 105 µm core diameter, 0.22 NA fiber pigtails in to the gain fiber to form a backward pumped amplifier configuration. The gain fiber is heat sunk by coiling it around a copper mandrel with grooves matched to fit the gain fiber.

In another implementation of the TDFA, a small-core gain fiber with core/cladding dimensions of 10/130 μm is used. The small-core set-up provides direct splicing of the standard SMF output to the TDFA input. A single combiner on the output side couples pump light in to the gain fiber in the backward propagating direction.

2.4.2. 35 W, 790 nm pump diode set-up

The 35 W pump diodes used in the set-up demonstrate a FWHM of ~1.2 nm with center wavelengths of ~791 nm and typical threshold currents of 8 A. The electro-optical efficiency of the lasers is specified to be ~41% with 35 W output at ~49 A current. The pump diode is mounted on a thermo-electric (TE) cold plate to temperature tune the pump wavelength. A thermistor mounted on the cold-plate provides feedback to the electronic circuit driving the current in the cold-plate to maintain the diode temperature stable during operation. The current through the two pump lasers is modulated by a square wave with 50% duty cycle at ~250 Hz to reduce the thermal load in the system and allows for modulation of the SC output without the need for external chopping equipment. The modulation is achieved by connecting the two pumps in series with a MOSFET switch driven by a signal generator. A bank of resistors is also included in the circuit to provide current limiting along with other safety measures to prevent damage to the pumps due to parasitic currents. For driving the pump diodes with continuous wave (CW) current, the signal generator is replaced by a 9 V battery to keep the MOSFET switch turned on.

One of the challenges in the operation of the 35 W pump diodes is the large current required to drive them. As mentioned, the diodes require ~49 A current to generate 35 W of output power. In addition, the diodes need to be modulated with 50% duty cycle to allow for supercontinuum modulation. A schematic of the drive circuit used to modulate the pump diode is shown in Fig. 2.5. The circuit uses a 60 A heavy duty constant voltage power supply made by TENMA in series with a MOSFET switch, driven by a signal generator. The generator outputs a 250 Hz square wave signal with 50% duty cycle, with a voltage swing from -0.5 V to ~11 V. During the low voltage phase of the input signal, the MOSFET switch is turned off disconnecting the power supply from the diode circuit. Conversely, when 10.5 V is applied to the gate terminal of the MOSFET, the circuit is

complete causing current to flow through the diodes. The diodes themselves are connected in series to eliminate the need for separate power supplies for the two diodes. A bank of resistors is also included in the circuit to provide current limiting. Across the two diodes, Schottky diodes are connected in reverse polarity as shown in the schematic to prevent accidentally reverse biasing the pump lasers. A Zener diode is also connected across the diodes to prevent the signal generator voltage applied at the gate of the MOSFET to accidentally appear across the pump diodes. A voltage sensing circuit is also included in the set-up, which grounds the gate of the MOSFET, in the event a high current spike causes the instantaneous current in the circuit exceeds 55 A, which is the maximum rated current for the two pumps. For driving the pump diodes with CW current, the signal generator is replaced by a 9 V battery to keep the MOSFET switch continuously turned on while the power supply provides current to the pump lasers. The capacitors across the power supply prevent fluctuations in the voltage due to the power supply during starting up and shut down.

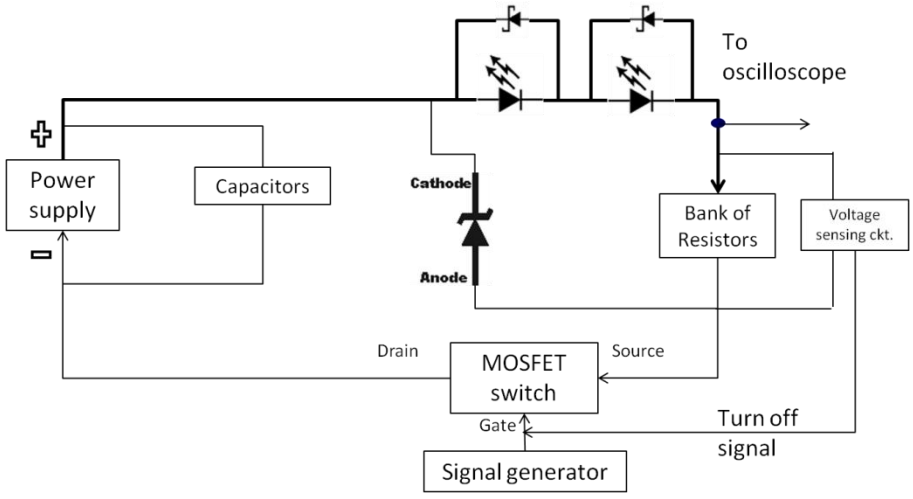

Fig. 2.5 Circuit for driving 35 W diodes with modulation of pump diode current

The voltage waveform across the bank of resistors is measured to determine the approximate peak current in the circuit. Fig. 2.6(a) shows the voltage drop across the resistors and the MOSFET switch in comparison to the signal generator waveform driving the gate of the MOSFET switch. As can be seen, when the signal generator outputs -0.5 V, the switch is off, causing all of the power supply voltage to drop across the switch. However, when the switch is on, a voltage proportional to the resistance value

of the resistor banks (75 mΩ) in the circuit is observed on the scope. Fig. 2.6(b) shows the current waveform through the resistors, obtained by dividing the voltage across the resistors by their resistance value. The figure shows no presence of spikes in the current waveform due to parasitics in the circuit.

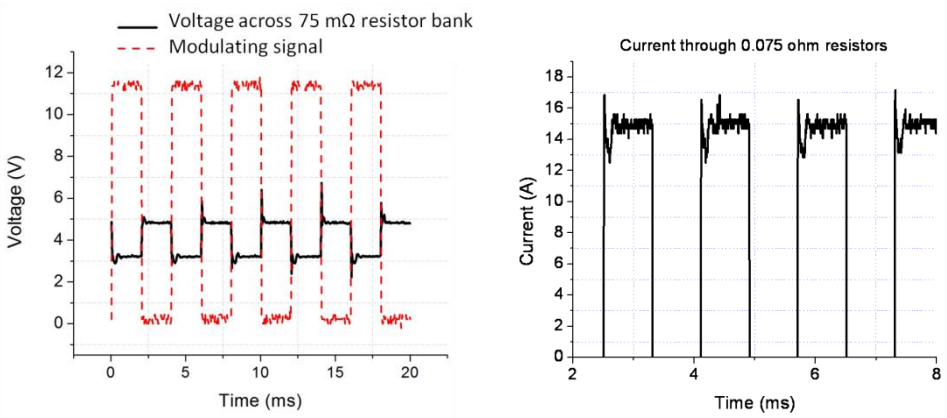

(a) (b)

Fig. 2.6 (a) Voltage waveform from signal generator applied to the gate of the MOSFET switch and the corresponding voltage drop across the 75 mΩ resistor and the MOSFET switch, (b) Current waveform through the 75 mΩ resistor bank showing lack of high amplitude current spikes

2.4.3. ZBLAN fiber properties

ZBLAN fibers are made of multi-composite glass composed of several heavy metal fluorides, specifically ZrF_4-BaF_2-LaF_3-AlF_3-NaF. They form a suitable nonlinear medium for mid-IR supercontinuum generation due to their relatively low loss compared to fused silica in the 2-4 µm wavelength region. The approximate loss curve of the fiber in comparison to fused silica, as provided by the manufacturer is shown in Fig. 2.7(a). As can be seen, the fiber has low loss of ~100 dB/km at 3.8 µm, beyond which the loss increases exponentially with wavelength due to the multi-phonon absorption edge of ZBLAN glass. In general, it is difficult to fabricate ZBLAN fibers with low loss because chemical vapor deposition techniques, which are popular for fabrication of fused silica glass cannot be applied to them due to lack of gaseous raw materials and the high quality of raw materials required during processing [24].

Nonlinear properties of ZBLAN are suited to supercontinuum generation processes. The nonlinear refractive index of ZBLAN is ~0.85 times that of fused silica [24], whereas the Raman gain coefficient is ~2.2x that of fused silica [25]. The Raman shift spectra of

ZBLAN glass as compared to fused silica based on results presented in [26], is also shown in Fig. 2.7(b), which shows the peak Raman shift to be at 580 cm^{-1} compared to ~440 cm^{-1} for fused silica. The zero dispersion wavelength of ZBLAN glass is close to 1.65 µm with longer wavelengths experiencing anomalous dispersion. All these properties suit efficient longer wavelength generation as the dominant nonlinear process occurring in the fiber when pumped at 2 µm is asymmetric stimulated Raman shifting towards longer wavelengths as compared to SPM-based symmetric broadening.

The fibers used in my experiments have a core radius of 8 µm and a cladding diameter of 123 µm. The fiber has a large numerical aperture of ~0.27, custom requested to reduce bend-induced loss at longer wavelengths [12].

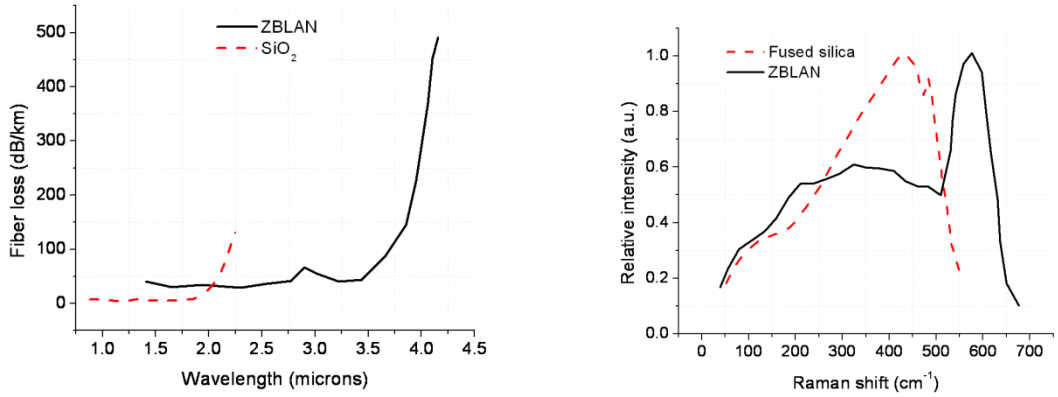

(a) (b)

Fig. 2.7 (a) ZBLAN fiber loss compared to fused silica (Source: KDD-FiberLabs) (b) ZBLAN Raman shift spectrum compared to fused silica

The output from the combiner used for coupling pump light into the gain fiber cannot be directly spliced to ZBLAN fibers due to the low melting temperature of ZBLAN glass (340°C) which is ~5 times lower than fused silica glass [27]. As a result, light output from the amplifier is butt-coupled to the ZBLAN fibers using a nanomax stage. The procedure involves angle cleaving the ends of the two fibers and keeping them in close proximity of each other while maintaining alignment between the two cores. Experimentally determined coupling losses are found to be in the range of 50-55% depending on the quality of cleaves and the proximity of the two fibers. The coupling efficiency is lower than that obtained in Er:Yb system (~60%) due to the larger mode area of 2 µm light in fused silica single mode fiber, compared to 1.55 µm. For example,

the calculated mode area in single mode fiber is ~10.4 µm at 1.55 µm and ~11.5 µm at 2 µm wavelength.

The complete system used for mid-IR supercontinuum generation is shown in Fig. 2.8.

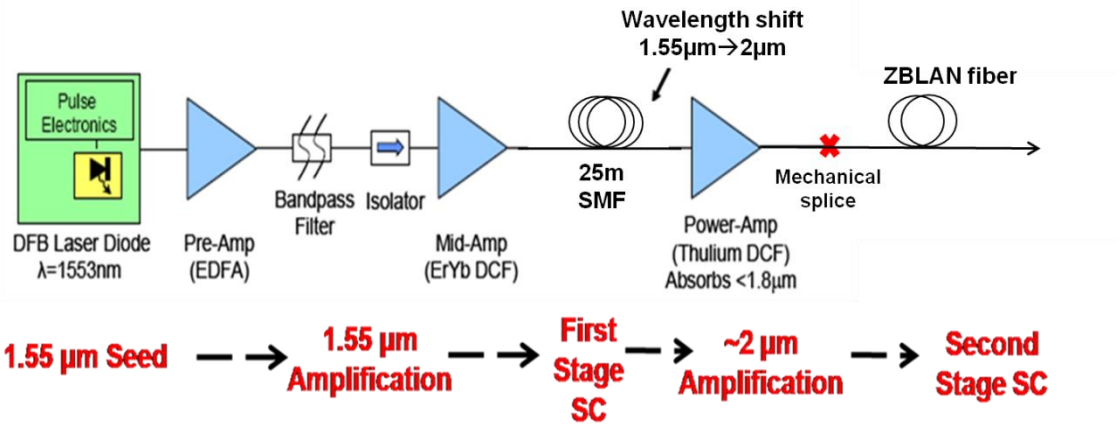

Fig. 2.7 Experimental set-up consisting of two SC stages separated by a Tm-doped power-amp stage

2.5. Experimental results

2.5.1. Two-stage LMA-TDFA based Mid-IR SC laser spectrum

The output spectrum of ~8.5 m length ZBLAN fiber mechanically spliced to the LMA-TDFA is shown in Fig. 2.9. The spectrum extends from ~1.9 to 4.5 µm with ~2.6 W total average power, of which ~0.7 W lies in wavelengths beyond 3.8 µm. The TDFA is pumped with ~30 W of 790 nm pump power with 50% modulation and outputs ~8 W of average power around 2 µm. The input to the TDFA comprises of output from ~25 m length standard SMF with ~2.5 kW peak power 1.55 µm laser diode input pulses of ~1-ns duration at 500 kHz repetition rate. The mechanical splice loss is observed to be ~45% corresponding to a coupled pump power of ~4.4 W. The residual power in the 1.8-2.1 µm wavelengths at the output of the ZBLAN fiber is ~0.13 W and is calculated from the area under the curve in the calibrated spectrum in these wavelengths, indicating ~97% SC pump depletion. With the modulation of the TDFA pumps with a 50% duty cycle square wave at 250 Hz, the SC output is also modulated. Hence an observed SC output power of 2.6 W corresponds to ~5.2 W SC output during the ON phase of the 250 Hz modulation signal. Similarly, the ~0.7 W average power measured in wavelengths beyond 3.8 µm indicates ~1.4 W power output from the laser in these wavelengths for 50% of the time.

The generated SC is continuous and with a spectral power density >0 dBm/nm (1 mW/nm) between ~3.6-4.3 µm. The intensity of the measured spectrum is calibrated in dBm/nm as follows. First, the measured SC spectrum is corrected for the spectral responsivity of the HgCdTe detector and the monochromator grating response. The spectral power density is then calculated by using the SC output power in the 3.5-3.8 µm wavelength region measured by the thermal power meter and appropriate wavelength filters. The SC laser generates ~0.9 W beyond 3.5 µm. The dip in the spectrum at ~4.25 µm is attributed to the CO_2 absorption in the atmosphere while traversing ~0.75 m path length inside the monochromator.

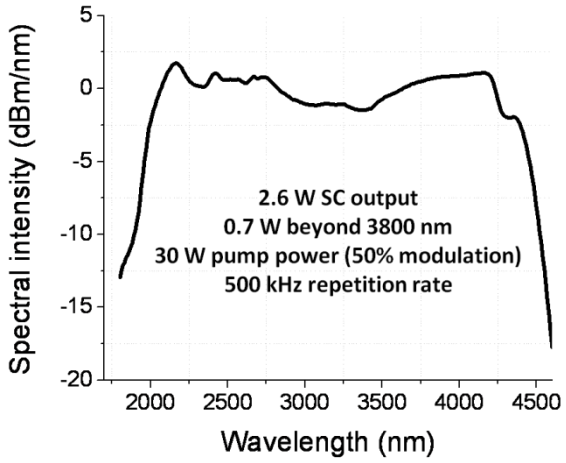

Fig. 2.8. SC spectrum generated from ~8.5 m length of ZBLAN fiber at ~61 W of 790 nm pump power in the LMA Tm-amplifier with ~5.2 W of total output with 50% modulation

Figure 2.10 shows the power scaling of the TDFA-based mid-IR SC laser as a function of the pulse repetition rate and the 790 nm pump power. By varying the pulse repetition rate electronically, the demonstrated Tm-system shows versatility in its ability to adjust the output power with similar spectral extent. Figure 2.10(a) shows the linear scaling of the average power at the output of 8.5 m length ZBLAN fiber over 125-500 kHz pulse repetition rates, while Fig. 2.10(b) shows the corresponding output spectrum. The spectrum out of the ZBLAN fiber has similar spectral extent and shape, however, the average power content scales linearly with the pulse repetition rate. The preservation of the spectral shape with increasing repetition rate shows that the doubling of the output average power with doubling of the pulse repetition rate is achieved by increasing the

frequency of occurrence of the pulses while maintaining similar pulse peak powers. Figure 3 also shows that the amount of 790 nm pump power required to double the output average power with pulse repetition rate does not scale linearly. For example, at 125 kHz, the SC laser outputs ~0.4 W average power at 12 W of modulated pump power. However, to double the output average power to ~0.8 W at 250 kHz, only ~3 W of additional modulated pump power is required suggesting ~13% slope efficiency with system repetition rate. The increase in efficiency with repetition rate is attributed to the threshold of the TDFA (~6 W) and the increase in amplifier efficiency at higher pulse duty cycles due to lower losses to spontaneous emission.

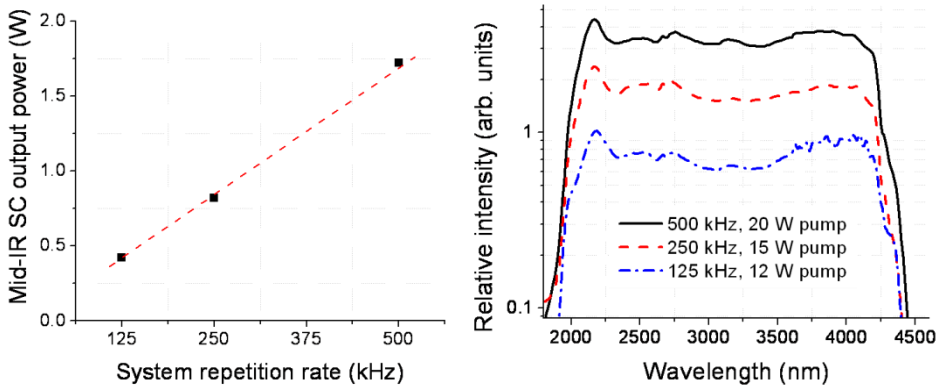

(a) (b)

Fig. 2.10. Output from 8.5 m length of ZBLAN showing power scaling with repetition rate and 790 nm pump power: (a) Output time-average power, (b) Output spectrum

Figure 2.11 compares the SC spectrum generated by ~8.5 m ZBLAN fiber pumped by a TDFA power amp to the best EYFA power amp results observed to date from ~12 m length of ZBLAN fiber with identical properties [13]. The observed long wavelength SC edge from the TDFA-based mid-IR source extends ~270 nm beyond the EYFA system output. The extension in the long wavelength edge is attributed to shifting of the SC pump from 1.55 to ~2 µm in the TDFA-system. Figure 4 also shows that the EYFA-SC extends in either direction around the ~1.55 µm SC pump. In comparison, the TDFA-SC extends only towards the longer wavelengths with respect to the SC pump at ~2 µm. The difference in the nature of the spectral broadening between the two systems is attributed to the dispersion properties of ZBLAN material, which has a ZDW around 1.65 µm [34]. As a result, pumping the ZBLAN fiber at ~2 µm compared to 1.55 µm, amounts to shifting the SC pump in to the anomalous dispersion regime, where spectral broadening is

observed to occur largely through stimulated Raman processes without much contribution from SPM as observed in EYFA systems.

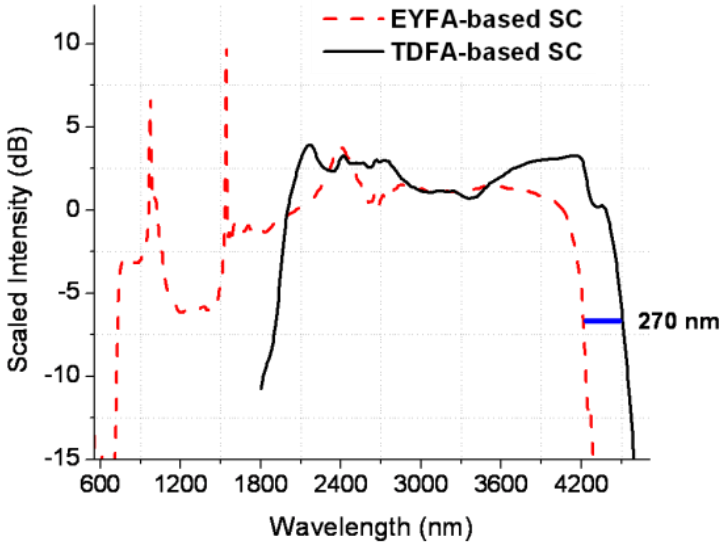

Fig. 2.11. Mid-IR SC spectrum from 8.5 m ZBLAN in TDFA power amp system compared to 12 m ZBLAN in EYFA-based system [13]

The evolution of the long wavelength edge of the 8.5 m ZBLAN fiber output as a function of modulated TDFA pump power at 500 kHz pulse repetition rate is shown in Fig. 2.12(a). At a fixed repetition rate, higher TDFA pump power corresponds to higher peak output powers and, hence, longer extending SC spectrum. Figure 2.12(b) plots the -20 dB SC wavelength edge of the measured spectra versus the modulated TDFA pump powers with saturation in the wavelength edge beyond ~4.5 μm. The long wavelength edge of the SC is limited by the absorption edge of the ZBLAN fiber. For example, at 4.5 μm, the absorption loss in the fiber is expected to be ~1 dB/m suggesting that any generated components at longer wavelengths in the ~8.5 m length of ZBLAN undergo rapid attenuation, preventing further spectral extension.

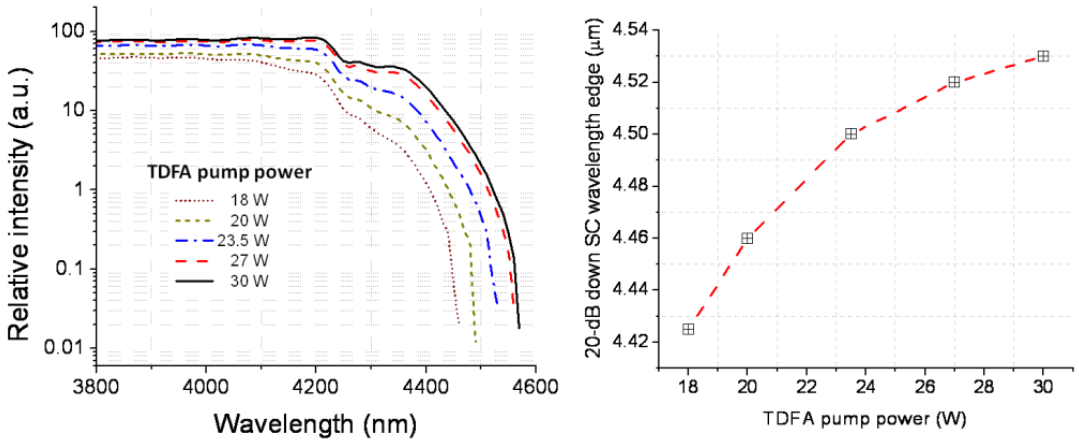

(a) (b)

Fig. 2.12. Evolution of the long wavelength SC edge in 8.5 m ZBLAN fiber length as a function of TDFA pump power measured at 500 kHz pulse repetition rate

2.5.2. LMA-TDFA based SC Laser efficiency

The thermal power meter measurements for the TDFA output, 8.5 m ZBLAN SC output and spectral content beyond 3.8 μm at the output of the ZBLAN fiber are plotted against the corresponding modulated TDFA pump power in Fig. 2.13. The LMA-TDFA operated in backward pumped configuration shows an overall efficiency of ~27% with ~8 W output power at ~30 W of 790 nm pump power. Observed SC output power of ~2.6 W corresponds to an overall mid-IR output efficiency of ~9% with respect to the 790 nm pump. ~0.7 W of the ZBLAN output lies in wavelengths beyond 3.8 μm leading to an observed efficiency of ~2.35% in generating wavelengths >3.8 μm with respect to the TDFA pump power.

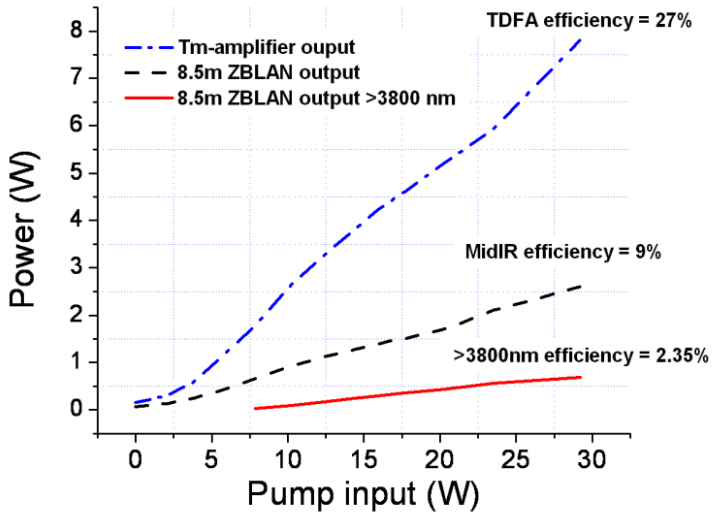

Fig. 2.13. Power meter measurement of TDFA output, 8.5 m ZBLAN SC output and output average power beyond 3.8 µm versus TDFA pump power

Table 2.1 summarizes the efficiency of various components of the TDFA-based MISCL. The Er:Yb mid-stage amplifier in the set-up outputs ~1.25 W of average power around 1.55 µm. The first SC section comprising of ~25 m standard SMF spliced to the mid-amp, outputs ~1 W total power, of which ~0.59 W lies in wavelengths beyond 1.8 µm, where TDFA gain occurs. The efficiency of the TDFA stage is maximized by optimizing the splices between the LMA gain fiber and the pump-combiner fibers and heat-sinking the Tm-gain fiber. Also, active cooling of the 35 W pump diodes allows pumping the amplifier close to 793 nm, where the maximum rated pump absorption in the gain fiber occurs. The length of the fiber between the TDFA output combiner and the ZBLAN fiber is kept at a minimum practically permissible length of ~0.5 m to reduce nonlinear losses in its ~10 µm diameter core. Approximately 55% coupling efficiency is observed at the mechanical splice from the TDFA output to the ZBLAN fiber due to the mode-mismatch between the ~10 µm core diameter combiner output fiber and the high-NA ZBLAN fiber with ~8 µm core diameter.

System component	Definition	Efficiency
790 nm pump diode	Electro-optic efficiency provided by manufacturer	~41%
Er:Yb mid-amp	1.55 μm output / 976 nm CW pump power	~17%
25 m SMF	Output >1.8 μm / Input power	~47%
LMA-TDFA	~2 μm output / 790 nm modulated pump power	~27%
Mechanical splice	Coupled ~2 μm / TDFA-output	~55%
>3.8 μm light shifting efficiency	Power beyond 3.8 μm / coupled ~2 μm power	~16%
SC generation efficiency	SC output/ coupled ~2 μm power	~59%

TDFA-pump to SC conversion efficiency = 0.27x0.55x0.59 = 9%
TDFA-pump to >3.8 μm conversion efficiency = 0.27x0.55x0.16 = 2.35%

Table 2.1. Efficiency of various components of the TDFA-pumped ZBLAN SC Mid-IR laser

The length of ZBLAN fiber used in the mid-IR SC generation is optimized for efficient generation of wavelengths beyond 3.8 μm. Three different lengths of ZBLAN fiber, 5.5 m, 8.5 m and 13 m, were used in the set-up. The power generated in wavelengths beyond 3.8 μm was measured as a function of the TDFA average output power at a fixed repetition rate of 500 kHz and the observed results are plotted in Fig. 2.14. It is observed that for the ~13 m length of ZBLAN fiber, the long wavelength power generation saturates at higher TDFA output powers, compared to the result from ~8.5 m length. On the other hand, the ~5.5 m length does not generate as much long wavelength power for the same amount of TDFA output power indicating lower long wavelength efficiency. Based on the result, we observe ~8.5 m length to be optimal for higher efficiency long wavelength generation. For longer lengths of ZBLAN, the longer wavelength components undergo additional attenuation in the excess length of ZBLAN fiber. In comparison, the 5.5 m length is found to be short of optimal length and would require higher peak power output from the TDFA to generate power in longer wavelengths more efficiently.

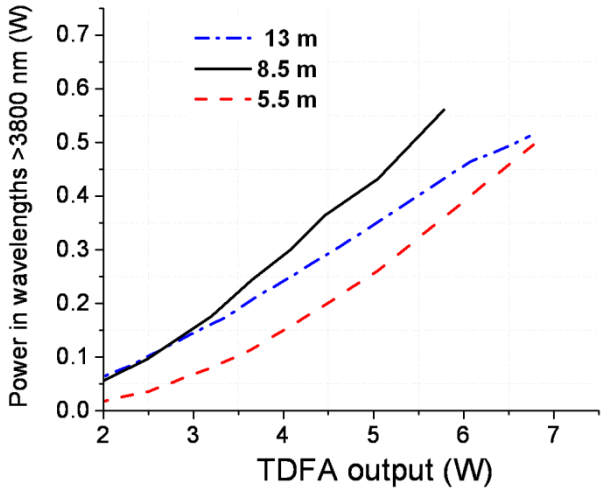

Fig. 2.14. Experimental optimization of power generation beyond 3.8 μm for various lengths of ZBLAN fibers

2.5.3. First stage optimization

The output from ~25 m length of standard SMF for various peak power settings of the 1.55 μm input pulse is shown in Fig. 2.15(a). Light generation in the TDFA gain band extending from ~1.75-2.1 μm is observed at input powers as low as ~1 kW with longer extending spectrum at higher peak powers. At ~2.5 kW peak power, a flat continuum extending from ~1.5-2.25 μm covering the entire TDFA gain band is obtained from ~25 m length standard SMF. Figure 2.15(b) shows the effect of the first stage input peak power on the spectrum output of ~12 m length of ZBLAN fiber for a fixed CW TDFA pump power of ~8 W. At low TDFA pump powers, the spectral extent of the ZBLAN output is found to be heavily dependent on the peak power used for 2 μm light generation. For example, the 1.5 kW peak power case used for 2 μm light generation yields the longest extending ZBLAN output spectra compared to the 2.5 kW case. However, the ASE peak from the TDFA in the ZBLAN output is ~8 times higher in the 1.5 kW case compared to 2.5 kW due to insufficient strength of the input signal in the TDFA gain band. Hence, even though the SC extends to beyond 4 μm at lower first stage peak powers, the efficiency of SC generation is poor in the 1-1.5 kW peak power cases.

Figure 2.15(c) shows the relative power in wavelengths >2.5 μm plotted against the peak power used at the input of the standard SMF. The result shows that higher spectral shifting efficiency is achieved at 2.5 kW peak power compared to lower peak powers with saturation observed beyond 2 kW. Above 2.5 kW, the standard SMF generates

additional components beyond 2.1 µm, which are not efficiently amplified in the TDFA. By pumping the TDFA with higher pump power, spectrum extending to 4.5 µm with ~97% pump depletion is obtained, as shown in Fig. 2.9 for first stage peak powers of ~2.5 kW to provide higher efficiency long wavelength generation. However, the demonstrated result shows the flexibility in extent of spectral generation in the two-step SC scheme based on the availability of pump power in the system and the application requirement.

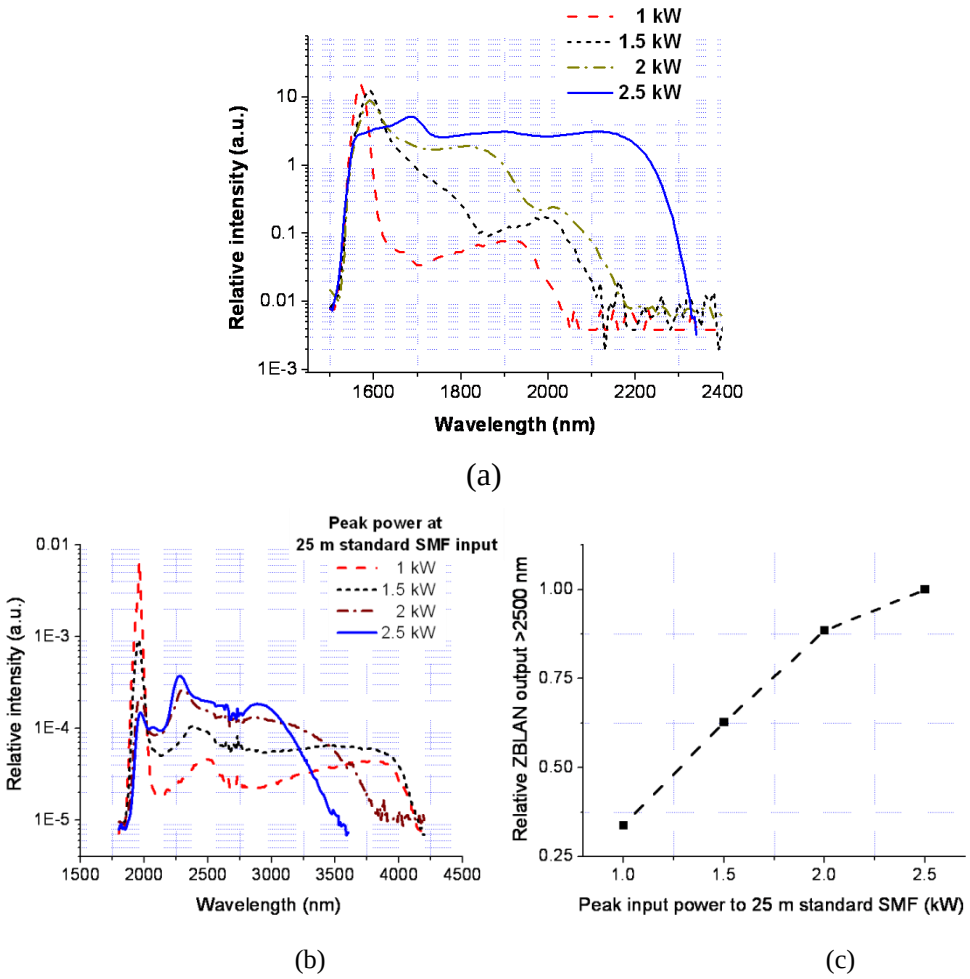

Fig. 2.15. Stage 1 peak power optimization (a) Output spectrum from ~25 m standard SMF for various peak input powers of 1.55 µm pulses, (b) 12 m ZBLAN output at ~8 W CW TDFA pump power for various 1.55 µm peak powers used in 2 µm light generation (c) Relative average power generated beyond 2.5 µm at output of ~12 m ZBLAN as a function of the stage 1 peak power for fixed TDFA pump power

Figure 2.16 shows the effect of the length of standard SMF used in the first stage on output spectrum from the ZBLAN fiber. Three lengths of standard SMF are used - 10m, 25m and 50m, and in each case, the 1.55 µm peak power is adjusted so that the same

average power (~0.6 W) is generated beyond 1.8 µm at the output of the fiber, measured using a power meter placed after a Ge long-pass filter. The standard SMF output is spliced to the LMA-TDFA and the output spectrum from ~8.5 m length of ZBLAN at ~20 W of pump power is measured in each case. Figure 9 shows that the SMF length used in the 2 µm light generation does not influence the extent of ZBLAN output as long as similar average powers are generated in the TDFA gain band at the output of the standard SMF. The observed result can be explained by the fact that since the standard SMF with ZDW ~1.3 µm, is pumped at 1.55 µm in the anomalous dispersion regime, soliton propagation is supported in the fiber from the balance of pulse broadening and compression through dispersion and fiber nonlinearities. Therefore, the soliton pulses at the output of 50 m length of standard SMF do not undergo much broadening compared to higher peak power pulses used in the generation of similar spectra from only 10 m length. Also, the dispersion length of the fiber is several kilometers for nanosecond long pulses in standard SMF and hence dispersive effects are not expected to be dominant. Hence the choice of SMF length can be made on the basis of ease of peak power generation from the Er:Yb mid-amp, with shorter fiber lengths requiring higher peak power pulses. Also, the low cost of standard SMF does not provide any incentive to using shorter fiber lengths and 25 m standard SMF length is chosen as optimal. The results indicate that in applications where remote delivery of the 2 µm light is required, the length of standard SMF can be chosen depending on the set-up requirements, without appreciable degradation in the performance of the mid-IR SC laser providing additional flexibility for practical applications.

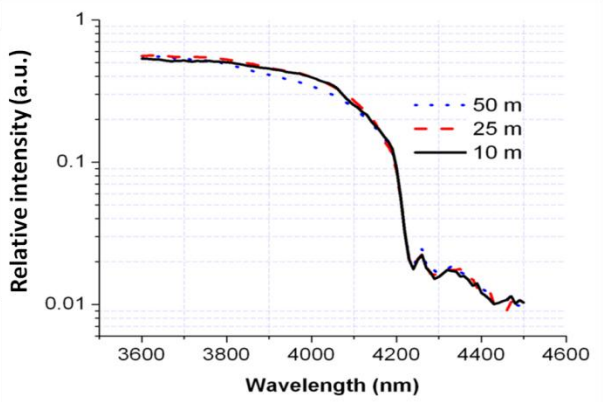

Fig. 2.16. ~8.5 m ZBLAN output at ~20 W TDFA pump power for various standard SMF lengths in the first stage

2.5.4. Small-core TDFA based mid-IR SC spectrum

The mid-IR SC spectrum from the small-core TDFA based set-up is shown in Fig. 2.17. The small-core TDFA (10/130 μm core/cladding diameter) is pumped with a maximum CW pump power of ~8 W with optimal settings in the first stage and a pulse repetition rate of 50 kHz. The TDFA output is mechanically spliced to ~12 m length of ZBLAN fiber. A spectrum extending from ~1.9-4.3 μm is obtained with ~300 mW average output power, of which ~85 mW lies in wavelengths beyond 3.8 μm. The peak in the observed spectrum at ~2 μm corresponds to the ASE generated in the amplifier and any un-depleted SC pump. The wiggles in the spectrum around 2.7 μm correspond to water vapor absorption and those at ~4.25 μm are due to CO_2 absorption in the air during propagation in the monochromator.

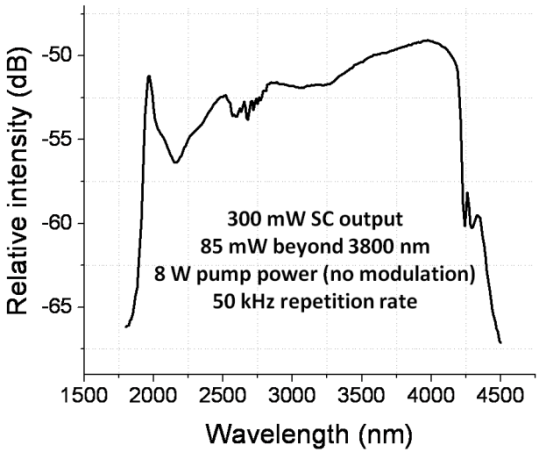

Fig. 2.17. Output spectrum from ~12 m length of ZBLAN fiber with spectrum extending from 1.9-4.5 μm

Compared to the LMA system, the small-core TDFA system shows less overall efficiency. For example, the efficiency in the generation of wavelengths beyond 3.8 μm with respect to the TDFA pump power is ~1.1% in the small-core system compared to ~2.35% observed in the LMA system. One of the main factors contributing to the lower efficiency of the small-core system is the higher nonlinearity in the amplifier. In the case of the above result, we observe ~15% pump-to-signal conversion efficiency in the small-core amplifier with respect to the coupled pump power. The higher nonlinearity in the small-core gain fiber leads to shifting of ~2 μm amplified pulses to longer wavelengths within the amplifier, which reduces the length of the gain fiber for which the input signal

lies spectrally in the amplifier gain band. Lower nonlinearity in the amplifier is also preferred to achieve efficient coupling to the ZBLAN fiber. For example, at 2.4 μm wavelength, the mode field diameter in the 10 μm core amplifier fiber is expected to increase to ~14 μm, which increases the free-space coupling loss to the 8 μm core ZBLAN fiber due to larger mode-area mismatch. The small-core TDFA system is also observed to be limited in its average power scaling capability with damage consistently observed at the combiner fiber and gain fiber splice at CW pump powers >26 W at 400 kHz pulse repetition rate. The set-up however, can be used for low power applications with passively cooled 790 nm pump lasers and a single small-core combiner for coupling in the pumps to provide for a simpler system design.

2.5.5. LMA-TDFA system characterization

The loss in the passive components of the system is characterized as shown in Fig. 2.18. As can be seen, an attenuated supercontinuum is coupled in to the input combiner fiber and the output after the two pump combiners, two gain fiber to combiner fiber splices and ~4.5 m length of 25/250 μm Tm-doped fiber is measured. By dividing the output spectrum with the input, the wavelength dependent system loss is measured and shown in the figure. The input spectrum is attenuated by ~15 dB to prevent any nonlinear effects in the amplifier. Two different splice times used in the splicing are shown in Fig. 2.18. The measured loss is a combination of the absorption in the gain fiber, combiner loss and splice loss. Loss due to absorption in fused silica fiber is accounted for by measuring the loss in a similar length of standard SMF as is used in the set-up. The results indicate a minimum loss of ~2 dB measured in the wavelength range from 2050- 2150 nm. At wavelengths below 2050 nm, the loss increases due to absorption in the Tm gain fiber. The two combiners used in the set-up have a rated insertion loss of 0.9 dB. Assuming identical splice losses in the combiner to gain fiber splices, the average splice loss is estimated to be ~0.55 dB each.

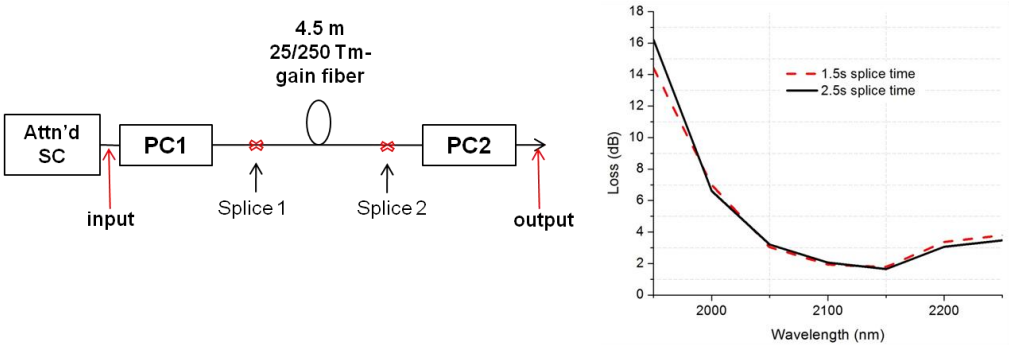

Fig. 2.18 Set-up and results of characterization of system loss for the assembled Gen-II Tm-amplifier

Further attempts to optimize the gain fiber to combiner splice were also made. The splicing process uses an Ericson FSU995FA model splicer, which has three fusion cycles during splicing. For the splicing of the large mode area fiber, only two fusion cycles are used. The first fusion cycle is fixed at a current of 13 mA and fusion time of 0.7 s. The fusion current and time of the second fusion cycle is varied and the performance of the amplifier is measured at 10 W of pump power. The results are shown in Fig. 2.19 below. In general, the splice performance for a number of different values of the fusion current and times is found to be similar as seen in the case for Fig. 2.18(b). However, at fusion current of 18 mA and fusion time of 3 s, consistently better performance is observed.

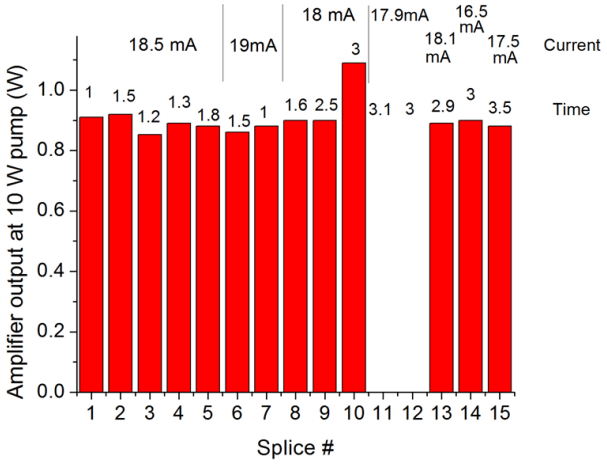

Fig. 2.19 Splice optimization from gain fiber to combiner by varying the splicing current and time and subsequently measuring the output of the amplifier at 10 W pump input

The amplifier performance is characterized at 1 MHz pulse repetition rate. The measured large mode area Tm-amplifier gain profile is shown in Fig. 2.20(a). The procedure used for gain profile measurement involves dividing the output spectrum for

various pump powers with the input spectrum. Fig. 2.20(b) shows the measured output power from the amplifier versus the input pump power. The result suggests a maximum slope efficiency of 38% from the amplifier.

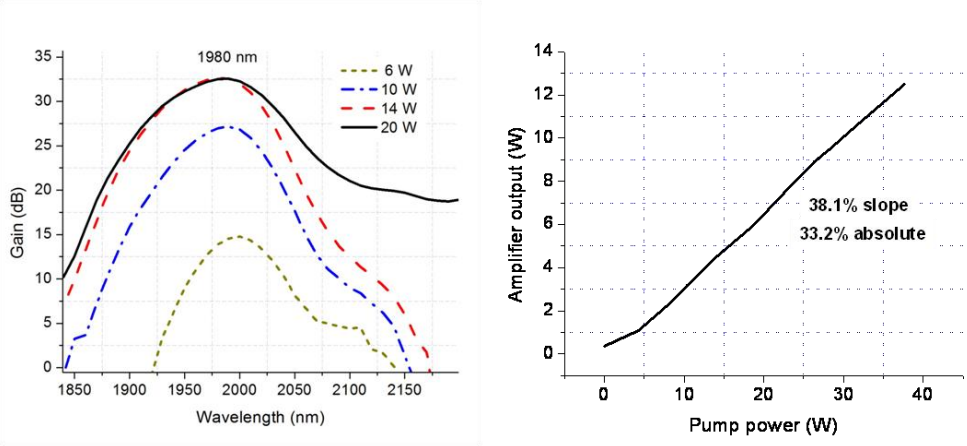

(a) (b)

Fig. 2.20 (a) Measured amplifier gain profile for supercontinuum input, (b) Amplifier performance for 1 MHz input repetition rate indicating maximum slope efficiency of 38.1%

The maximum observed slope efficiency for the large mode area amplifier is ~38.1% are shown in the figure above, which falls short of the observed performance measured by the fiber manufacturer Nufern. Up to 54% slope efficiency has been observed for similar fibers [40]. The observed gap is accounted for by the loss in the gain fiber to combiner splice, the output combiner, and the ~0.5 m length of combiner fiber at the output. The various losses and the projected efficiency are summarized in Table 2.3 below. As can be seen, up to 57% slope efficiency can be expected from the amplifier by eliminating losses in the gain fiber to combiner splice and the output combiner and nonlinearity in the ~0.5 m lengths of combiner fiber lead.

Component	Loss	Projected slope
Gain fiber to combiner splice	12%	43.8%
Output combiner	11.5%	50.4%
Spectrum shifting to 2.4 μm	10%	57%

Table 2.2 Gap between the measured slope efficiency and results presented by fiber manufacturer Nufern

As mentioned previously, to reduce the thermal load in the system and allow for practical applications, the supercontinuum output is modulated at 50% duty cycle with a

250 Hz square wave voltage. The modulation is implemented by switching the 35 W pump diodes on and off, causing the output of the amplifier to be modulated at 50% duty cycle. To confirm the modulation, the amplifier output is measured in the presence and absence of modulation as shown in Fig. 2.21. As can be seen, the output measured with modulation is slightly lower than half the output without modulation. This can be expected since modulation circuit does not turn on instantaneously with the positive voltage swing of the gate signal. Also, the amplifier takes finite time determined by the ~0.5 ms lifetime of the ions in the upper state before stimulated emission occurs [18]. These factors contribute to a duty cycle of ~45% at the output of the amplifier even though the electrical signal input is at 50% duty cycle. Such effects can be avoided by designing the electrical signal to have a duty cycle slightly larger than 50% so as to account for the lag in the turning on of the pump diodes and the amplifier output.

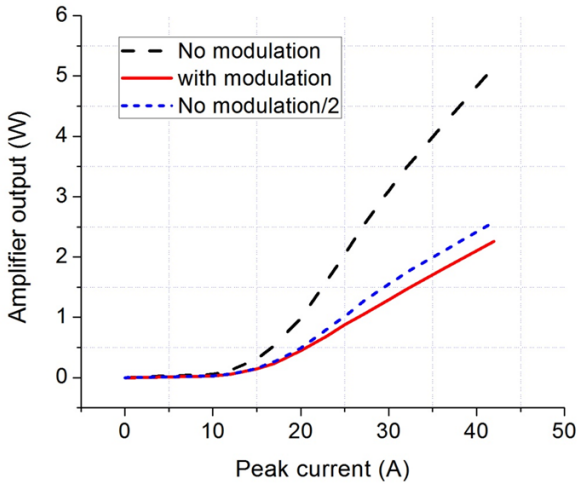

Fig. 2.21 Tm-amplifier output with and without modulation versus peak pump current

The output of the ZBLAN fiber in band IV wavelengths is also tested with and without modulation. With the pulse repetition rate set to 200 kHz, the output of 13 m length of ZBLAN is measured and shown in Fig. 2.22. As expected, the output with modulation is slightly less than 50% of the output without modulation. The result suggests that the output of the Tm-amplifier, ZBLAN and the band IV power scales similarly with modulation.

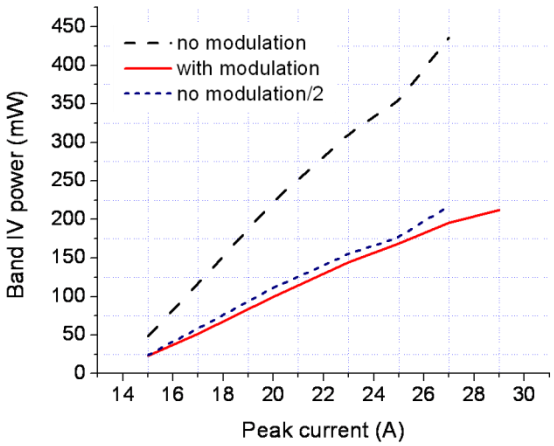

Fig. 2.22 Band IV power at the output of 13 m length of ZBLAN with and without modulation

2.6. Simulations

2.6.1. Simulator modeling

Simulations are performed to understand the optical processes associated with the two-stage TDFA-based SC system. In the fiber, the complex envelope *A(z,t)* of a pulse, under the slowly varying approximation satisfies the generalized nonlinear Schrödinger equation (GNLSE) given by [37],

$$\frac{\partial A}{\partial z} = (\hat{D} + \hat{N})A \tag{1}$$

with,

$$\hat{D} = -\frac{i}{2}\beta_2\frac{\partial^2 A}{\partial \tau^2} + \frac{1}{6}\beta_3\frac{\partial^3 A}{\partial \tau^3} + \frac{i}{24}\beta_4\frac{\partial^4 A}{\partial \tau^4} - \frac{\alpha}{2}$$

$$\hat{N} = i\gamma(1 + \frac{i}{\omega_0}\frac{\partial}{\partial t})\int_{-\infty}^{+\infty}[(1-f_R)\delta(t) + f_R h_R(t)]\,|A(z,t-t')|^2\,dt'$$

,

where the pulse moves along *z* in the retarded time frame $\tau = t - (z/v_g)$ with the central angular frequency of ω_0. The linear terms in the differential operator $\hat{D}$ account for the second (β_2), third (β_3) and the fourth order (β_4) dispersion as well as the loss (α) of the fiber. The terms in the operator $\hat{N}$ result from nonlinear interactions, which describe self-phase modulation, self-steepening and stimulated Raman scattering effects. In particular, the effective nonlinearity is defined as $\gamma = n_2\omega_0/cA_{eff}$, where n_2 and A_{eff} are the

nonlinear refractive index and effective mode area of the fiber respectively. In addition, $h_R(t)$ represents the Raman response function, and f_R is the fractional contribution of the Raman response to the nonlinear polarization.

The GNLSE described above is solved by a modified adaptive split-step Fourier method with the initial pulse shape as the known boundary value [31, 32]. The step size is determined and dynamically adjusted by the nonlinear gain in each section. Quasi-CW flat-top pulses with 80 ps FWHM are used as input in the simulator. A temporal window of 100 ps and spectral window of 333.33 THz is chosen to cover the entire SC spectrum corresponding to 2^{16} sampling points. The actual Raman shift spectrum of fused silica and ZBLAN fibers [26] is used in the simulations. The peak Raman gain coefficient (g_R) of fused silica fiber is set to 6.4×10^{-14} m/W at the center wavelength of 1553 nm [32] and that of ZBLAN fiber is set to ~2.2 times that of fused silica [25]. The dispersion parameters of the standard SMF are approximated based on the fiber datasheet and that of the ZBLAN fiber from the measured material dispersion [34]. For standard SMF, an effective nonlinear parameter of γ = 1.6 $W^{-1}km^{-1}$ is used at 1553 nm [32]. Since the n_2 of ZBLAN is ~0.85 times that of fused silica [24], an effective nonlinear parameter of 1.36 $W^{-1}km^{-1}$ is used for the ZBLAN fiber. The loss (α) in the standard SMF (Corning) and ZBLAN fiber (KDD FiberLabs) used in the simulations are as per provided by the fiber manufacturers. To account for the dispersion of the mode profile in the ZBLAN fiber at longer wavelengths, the Raman gain is scaled inversely with wavelength based on a linear dependence of the effective area on wavelength. Based on calculations, the effective area is expected to increase by ~1.45 times from 1.55 to 4 μm. The bend induced loss in the fiber is neglected due to the high NA and ~60 cm coiling diameter of the ZBLAN fiber in the experiments.

For modeling the TDFA, negative loss is assumed at wavelengths where gain is observed (1.95-2.13 μm). Experimentally measured TDFA gain profile is used in the simulations with peak gain observed at 1980 nm. The dispersion of the gain fiber is assumed to be same as that of standard SMF, while the nonlinearity parameters are scaled in proportion to the core diameter of the gain-fiber used in the experiments. In addition to the above components, the simulator also takes into account the effect of the pump-combiner output fiber pigtail and the mechanical splice loss observed from the pump-

combiner output fiber to ZBLAN fiber as observed experimentally. Figure 2.23 shows the block diagram of the simulation flow.

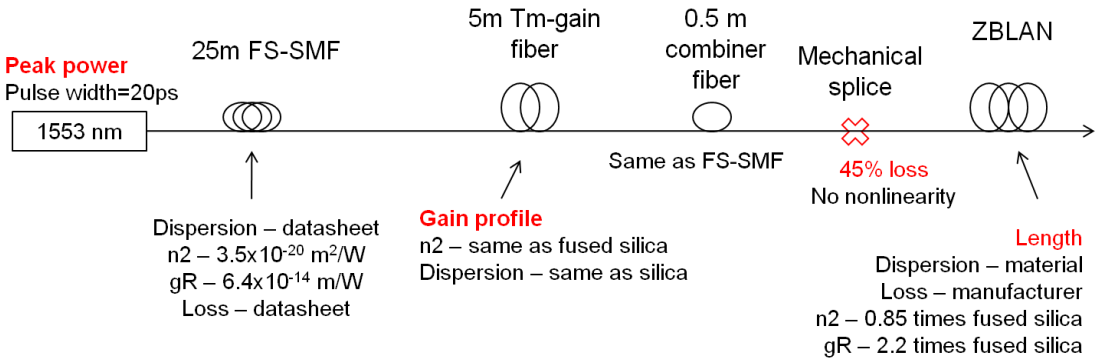

Fig. 2.23 System model for simulator depicting various components in the SC laser design

2.6.2. Simulation results

To verify the validity of the simulator, experimental results are compared to simulations. Figure 2.24 shows the comparison of output spectrum from 25 m length of standard SMF with 2.5 kW peak input power at 1553 nm as well as corresponding output from 8.5 m length of ZBLAN fiber with ~12 dB of power gain in the TDFA stage as observed in experiments. The figures show a single run of the simulation as well as an ensemble average of 12 simulation runs in comparison with the experimentally observed results. The single run simulation output has several spectral features due to the smaller pulse-width used in the simulation compared to experiments. Also, due to the averaging of the experimental spectral measurements with a lock-in time constant of 300 ms and 500 kHz system repetition rate, the measured spectrum shows ensemble average over 150,000 instances of the 1.55 µm input pulse. The ensemble average of 12 simulation runs shows a trend towards reduction in the fluctuations in the spectrum as observed in the experimental results. The output of the different simulation runs show variation due to the evolution of the spectrum from background noise. The simulation output is also averaged over ~2 nm intervals to resemble the monochromator resolution in the experimental measurements.

With ensemble averaging of the spectrum, reasonable agreement in terms of spectral extent between experiments and simulations is observed for both the standard SMF and ZBLAN output cases. For the case of the fused silica SMF (Fig. 2.24(a)), the simulation

output shows longer extension of the output spectrum compared to experimental results, which is attributed to the larger mode profile dispersion in standard SMF due to a numerical aperture of ~0.13. For the case of ZBLAN output in Fig. 2.24(b), the simulations show higher depletion of the SC pump at ~2 µm compared to experimental results. This is attributed to the fact that the ZBLAN fiber has a cut-off wavelength of ~2.75 µm, which suggests some of the coupled 2 µm light in to the ZBLAN fiber may not be in the fundamental mode. These components would not contribute to the spectral broadening process due to lower field intensity of higher order modes and hence remain un-depleted at the output of the ZBLAN fiber.

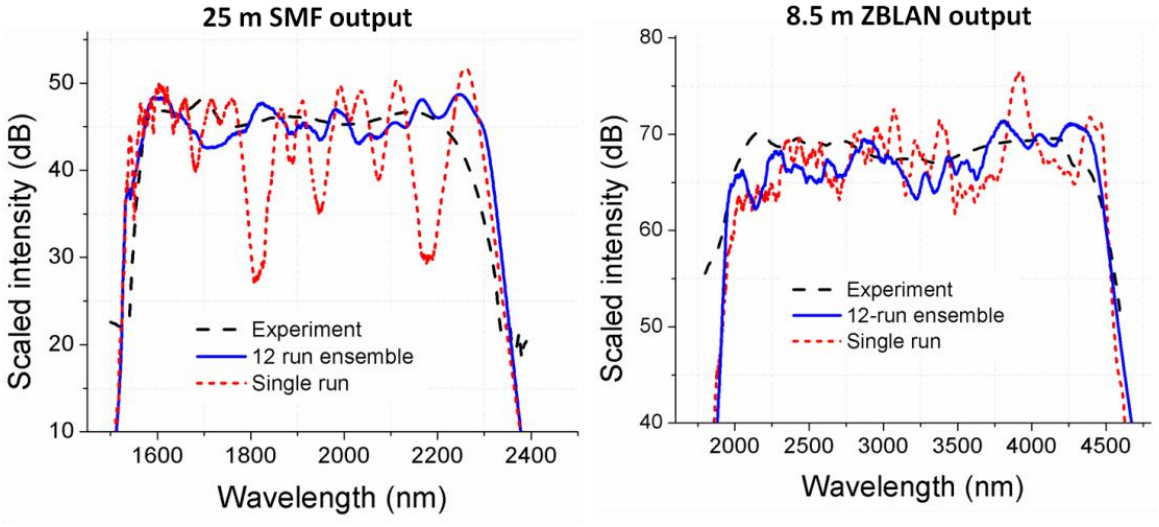

(a) (b)

Fig. 2.24 (a) Comparison of simulation vs. experimental result at the output of 25 m standard SMF with 2.5 kW peak input power pulses at 1553 nm, (b) Comparison of simulation vs. experimental result for the output of 8.5 m ZBLAN at 12 dB power gain in the TDFA

In experiments, the efficiency of long wavelength generation is observed to be dependent on the ZBLAN fiber length for a given TDFA output power level. Simulations are performed to confirm the observed experimental results. For example in Fig. 2.14, experimental results shows 8.5 m ZBLAN length to be more efficient in generation of wavelengths >3800 nm compared to 5.5 and 13 m ZBLAN lengths. Figure 2.25 shows the simulation results obtained for the relative power, i.e. area under the curve, beyond 3800 nm for 5.5, 8.5 and 13 m ZBLAN fiber lengths as a function of TDFA gain corresponding to ~3 W, ~5.2 W and ~7 W of experimentally measured power-amp

output. The observed results confirm a similar trend, where 8.5 m length shifts a larger fraction of the SC pump to wavelengths beyond 3800 nm.

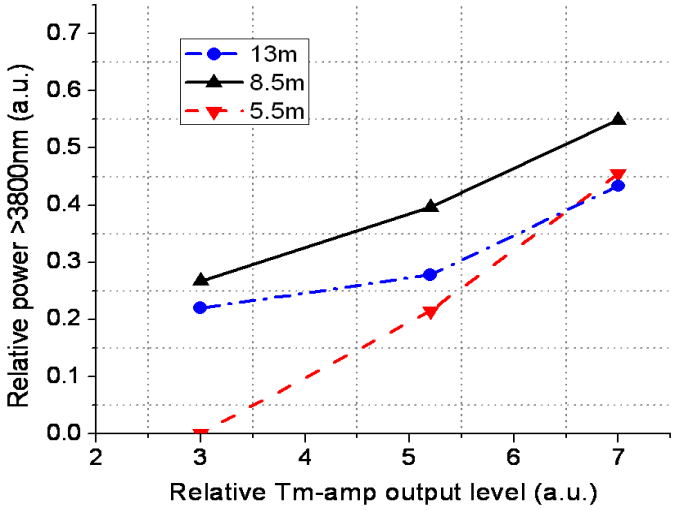

Fig. 2.25. Simulation results for confirming dependence of efficiency in long wavelength generation on ZBLAN length

Experimental results observed for the dependence on the 1.55 µm pulse peak powers on the 12 m ZBLAN output (Fig. 2.15(b)) contradict expectations. For a fixed amount of TDFA pump power, one would expect the input spectrum (Fig. 2.15(a)) corresponding to 2.5 kW peak power 1.55 µm pulses to give rise to the furthest extending spectrum. However, the observed results follow a trend that is opposite to this expectation. To verify the validity of the observed results, simulations are performed for two of the above measured cases. Fig. 2.26 compares the experimental and simulation results for the 1.5 kW and 2.5 kW, 1.55 µm pulse peak power cases. Simulation results match the observed experiments, whereby lower 1.55 µm peak power pulses lead to longer extension of the ZBLAN output spectrum. The explanation of this phenomenon is observed in the time-domain evolution of pulses in the TDFA, shown in Fig. 2.26. It is observed that in the time domain, for the case of 2.5 kW 1.55 µm peak power, more number of ~2 µm pulses evolve in the TDFA compared to the 1.5 kW case. As a result, the 2.5 kW 1.55 µm pulse peak power case generates, at the output of the TDFA, larger number of relatively low peak power ~2 µm pulses compared to the 1.5 kW case, which would explain the shorter extending spectrum out of the ZBLAN fiber compared to the 1.5 kW peak power case. Also, since the duty cycle in the 2.5 kW case is larger due to the presence of a larger

number of 2 µm pulses, the ASE generation can be expected to be lower, leading to larger pump depletion.

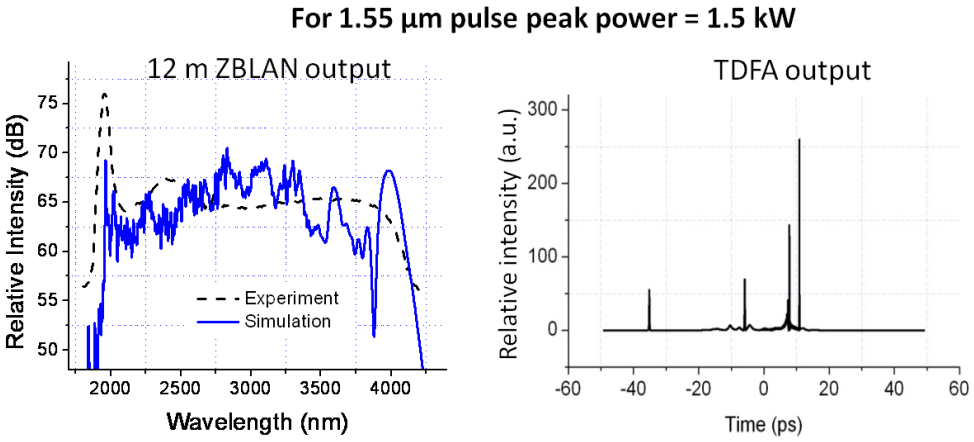

(a)

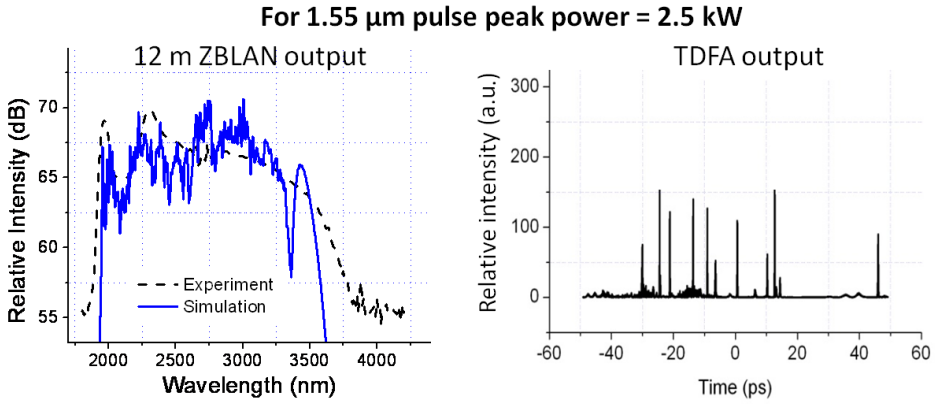

(b)

Fig. 2.26. Simulation results for 1.55 µm peak power dependence on ZBLAN output (a) Spectral domain comparison between simulation and experiments for 1.5 kW and corresponding TDFA output time-domain pulse profile (b) 2.5 kW peak power cases with ZBLAN spectral output comparison between experiments and simulations and corresponding TDFA output pulse profile

In experiments, the long wavelength edge of the TDFA mid-IR SC spectrum extends longer than that from the EYFA-based system. Simulations are performed to compare the output from 8.5 m length of ZBLAN fiber in the two systems. For the case of the EYFA system, input parameters used in [13], specifically, 20 kW peak power pulse at 1.55 µm is input to ~1 m length of standard SMF and the output is propagated through 8.5 m length of ZBLAN fiber after accounting for the mechanical splice loss. For the TDFA system, the single-run result shown in Fig. 2.24(b) is used. Figure 2.27(a) compares the output spectrum in the two cases, generating a spectrum at the output of the TDFA

system extending ~330 nm further than the EYFA systems as observed in experiments. Figure 2.27(b) shows the corresponding input pulse profile to the ZBLAN fiber in the two systems. In the EYFA system case, simulations suggest that the MI-initiated pulse break-up process in the 1 m length standard SMF after the Er:Yb amplifier stages gives rise to high peak power pulses responsible for long wavelength generation in the ZBLAN fiber. In the case of the TDFA system, simulations show that the amplification of wavelength shifted components in 25 m length of standard SMF around 2 μm yields a pulse profile with higher peak powers, which would explain the longer extending spectrum in the same length of ZBLAN fiber compared to the EYFA-based MISCL.

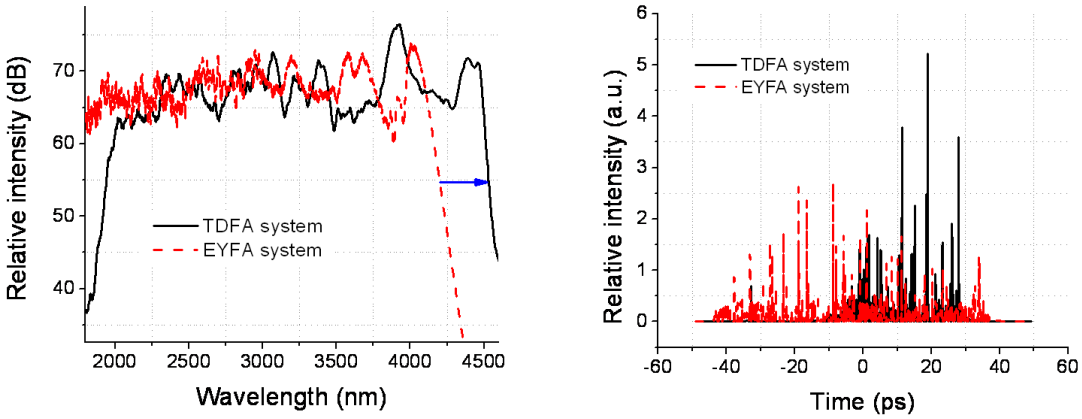

Fig. 2.27. (a) Simulation results comparing output spectrum of 8.5 m length of ZBLAN fiber for EYFA and TDFA systems, (b) Pulse profile comparison at the input of the ZBLAN fiber in the two power amp systems

The long wavelength edge of the TDFA-based mid-IR SC is experimentally found to be limited to ~4.5 μm as shown in Fig. 2.12. Based on the fiber specifications, the loss is the ZBLAN fiber is expected to be ~1 dB/m at 4.5 μm and the long wavelength edge seems to be loss-limited by the material absorption and poor confinement of longer wavelengths [12]. Simulations are performed to study the dependence of the loss profile of the ZBLAN fiber on the long wavelength edge. As shown in Fig. 2.28(a), three different loss profiles for the fiber displaced by around 200 nm from the manufacturer specifications is used in the simulator and the corresponding output from 10 m length of ZBLAN fiber is shown in Fig. 2.28(b). It is observed that the long wavelength edge of the SC spectrum shifts in accordance with the loss curve indicating that the SC long wavelength edge is limited by the loss in the ZBLAN fiber. For example, when the loss

profile is shifted to lower wavelengths by ~200 nm, the long wavelength edge reduces by ~206 nm. Similarly, shifting the loss curve towards the longer wavelengths causes the SC output to shift by ~160 nm. The slightly lower shift in the SC edge compared to a shift in the loss is attributed to the mode profile dispersion accounted in the simulations.

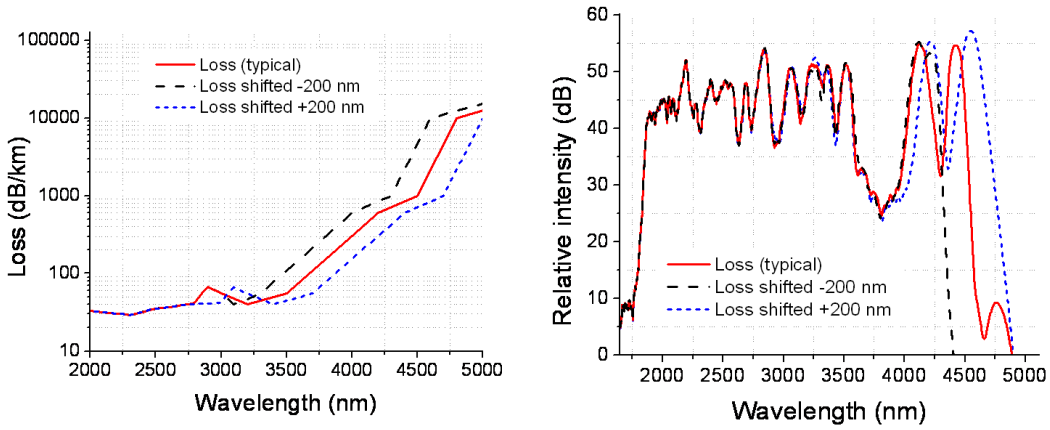

Fig. 2.28. (a) Input loss profile for ZBLAN fiber in to the simulator, (b) Corresponding output spectrum from 10 m length of ZBLAN fiber.

2.7. Discussion of results

The demonstrated TDFA-based mid-IR SC laser using a two-step nonlinear broadening set-up has several advantages. Firstly, it allows use of higher efficiency Tm-based systems compared to EYFAs. We have observed ~1.35 times higher pump-to-signal conversion efficiency in the large mode area TDFA compared to the Er:Yb power amplifier used in results demonstrated in [13]. Secondly, by shifting the SC pump to ~2 µm, longer extending spectrum is obtained compared to Er:Yb power-amp based system. Specific to the case of ZBLAN fibers with zero-dispersion wavelength ~1.65 µm, the TDFA system pumps the nonlinear medium in the anomalous dispersion regime and broadens spectrum more efficiently towards longer wavelengths through Raman processes. SC lasers pumped in the normal dispersion regime [9-13], in comparison, broaden the spectrum towards either direction with respect to the pump wavelength. By further optimizing the experimental parameters, ~2.5 times higher optical efficiency in generating wavelengths beyond 3.8 µm is achieved in the thulium-based mid-IR SC laser compared to previously demonstrated Er:Yb system [13].

The absolute efficiency of the LMA-TDFA seeded by fused silica SC is currently observed to be ~27% with respect to 790 nm pump power. The observed efficiency is considerably lower than published numbers for Tm-amplifiers. Particularly, for the 25/250 μm LMA gain fiber used in our experiments, absolute efficiency of ~53% has been demonstrated [40] in a CW lasing cavity configuration with respect to the launched pump power. In comparison, for our system, the signal loss in the splice at the gain fiber output end and the insertion loss of the output combiner currently amount to ~1 dB. In the absence of these losses, the expected TDFA efficiency is ~34.2%. Also, the generation of high peak powers leads to spectral broadening to ~2.5 μm in the ~0.5 m length of 10 μm core diameter fused silica fiber at the output of the pump-combiner. Due to the phonon losses associated with the spectral shifting process, ~11% reduction is observed in the power amp efficiency. The remainder of the gap in observed amplifier efficiency is attributed to the low duty cycle of the input signal to the amplifier. At 500 kHz pulse repetition rate with a 1-ns long 1.55 μm pulse, the system duty cycle is set to 1:2000 with respect to the TDFA pump. However, at the output of 25 m length of standard SMF, only a fraction of the 1.55 μm pulse shifts to the TDFA gain band, leading to lower 2 μm signal duty cycle. The low input duty cycle results in larger losses to spontaneous emission in the amplifier and currently reduces the efficiency of the system.

An optical efficiency of ~9% is demonstrated for the TDFA-based mid-IR laser in converting 790 nm pump light to SC. In comparison, a QCL operating at room-temperature generating 4.6 μm wavelength light with up to 8.8% wall-plug efficiency has been demonstrated [14]. Also, a $ZnGeP_2$-based OPO has been demonstrated with 22 W of output power in the 3-5 μm range and requiring 110 W of pump power yielding a 20% optical conversion efficiency [15]. Another mid-IR OPO has been demonstrated based on a periodically poled MgO-doped congruent $LiNbO_3$ crystal capable of generating 16.7 W at 3.84 μm starting from 110 W at 1064 nm (15.2% optical conversion efficiency) [16]. Table 2.4 summarizes the results of these mid-IR light generation technologies in comparison to the demonstrated TDFA-based SC laser.

Our results show mid-IR SC generation with efficiencies approaching that of other technologies can be achieved with some improvements. One of the main loss component in the current system is the ~45% loss in the mechanical splice from the

TDFA output to the ZBLAN fiber. Due to the dissimilar melting temperatures of fused silica and ZBLAN materials, fusion splicing of the two fibers is difficult. However, some preliminary work has been demonstrated in fused silica to fluoride fiber mechanical splices using a shape memory connector with losses as low as 0.8 dB at 1550 nm [41]. Incorporation of such a splice would increase the efficiency of the system by ~1.3 times. The splice loss from the LMA-gain fiber to the combiner fiber is currently estimated to be ~0.6 dB, which can be reduced by better control and uniformity of the fusion temperature, which could not be achieved by our two-electrode arc-based splicer. The insertion loss of the combiner is observed to be ~0.4 dB and agrees with specifications provided by the manufacturer. Another approach to increasing the efficiency of the SC laser is by increasing the repetition rate of the 1.55 μm pulses. By increasing the duty cycle of the input pulses, higher amplifier efficiency can be achieved by reducing losses to spontaneous emission in the gain fiber. However, operation at higher repetition rates would also require more pump power and better thermal management to prevent damage to components due to increase in the average power levels in the system.

Technology	Ref.	Demonstrated Wavelength	Average Power level	Demonstrated Efficiency	Advantages/ Disadvantages
Quantum cascade laser	[14]	4.6 μm	1.5 W	8.8% (wall-plug)	High efficiency/ Single wavelength
ZGP-OPO pumped by hybrid Tm:fiber laser/ Ho:YAG laser	[15]	3-5 μm tunable	22 W	20% (to 790 nm pump)	High average power, tunable/ Free-space optics
PPMgO-OPO pumped by Q-switched Nd:YAG laser	[16]	3.85 μm	16.7 W	15% (to Nd:YAG pump)	High average power/ High beam M^2
TDFA-based Mid-IR SC		2-4.5 μm	2.6 W	9% (to 790 nm pump)	Broad wavelength, No moving parts, remote fiber delivery/ Lower efficiency

Table 2.3. Comparison of TDFA-based mid-IR SC laser efficiency with other mid-IR lasers

Compared to the EYFA-system, the Tm-based system generates a spectrum extending ~270 nm towards the longer wavelengths. Based on the simulation results shown in Fig. 2.27, we attribute the longer spectral edge to higher peak power pulses at the output of the TDFA compared to MI-initiated pulse break-up in 1 m length of standard SMF following a Er:Yb power amplifier. The long wavelength edge of the SC spectrum obtained from the TDFA-based MISCL is limited to ~4.5 μm as observed in Fig. 2.12.

Due to pumping of the ZBLAN fiber in the anomalous dispersion regime, spectral broadening is dominantly Raman-induced soliton self-frequency shifting as evidenced by the asymmetry of the spectrum around the 2 μm SC pump (Fig. 2.9). Based on the theoretical model proposed in [12] for MI-initiated Raman-based SC generation processes in step-index ZBLAN fibers, the edge of the SC is limited by the absorption loss in the fiber and the bend-induced loss. By using a fiber with a high numerical aperture of ~0.27 and coiling the fiber around a ~60 cm diameter cylinder, the effect of bend-induced loss is eliminated based on the calculations presented in [12], where negligible bend-induced loss is calculated for a ZBLAN fiber with comparable geometry. Using simulations we studied the effect of the absorption edge of the ZBLAN fiber on the SC edge. By shifting the loss edge, we observe a similar trend in the edge of the generated SC showing that the long wavelength edge of the SC is largely dominated by the material loss in the fiber.

One approach for longer wavelength generation using the TDFA-based high peak power source entails use of higher nonlinearity fibers. A tellurite PCF with ~10x the Raman gain coefficient compared to ZBLAN [25] and only 1.7 μm^2 mode-field area has been demonstrated as a candidate for spectral generation up to ~4.8 μm with ~17 kW peak power 1.55 μm pulses coupled in to ~0.8 cm length of fiber with ~50% efficiency [10]. The results in Fig. 2.11 indicate that the TDFA-based 2 μm source should generate spectrum extending beyond 4.5 μm in suitable tellurite PCFs since we have shown further extending spectrum compared to EYFA-system with ~20 kW peak power generation capabilities. However, to the best of our knowledge, maximum average power handling of only ~1.12 W in a 18 μm solid core tellurite fiber has been demonstrated to date [39].

2.8. Summary

I have demonstrated an all-fiber integrated, power scalable mid-IR SC laser based on a thulium-doped power amplifier stage. The laser generates a continuous spectrum extending from ~1.9-4.5 μm in ~8.5 m length of high NA ZBLAN fiber with a core/cladding diameter of ~8/125 μm. Time-average power output of up to ~2.6 W with ~50% modulation is measured with ~0.7 W power in wavelengths beyond 3.8 μm.

An overall efficiency of ~9% is achieved in conversion of the 790 nm TDFA pump power to the SC output by optimizing the power-amp stage and the length of the ZBLAN fiber in the set-up. Compared to previously demonstrated Er:Yb based systems, ~2.5 times higher efficiency is observed in the conversion of power-amp pump to wavelengths >3.8 μm due to higher power-amp stage efficiency and shifting of SC pump to the mid-IR. Approximately 270 nm further extending spectrum in the mid-IR is also obtained by generating higher peak power pulses at the output of the TDFA as shown by the simulation results.

The novelty of our approach lies in the two-step SC generation. 2.5 kW peak power laser diode pulses at 1.55 μm are first shifted to beyond 2 μm in ~25 m length of low near-IR loss standard SMF, based on modulation instability-initiated SC generation process. The first stage SC is followed by a thulium-based large mode area fiber amplifier, which provides gain for the ~2 μm wavelength components. Coupling the TDFA output to low mid-IR loss ZBLAN fiber gives rise to a second SC generating stage extending up to ~4.5 μm wavelength. Dependence of the parameters used in the generation of the first stage SC on the ZBLAN output were studied and optimized for increased long wavelength generation efficiency of the laser. Scaling of the SC average output power was also demonstrated, whereby similar spectral extent at increasing average powers is achieved by proportionately increasing the pulse repetition rate. Numerical simulations were also presented to verify the observed results, which indicate the long wavelength edge of the SC to be limited by the high absorption in the ZBLAN fiber beyond 4.5 μm.

The demonstrated fused silica SC-seeded TDFA system provides an alternative to mode-locked lasers at 2 μm for mid-IR light generation, while using all commercial off-the-shelf parts. The achieved optical efficiency in SC generation is currently limited by the high mechanical splice loss from the TDFA output fiber to the ZBLAN fiber and the low duty cycle of the input signal. With further optimization of these factors, mid-IR SC light generation with efficiency comparable to competing technologies such as OPOs can be achieved using TDFAs.

References

[1] P. S. Edwards, D. M. Brown, A. M. Wyant, Z. Liu, and C. R. Philbrick, "Atmospheric Absorption Spectroscopy Using Supercontinuum Lasers," in *Conference on Lasers and Electro-Optics/International Quantum Electronics Conference*, OSA Technical Digest (CD) (Optical Society of America, 2009), paper CFJ3S.

[2] S. T. Sanders, "A wavelength-agile source for broadband sensing," Appl. Phys. B 75, 799-802 (2002)

[3] H. Li, D. A. Harris, B. Xu, P. J. Wrzesinski, V. V. Lozovoy, and M. Dantus, "Standoff and arms-length detection of chemical with single-beam coherent anti-Stokes Raman scattering," Appl. Opt. **48**, B17-B22 (2009)

[4] C. R. Philbrick, D. M. Brown, A. H. Willitsford, P. S. Edwards, A. M. Wyant, Z. Z. Liu, C. T. Chadwick, and H. Hallen, "Remote sensing of chemical species in the atmosphere," Fourth Symposium on Lidar Atmospheric Applications, 11-15 January 2009, Phoenix, Arizona

[5] K. –D. F. Büchter, H. Herrmann, C. Langrock, M. M. Fejer, and W. Sohler, "All-optical Ti:PPLN wavelength conversion modules for free-space optical transmission links in the mid-infrared," Opt. Lett. **34**, 470-472 (2009)

[6] I. T. Sorokina and K. L. Vodopyanov (Eds.), *Solid-state mid-infrared laser sources*, Springer-Verlag, Berlin Heidelberg 2003.

[7] Craig M. Payne (Ed.), Principles of Naval Weapons systems, 2nd Ed., Annapolis, MD, Naval Institute Press, 2010

[8] O. Malis, C. Gmachl, D. L. Sivco, L. N. Pfeiffer, A. M. Sergent, and K. W. West, "The quantum cascade laser: A versatile high-power semiconductor laser for mid-infrared applications," Bell Labs Technical Journal 10(3), 199-214 (2005)

[9] G. Qin, X. Yan, C. Kito, M. Liao, C. Chaudhari, T. Suzuki, and Y. Ohishi, "Ultrabroadband supercontinuum generation from ultraviolet to 6.28 μm in a fluoride fiber," Appl. Phys. Lett, 95, 161103 (2009)

[10] P. Domachuk, N. A. Wolchover, M. Cronin-Golomb, A. Wang, A. K. George, C. M. B. Cordeiro, J. C. Knight, and F. G. Omenetto, "Over 4000 nm bandwidth of mid-IR supercontinuum generation in sub-centimeter segments of highly nonlinear tellurite PCFs," Opt. Express **16**, 7161-7168 (2008)

[11] C. Xia, M. Kumar, O. P. Kulkarni, M. N. Islam, F. L. Terry, Jr., M. J. Freeman, M. Poulain, and G. Mazé, "Mid-infrared supercontinuum generation to 4.5 μm in ZBLAN fluoride fibers by nanosecond diode pumping," Opt. Lett. 31, 2553-2555 (2006)

[12] C. Xia, Z. Xu, M. N. Islam, F. L. Terry, Jr., M. J. Freeman, A. Zakel, and J. Mauricio, "10.5 W time-averaged power mid-IR supercontinuum generation extending beyond 4 μm with direct pulse pattern modulation," IEEE J. of Sel. Top. Quantum Electron., Vol. 15, No. 2, March/April 2009

[13] M. Kumar, V. Alexander, M. J. Freeman, M. N. Islam, F. L. Terry, Jr., in preparation, 2011

[14] A. Lyakh, C. Pflügl, L. Diehl, Q. J. Wang, F. Capasso, X. J. Wang, J. Y. Fan, T. Tanbun-Ek, R. Maulini, A. Tsekoun, R. Go, C. Kumar, and N. Patel, "1.6 W high wall plug efficiency, continuous-wave room temperature quantum cascade laser emitting at 4.6 μm," Appl. Phys. Lett. 92, 111110 (2008)

[15] E. Lippert, H. Fonnum, G. Arisholm, and K. Stenersen, "A 22-watt mid-infrared optical parametric oscillator with V-shaped 3-mirror ring resonator," Opt. Express **18**, 26475-26483 (2010)
[16] Y. Peng, W. Wang, X. Wei, and D. Li, "High-efficiency mid-infrared optical parametric oscillator based on PPMgO:CLN," Opt. Lett. **34**, 2897-2899 (2009)
[17] P. F. Moulton, G. A. Rines, E. V. Slobodtchikov, K. F. Wall, G. Frith, N. Samson, A. L. G. Carter, "Tm-Doped Fiber Lasers: Fundamentals and Power Scaling," *Selected Topics in Quantum Electronics, IEEE Journal of* , vol.15, no.1, pp.85-92, Jan. 2009
[18] Stuart D. Jackson and Terence A. King, "Theoretical Modeling of Tm-Doped Silica Fiber Lasers," J. Lightwave Technol. **17**, 948- (1999)
[19] J. C. Jasapara, M. J. Andrejco, A. D. Yablon, J. W. Nicholson, C. Headley, and D. DiGiovanni, "Picosecond pulse amplification in a core-pumped large-mode-area erbium fiber," Opt. Lett. **32**, 2429-2431 (2007)
[20] G. Imeshev and M. Fermann, "230-kW peak power femtosecond pulses from a high power tunable source based on amplification in Tm-doped fiber," Opt. Express **13**, 7424-7431 (2005)
[21] K. Kieu, F. W. Wise, "Soliton Thulium-Doped Fiber Laser With Carbon Nanotube Saturable Absorber," *Photonics Technology Letters, IEEE* , vol.21, no.3, pp.128-130, Feb.1, 2009
[22] P. T. Rakich, Y. Fink, and M. Soljačić, "Efficient mid-IR spectral generation via spontaneous fifth-order cascaded-Raman amplification in silica fibers," Opt. Lett. **33**, 1690-1692 (2008)
[23] Min Jiang and Parviz Tayebati, "Stable 10 ns, kilowatt peak-power pulse generation from a gain-switched Tm-doped fiber laser," Opt. Lett. **32**, 1797-1799 (2007)
[24] X. Zhu and N. Peyghambarian, "High-Power ZBLAN Glass Fiber Lasers: Review and Prospect," Advances in OptoElectronics, vol. 2010, Article ID 501956, 23 pages, 2010
[25] M. D. O'Donnell, K. Richardson, R. Stolen, C. Rivero, T. Cardinal, M. Couzi, D. Furniss, A. B. Seddon, "Raman gain of selected tellurite glasses for IR fibre lasers calculated from spontaneous scattering spectra," Optical Materials, Volume 30, Issue 6, February 2008, Pages 946-951
[26] A. Saissy, J. Botineau, L. Macon, and G. Maze, "Raman scattering in a fluorozirconate glass optical fiber," J. De Physique Lettres 46, 289-294 (1985)
[27] B. Srinivasan, M. Erlandsson, G. S. Feller, E. W, Mies, R. K. Jain, "Reproducible fusion splicing of low melting point (fluoride) optical fibers with the use of a stable heat source," Optical Fiber Communication, Conference on , vol., no., pp.1-2, 16-21 Feb 1997
[28] G. Genty, J. M. Dudley, C. M. de Sterke, A. Judge, B. J. Eggleton, O. Bang, "Optical rogue waves and soliton turbulence in nonlinear fibre optics," *Lasers and Electro-Optics 2009 and the European Quantum Electronics Conference, European Conference on*, vol., no., pp.1, 14-19 June 2009
[29] B. C. Stuart, M. D. Feit, A. M. Rubenchik, B. W. Shore, and M. D. Perry, "Laser-induced damage in dielectrics with nanosecond to subpicosecond pulses," Phys. Rev. Lett. 74, 2248–2251 (1995)
[30] *Nufern* website (*http://www.nufern.com/whitepapers.php*)

[31] G. Chang, T. B. Norris, H. G. Winful, "Optimization of supercontinuum generation in photonic crystal fibers for pulse compression," Opt. Letters **28**, 546-548 (2003)
[32] C. Xia, M. Kumar, M. –Y. Cheng, R. S. Hegde, M. N. Islam, A. Galvanauskas, H. G. Winful, F. L. Terry, Jr., M. J. Freeman, M. Poulain, and G. Mazé, "Power scalable mid-infrared supercontinuum generation in ZBLAN fluoride fibers with up to 1.3 watts time-averaged power," Opt. Express **15**, 865-871 (2007)
[33] Corning website (*http://www.corning.com/opticalfiber/products/SMF-28_ULL_fiber.aspx*)
[34] J. A. Harrington, *Infrared fibers and their applications*, SPIE Press Book, 2004
[35] KDD Fiberlabs website (*http://www.fiberlabs-inc.com/fluorideFiber.htm*)
[36] X. Yan, G. Qin, M. Liao, T. Suzuki, Y. Ohishi, "Transient Raman response and soliton self-frequency shift in tellurite microstructured fiber," Journal of Applied Physics, vol.108, no.12, pp.123110-123110-5, Dec 2010
[37] G. P. Agrawal, *Nonlinear Fiber Optics,* 3rd edition, (Academic, San Diego, 2001).
[38] D. Buccoliero, H. Steffensen, E. –H. Ole, M. Heike, M. Tanya, "Thulium pumped high power supercontinuum in loss-determined optimum lengths of tellurite photonic crystal fiber," Applied Physics Letters, vol.97, no.6, pp.061106-061106-3, Aug 2010
[39] K. Li, G. Zhang, and L. Hu, "Watt-level ~2μm laser output in Tm^{3+}-doped tungsten tellurite glass double-cladding fiber," Opt. Lett. **35**, 4136-4138 (2010)
[40] G. P. Frith and D. G. Lancaster, "Power scalable and efficient 790-nm pumped Tm^{3+}-doped fiber lasers", Proc. SPIE 6102, 610208 (2006)
[41] D. Faucher, A. Fraser, P. Zivojinovic, X. P. Godmaire, É. Weynant, M. Bernier, and R. Vallée, "High power handling shape memory alloy optical fiber connector," Appl. Opt. **48**, 5664-5667 (2009)
[42] S. Tokita, M. Hirokane, M. Murakami, S. Shimizu, M. Hashida, and S. Sakabe, "Stable 10 W Er:ZBLAN fiber laser operating at 2.71–2.88μm," Opt. Lett. **35**, 3943-3945 (2010)
[43] K. Tankala, B. Samson, A. Carter, J. Farroni, D. Machewirth, N. Jacobson, U. Manyam, A. Sanchez, M-Y. Chen, A. Galvanauskas, W. Torruellas and Y. Chen, "New developments in high power eye-safe LMA fibers", Proc. SPIE 6102, 610206 (2006)

Chapter III

Broadband, surface-normal optical modulator based on free-carrier effect in GaAs

Since the past few decades, the bottleneck in the field of high-speed network delivery has concentrated in the user access network. The access network has been defined in [1] as "the set of equipment connecting the subscriber unit to the equipment at the service provider's premise". There has been significant progress, technologically, in the long-haul and metropolitan area networks due to the maturity in high-speed optical networking system like SONET. But until recently, the single most crucial reason for the existence of such a bottleneck has been the absence of any such technology in the local loop. However the advent of Passive Optical Network (PON) architectures has since the late 1990's been the single most effective attempt to solve the problem of the "last-mile". In this chapter I shall review the technological issues regarding implementation of passive optical networks. In particular, I shall look at a proposed architecture [2] to provide sharing of cost of optical components to bring down subscriber equipment cost, which is presently the most crucial feature hindering mass deployment of PONs.

3.1. Concepts in Optical Access Networks

The technological solutions that have to be adopted in an Access Network (AN) are basically different from other mainstream optical networks. Their basic requirements are defined by the scenario and telecom demands of the users. An AN typically covers a local area which is commonly in a distance of 10 km radius or shorter from a central Head-End of the local telecom service center and the information bandwidth that is expected to be transported over each link is between 10 Mbps and 1 Gbps [1].

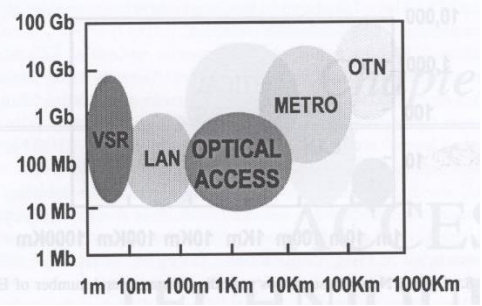

Fig. 3.1 Optical Network scenarios regarding distance and bit-rate

In this context, an Optical Access Network (OAN) corresponds to an implementation wherein, optical fiber technology is used in this last-mile to connect the user to the service-provider.

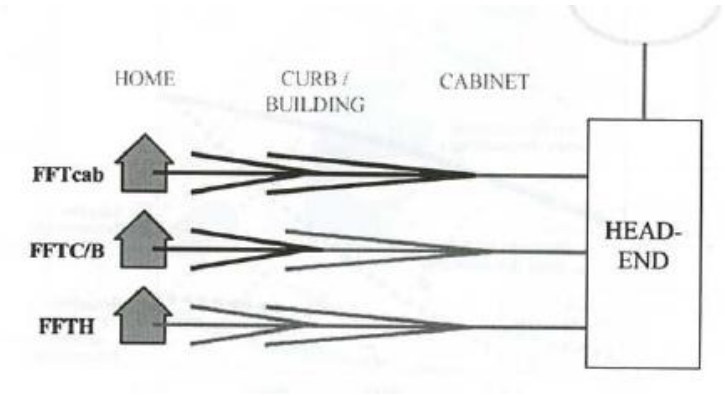

Fig. 3.2 Fiber/Copper Access Techniques

Several architectures came up one after the other as technological advances emerged in the field of optical networking. More importantly, the fiber has kept moving closer and closer to the user, until has finally reached the door-step. Some of these architectures are described in Fig. 3.2. Of these architectures, FTTH (fiber-to-the-home) has been effective in carrying the fiber right up to the user and thus delivering direct unlimited capacity link. The underlying basis of such FTTH architecture is a passive optical network. This simply implies a distribution network consisting of solely passive components thus bypassing the need of costly powering and maintenance of any such devices. This is responsible for making the PON architecture cost-effective as compared to laying new SONET-rings.

Figure 3.3 shows a simplified PON architecture. The network typically contains an Optical Line Termination (OLT) at the subscriber premise. A high bandwidth optical signal is sent on a single fiber access line and then optically split, using a passive optical splitter (POS) to multiple Optical Networking Units (ONUs). Each ONU

transmits/receives an independent optical channel and provides end users with dynamically allocated 1 Mbps-1Gbps of voice, data and video bandwidth. At the end of the network (the OLT and ONUs), both the upstream and downstream information flows are multiplexed into one fiber optic, using different wavelength for each direction, enabling a simultaneous transmission. In this case optical power is simply split amongst branches and sent to each ONU. This provides simpler implementation.

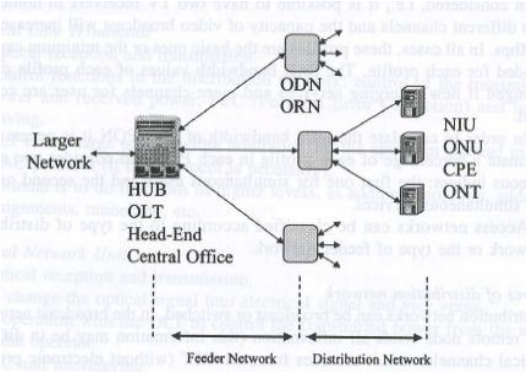

Fig. 3.3 General Structure of an optical access network

In the scheme of passive optical networks, information distribution can be carried out amongst multiple users on the basis of either time- or wavelength- division multiplexing. In the case of time-division multiplexed networks, synchronization amongst various users can add to operation complexity and also there is need for all users to carry equipment capable of operating at the aggregate channel capacity. In contrast, for the case of wavelength-division multiplexed (WDM) networks, various users operate on different wavelength channels making them transparent to others and every wavelength channel can operate at a speed independent of other users. However, the cost of components is higher for WDM-PONs, since every user requires a light source operating at a different wavelength and co-ordination between user wavelengths would increase the complexity of network operation.

One approach to reducing the cost of components in a WDM-PON is achieved by the architecture shown in Fig. 3.4. The central office (CO) in such a network would contain a single broadband light source, which provides a minimum of two wavelengths per user for the upstream and downstream communication channels. The upstream wavelength light is modulated over by a passive, reflective modulator at the user terminal and sent back to the central office. Cost reduction is achieved in this architecture by sharing a

single light source amongst multiple users and eliminating the need for active lasers at the user premises. For the shared light source, a multi-wavelength source with 1021 channels over 1525-1607 nm has been demonstrated in the past [3]. Broader SC light sources extending in the atmospheric transmission windows also allow for free-space communication applications for such networks. However a colorless modulator operating over a broad wavelength range is a key enabler for the implementation of such an architecture and allow for significant cost reduction.

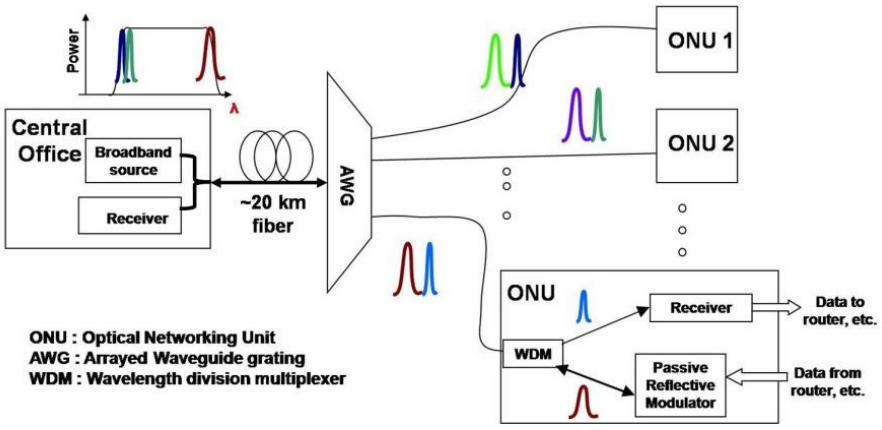

Fig. 3.4 Cost-shared architecture for WDM-PONs with single broadband light source at the central office and a passive, reflective modulator at each user premise

The achievable throughput from the system architecture shown in Fig. 3.4 depends on the modulation depth, insertion loss, operating speed and optical bandwidth of the modulator. The wavelength range of operation of the modulator limits the number of channels that can be supported by a single CO, whereas the speed of operation of the device limits the maximum bandwidth available to each user. The available modulation depth and insertion loss determine the maximum operating distance in order to achieve satisfactory bit-error rate performance. A variety of modulator solutions such as wavelength locked Fabry-Perot laser diodes [4], reflective semiconductor optical amplifiers [5], optical injection-locked VCSELs [6] and reflective electro-absorption modulators [7] have been investigated for the upstream communication channel from the user to the CO. They provide large modulation depth and operating speeds up to a few GHz. However, these solutions operate over less than 50 nm wavelength range, thereby limiting the number of users that can be connected to a single CO.

In this chapter, I will discuss my results of design, fabrication and characterization of a GaAs-based modulator operating on the principle of the free-carrier effect (FCE) in surface-normal geometry. The device consists of two forward biased *pin* diodes, which independently modulate the phase of two halves of an incident beam. By coupling the differentially phase modulated beam in to a single mode fiber (SMF), phase to amplitude modulation conversion is achieved using the mode-selectivity properties of standard SMF.

The choice of modulator technology for WDM-PON applications is governed by a number of operation constraints. For broad optical bandwidths the modulator needs to be non-resonant, thereby limiting the use of electro-absorption modulators due to their relatively narrow wavelength range of operation. The modulator also needs to be polarization independent since the polarization of the light received by the user is random, which presents penalty on use of electro-optic modulators. Other modulator technologies such as thermal, acousto-optic and micromechanical based solutions are also unsuitable due to limited operation speed capabilities. Based on these constraints, FCE is chosen for the modulator design.

FCE is a non-resonant effect that occurs in semiconductors above the band-edge wavelength due to the polarizability of charged carriers. Semiconductor devices based on the FCE have also been extensively studied as candidates for integrated optical components with the advantage of leveraging mature fabrication technology. Much of the focus in FCE modulators lately has been on waveguide devices due to their ability to provide high extinction ratios (>15 dB), and large operating speeds up to 40 Gbit/s, [8]. However, high packaging costs and operation in small, non-circular optical modes make waveguide devices unsuitable for low-cost and free-space optical networks [9].

Surface-normal optical modulators are also attractive for free-space as well as on-chip applications such as mobile optical communication links [10], optical signal processing arrays [11], chip-to-chip optical interconnects [12] and pulse-shaping [13]. Also, modulators capable of operation in the 2-2.4 μm wavelength region have applications in free-space systems due to the lower attenuation at these wavelengths in the atmosphere and their ability to pass through haze [14].

Amongst semiconductor-based surface-normal optical modulators, a MEMS device has been recently demonstrated with >15 dB contrast [15]. However, the device has limited operating speeds of ~1 MHz. Systems based on electro-absorption (EA) modulators are also under investigation [11] and results suggest high contrast ratio (~10 dB) with operating speeds >1 GHz. However, demonstrated tunability of EA modulators is only ~70 nm [16]. In comparison, FCE based devices are of interest due to their ability to operate over larger wavelength range.

In this chapter, I will discuss results on a FCE-based surface-normal optical modulator in GaAs. A Si-based FCE device has been demonstrated with 24% typical modulation depth and 60 MHz electrical bandwidth in the past [17]. However, theoretical studies predict larger phase shifts per unit length from the FCE in materials with smaller carrier effective masses such as GaAs compared to Si [18]. Techniques such as ion-implantation used in the fabrication of the Si-based device, are not suited for GaAs, due to the tendency of the GaAs crystal to decompose and emit arsenic at the high temperatures of 800-900°C required for these processes [19]. The demonstrated device is instead fabricated on n-type GaAs substrate with epitaxially grown p-type and intrinsic layers to avoid exposure of the device to high temperatures during processing.

3.2. Device design

The chosen modulator design is a *pin*-junction device based on the FCE, which occurs due to the polarizability of free carriers in semiconductors. The FCE is a non-resonant effect and occurs at wavelengths above the semiconductor band-gap, thus allowing modulation over a broad wavelength range. Also, FCE-based devices have been demonstrated to be polarization independent [17], making them suitable as remote external modulators. The operating speed of FCE-based modulators is determined by the lifetime of the carriers in long length devices and the carrier transit times in short length device, and hence can be designed to switch on the order of few nanoseconds.

Surface-normal geometry with free-space coupling is chosen for the modulator to ensure low fabrication and packaging costs. However, this limits the available interaction length between the incident light beam and the device active region. Since larger phase

shifts can be achieved by larger contrast in the carrier density, the *pin* diode needs to be operated in the forward biased mode.

Recombination of carriers in the diode invariably leads to generation of heat. Change in the junction temperature also leads to change in the device refractive index. In most semiconductors, the thermal effect is more dominant compared to the FCE, resulting in undesirable device operation at speeds below 100 kHz. To cancel out the thermal effect, split beam geometry, as shown in Fig. 3.5(a), is used in the modulator. Each of the two halves of the incident light beam is modulated separately by the two diodes while maintaining the same average current through each. As a result, both halves of the beam experience equal phase shifts due to the thermal effect. In addition to cancelling out the thermal effect, the dual diode structure can also be used to achieve a large amplitude change for a given phase shift in the incident light beam as outlined in Fig. 3.5(b), by using mode rejection properties of SM fibers [17]. In the absence of current through the diodes, a fixed $\pi/2$ phase shift is introduced between the two halves of the beam. As a result, when the beam is coupled back into the SM fiber, some higher order modes will be excited due to the non-uniform phase front of the reflected Gaussian beam. On the other hand, when the diodes are turned on, the differential phase shift between the two halves of the beam is reduced and the phase over the beam front is more uniform, leading to stronger coupling of the phase modulated light. In this way, phase-to-amplitude modulation conversion can be attained effectively.

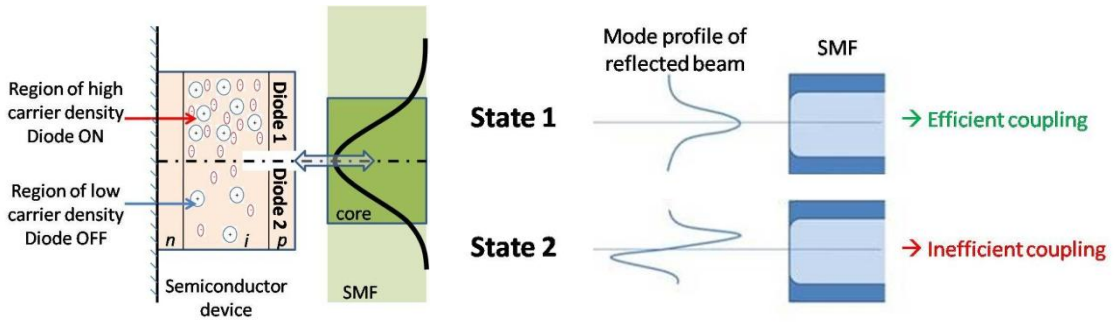

(a) (b)

Fig. 3.5 (a) Device schematic showing two-diode geometry for cancelling thermal effect (b) Phase to amplitude conversion using mode rejection property of SM fiber [17]

At near infrared wavelengths, the FCE can be modeled by Drude theory [18], where the induced phase shift in an incident light beam is given by,

$$\Delta\phi = -\frac{q^2\lambda}{4\pi c^2 \varepsilon_0 n}\left(\frac{\Delta N_e}{m_e^*} + \frac{\Delta N_h}{m_h^*}\right) \tag{3.1}$$

where, q - charge of electron

λ – wavelength of incident light

$\Delta N_{e,h}$ – change in electron (e) and hole (h) density

m_e^*, m_h^* - electron and hole effective mass.

Compared to Si, GaAs has smaller effective mass of carriers ($m_{e,h}^*$) [20], which should result in larger phase shift per unit length according to Eq. (3.1). The diodes are operated in forward biased mode, which makes the operation speed cutoff dependent on carrier diffusion time. The higher carrier mobility and twice as large carrier drift velocity in GaAs should make higher speed operation possible compared to Si. To verify these hypotheses, simulations were first performed to compare similar devices in the two material systems. The simulations were performed using Sentaurus Device simulator tool, which evaluates the charge continuity for the device structure to solve the Poisson's equation and develops a map of charged carrier density in the device.

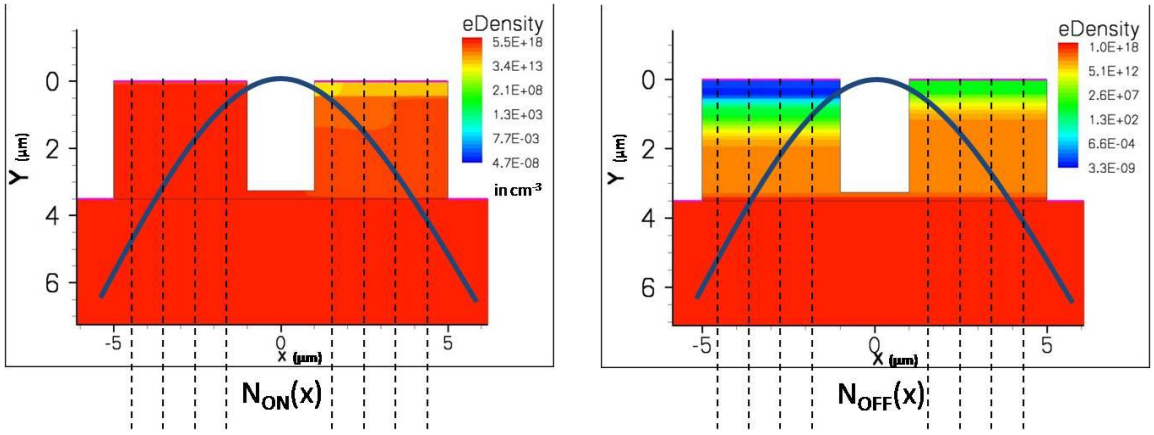

Fig. 3.6 Simulations showing the density of carriers when the diode is in on and off states; Phase shift is calculated at various points along the incident lowest order Gaussian beam and the mode overlap integral in the on and off states gives the resulting modulation depth

Figure 3.6 shows the procedure used to predict the response of the modulator. A device cross section of 10 µm is chosen to match the mode field diameter of the light beam coming out of a standard SMF at 1.55 µm. A 3 µm thick intrinsic region is used for

the diode to allow for reliable fabrication of the device, with thicker regions providing larger phase shifts at the expense of higher fabrication costs. Simulations with voltage signals of up to 1 GHz frequency are performed and the resulting peak carrier densities in the diode intrinsic region in the device on- and off-states are obtained. The phase shift experienced by the incident light beam along the wave front is then calculated using Eq. (3.1), with material parameters summarized in Table 3.1. The coupling efficiency to standard SMF is calculated by computing the Gaussian mode overlap integral in the on- and off- states of the device to give the expected modulation depth over a range of input frequencies.

Parameter	GaAs	Si
Refractive index at 1.55μm	3.37	3.45
Relative permittivity	13.1	11.8
Electron effective mass	$0.067m_e$	$0.9163m_e$
Hole effective mass	$0.5m_e$	$0.537m_e$

Table 3.1 Material parameters used for calculating expected modulator performance for GaAs and Si [20]

Figure 3.7(a) compares the simulation results for identical modulators in GaAs and Si. The results suggest an expected peak modulation depth of ~50% for the GaAs modulator and ~20% for a Si modulator in the 1550 nm region, implying ~2.5 times more modulation depth in GaAs compared to Si under similar bias conditions. The relative frequency response of the Si and GaAs modulators is compared in Fig. 3.7(b). The simulation results suggest the diffusion capacitance limited -3-dB cutoff frequency in GaAs to be ~600 MHz compared to ~350 MHz in the case of Si device, implying ~1.8 times larger theoretical operation bandwidth in GaAs.

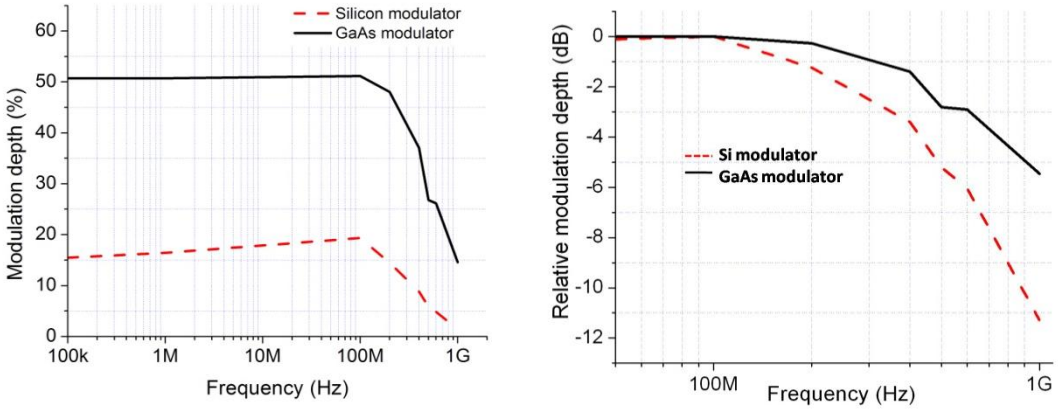

(a) (b)

Fig. 3.7 (a) Expected modulation depth vs. frequency for GaAs and Si modulator with the same structure, (b) Relative frequency response beyond 50 MHz for Si and GaAs modulators

Simulations predict device operation with 50% expected modulation depth and 600 MHz operation speed cutoff, which falls short of competing optical modulator technologies. However, unlike time-division multiplexed (TDM) systems shared by 32 or more users, devices for WDM-PON systems do not need to operate at the aggregate system speed of a few GHz. As a result, modulators operating at only a few hundreds of MHz can still provide higher throughput to individual users compared to TDM systems, with lower equipment costs. The required modulation depth for the modulator in WDM-PONs is set by the noise and signal attenuation in the communication channel. Compared to long-haul communication systems, the signal degradation in PONs is not severe due to lack of active components in the network and operation over short distances of ~20 km. Simulation studies, such as [21], suggest that $>10^{-9}$ bit-error rates can be achieved with ~3 dB modulation depth in ASK systems for power levels >-15 dBm at the receiver. Therefore the designed modulator can be used for short distance or local access network applications with the predicted performance.

3.3. Device fabrication

The device is fabricated on n-type substrate with epitaxially grown intrinsic and p-type layers with doping concentrations described in Table 3.2. Epitaxially grown p-type layer provides a sharp doping profile transition compared to ion-implantation techniques [19], and thus can provide larger free carrier density contrast in the intrinsic region. The device intrinsic layer thickness is chosen to be 3 μm to allow for reliable fabrication and keeping

fabrication costs low. Thicker layers can be used at the expense of increased epi-wafer costs.

Layer	Thickness	Doping concentration (cm^{-3})
n-type substrate	400 µm	1-4 x 10^{18} (Silicon)
Intrinsic layer	3 µm	< 1 x 10^{15}
p-type layer	0.5 µm	1 x 10^{20} (Carbon)

Table 3.2 Thickness of epitaxially grown layers and target doping concentrations

The schematic of the device based on the design factors discussed above is shown in Fig. 3.8. The device consists of two pin diodes of 4 µm x 10 µm cross section separated by a 2 µm trench for electrical isolation. The active region of the device is only ~3.5 µm with a total interaction length of 7 µm for the incident light, which is reflected from the metal contacts on the top of the device. Light is incident from the back of the device, where a phase-bias etch is provided to allow for π/2 phase shift between the two halves of the incident beam without any modulation signal. Such a scheme provides for maximum amplitude change for a given phase change. An anti-reflection (AR) coating reduces reflection of un-modulated light from the front incident layer. The n-type substrate is thinned down as much as possible as necessary for the mechanical stability of the device.

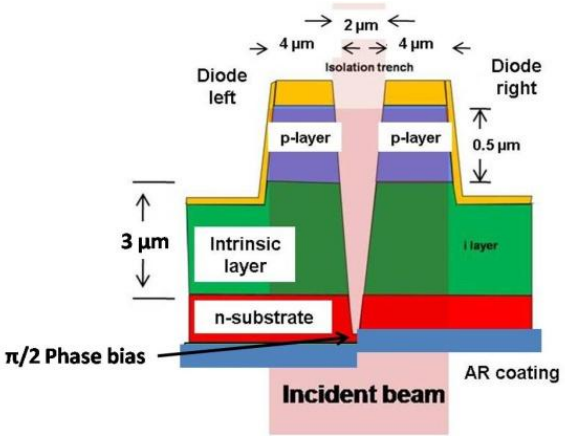

Fig. 3.8 Device schematic

The fabrication steps are shown in Fig. 3.9. Two p-type ohmic contacts of an alloy of Pd/Zn in the ratio 1:2 with dimensions of 10 µm x 4 µm each and separated by 2 µm are patterned on the wafer. Connecting pads to the p-contact with ~0.2 mm^2 area are laid down to allow for connections to external drive circuitry (Fig. 3.10(a)). The surface area

of the pads is an important factor that contributes to the parasitic capacitance of the device due to the only 3 μm thick intrinsic layer separating the highly conducting p- and n-type regions, and hence needs to be kept as small as possible. The semiconductor surface is then wet-etched until the buried n-type layer is exposed. Au/Ge eutectic contact to the n-type substrate is patterned by lift-off and the device is annealed at 400ºC after passivation to reduce the contact resistance.

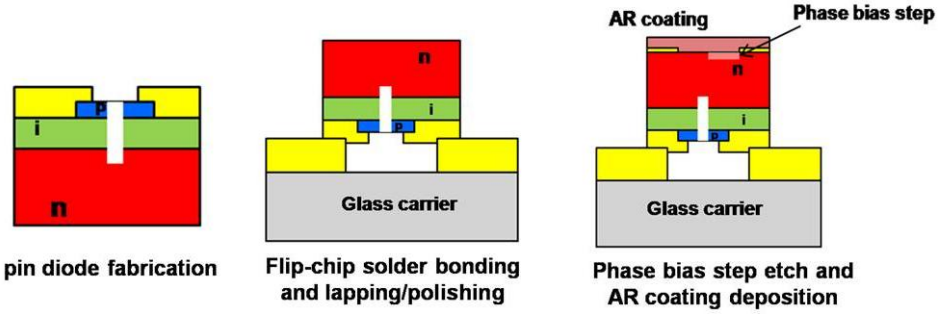

Fig. 3.9 Schematic of device fabrication steps

To reduce free-carrier absorption (FCA) of light in the highly doped substrate, provision in the fabrication needs to be made to allow for thinning down the substrate. To achieve this goal, the wafer is flip-chip bonded to a glass carrier before lapping operation (Fig. 3.9). Since the device has two diodes separated by only a 2 μm trench, conventional wafer bonding techniques cannot be used due to the possibility of shorting the two diodes at high process temperatures. Instead, I use solder bonding at ~200º C to mount the device onto a glass carrier while ensuring electrical isolation between the two diodes. The GaAs substrate is then thinned down to ~100 μm, with the glass carrier substrate providing mechanical strength for further device processing. Back-side aligning is used to define a device window on the exposed semiconductor surface as shown in Fig. 3.10(b).

Approximately 56 nm deep dry etch is performed on one half of the device window to achieve π/2 radians phase bias between the two halves of the incident light beam and a single layer anti-reflection (AR) coating of SiO is evaporated on to the device designed for an operation wavelength close to 1.55 μm.

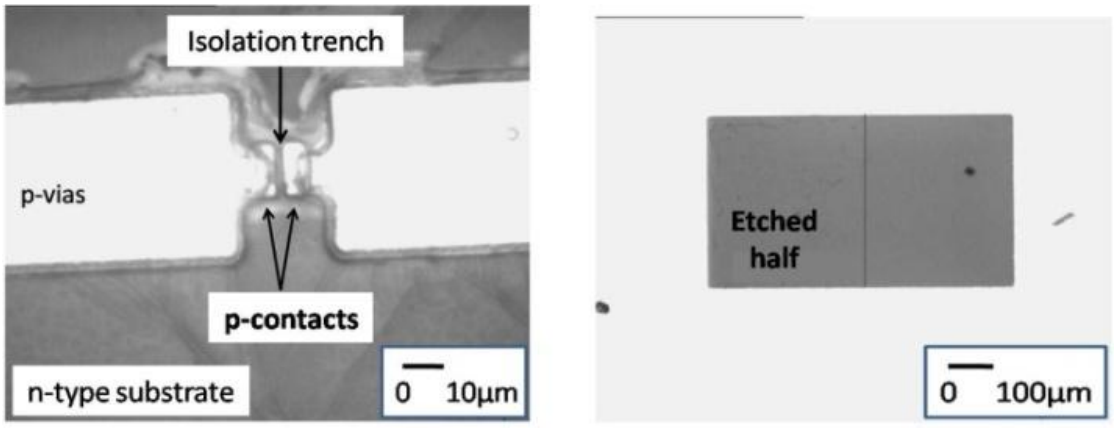

(a) (b)

Fig. 3.10 (a) Fabricated p-contacts and vias. The p-contacts are separated by a 2µm trench, (b) Front side device window with ~56 nm phase bias etch on one half of the window

3.4. Experimental set-up

Two optical sources are used in the device characterization experiments. A 1530 nm continuous wave distributed feedback (DFB) laser diode is used to measure the modulation depth, frequency response and insertion loss of the modulator. An amplified nanosecond pulsed SC source, as described in [22], is used to measure the wavelength response of the modulator. The SC source, as shown in Fig. 3.11, consists of a nanosecond pulse driven 1553 nm DFB laser diode with variable repetition rate followed by three stages of fiber amplifiers. Pulses amplified to ~4 kW peak power are coupled in to ~2 m of SMF followed by 6 m of high nonlinearity fused silica fiber with a zero dispersion wavelength of 1544 nm. The SC extends from ~900 nm to 2700 nm with ~165 mW average power.

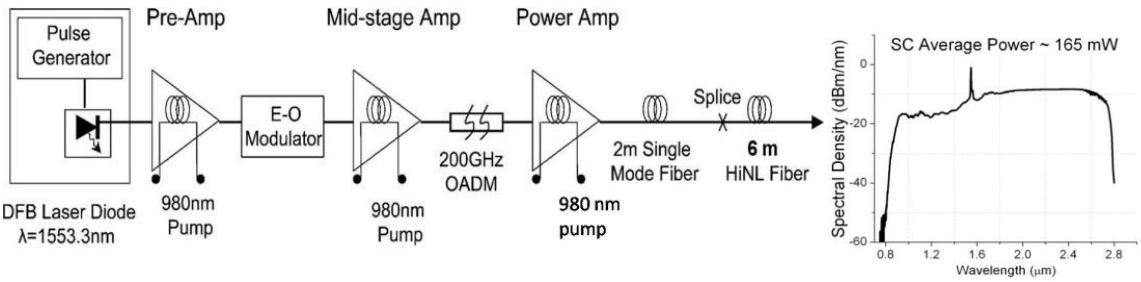

Fig. 3.11 Schematic of the SC source used for wavelength response measurement

The experimental set-up is shown in Fig. 3.12. An imaging spectrometer is placed in the beam path to select the wavelength of light. An AR coated CaF_2 50:50 beam splitter is used to direct light in and out of the modulator. Fused silica aspherical lenses are used

to focus light in to the modulator and the reflected modulated light in to 2 m long SMF. The detection system at the output end of the SMF consists of an InGaAs detector. For modulation depth measurement, a DC to 1 MHz variable-gain amplifier is used. The frequency response of the modulator is measured using a RF-amplifier with ~13 dB gain and a 2 GHz oscilloscope.

For measuring wavelength response, a pulsed SC source is used. To ensure overlap of the optical pulses and the modulating signal, the repetition rate of the SC source and the modulation signal are synchronized at 100 kHz. The modulated optical signal is detected by a strained InGaAs detector (0.8-2.6 μm operation) followed by a lock-in amplifier. The relative response of the modulator is measured by comparing the amplitude of the lock-in voltage normalized to the incident average power over the wavelength range of the source.

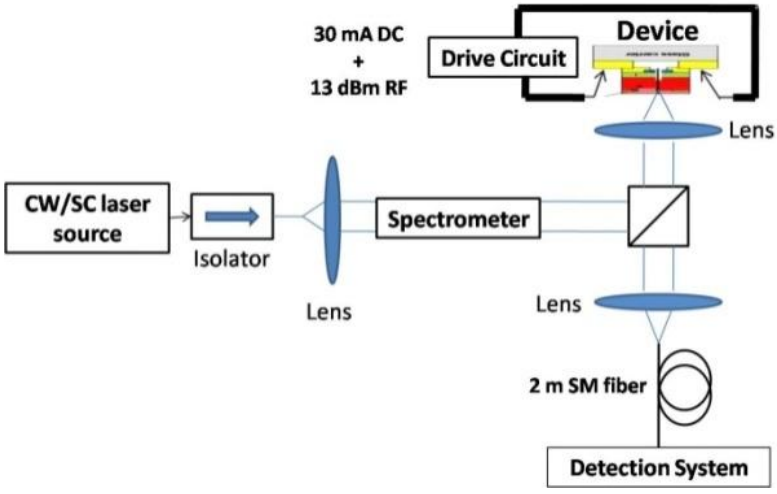

Fig. 3.12 Experimental set-up

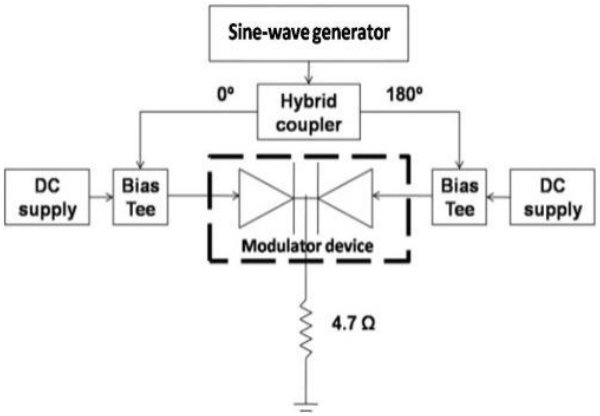

Fig. 3.13 Drive circuit schematic

The device is operated in a push-pull configuration and the drive circuitry is shown in Fig. 3.13. A sine wave generator is used to drive the input terminal of a hybrid coupler. The 180º out-of-phase outputs are fed to two bias tees which combine the AC signal with a DC bias current.

3.5. Experimental results

A maximum modulation depth of ~43% is observed with the 1530 nm DFB laser, as shown in Fig. 3.14, at a drive current of 30 mA DC + 20 mA AC rms current at 100 kHz. The overall insertion loss of the modulator is ~7 dB, comprised of ~3 dB coupling loss to SMF in addition to ~4 dB of device loss. For a substrate with ~4x10^{18} cm^{-3} doping concentration, the FCA coefficient is ~30 cm^{-1} [23], which corresponds to ~2.6 dB loss on double pass through a 100 µm substrate. The remaining 1.4 dB loss occurs due to light escaping through the isolation trench and diffraction of the beam.

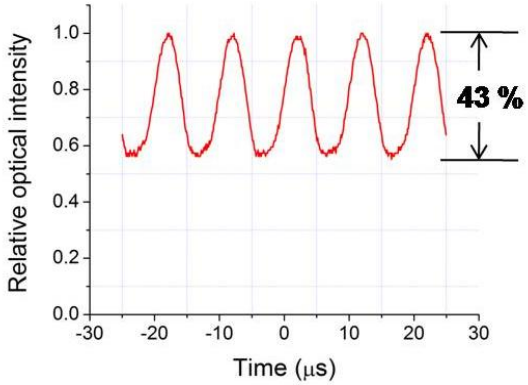

Fig. 3.14. Modulation depth measured with a 1530 nm continuous wave laser

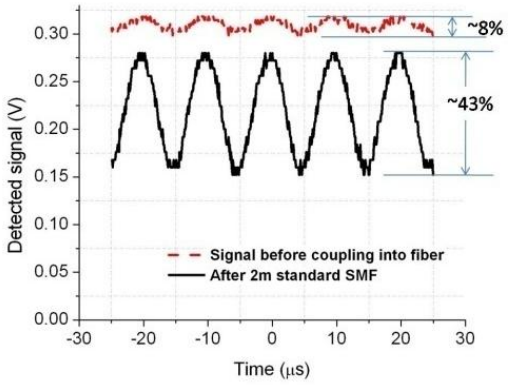

Fig. 3.15 Modulation depth before and after ~2 m SMF

Optical modulation is achieved in the modulator in two steps. First, the varying density of free carriers in the device active region produces a variable phase shift in the incident light beam. The resulting phase modulation is then converted to amplitude modulation by coupling to SMF. Fig. 3.15 gives evidence of the phase to amplitude conversion process by showing the observed modulation depth in the optical beam before and after the ~2 m long SMF in the set-up. The data suggests that before coupling in to the SMF, there is only ~8% modulation on the light amplitude, which occurs due to interference between the modulated light beam and the weak reflection from the AR coating interface. At the output end of the SMF, ~43% modulation depth is observed due to the mode selectivity of the fiber between the device on and off states as outlined in Fig. 3.5. However, the SMF also adds ~3 dB of coupling loss to the overall insertion loss of the modulator.

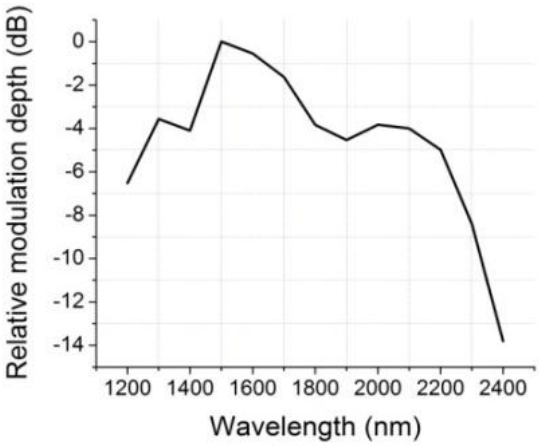

Fig. 3.16 Wavelength response measured using SC source

The wavelength response of the modulator, measured using the SC source is shown in Fig. 3.16. Modulation is observed over 1200-2400 nm with peak performance around 1500 nm and response falling off on either side. Our data suggests >1 dB modulation over 300 nm from 1450-1750 nm. Loss of modulation at the lower wavelengths is due to the cut-off wavelength of the SMF. Below 1200 nm, the fiber is multimode resulting in poor phase modulation to amplitude modulation conversion. At wavelengths above 2400 nm, the high absorption loss in the fiber prevents observation of modulation. The peak of the wavelength response around 1500 nm is due to the spectral characteristics of the single layer AR coating deposited on the device. Away from 1500 nm, the reflection from

the front surface of the device increases and causes the observed modulation depth to fall. Also, the phase bias etch of ~56 nm corresponds to an optimal $\pi/2$ radians phase difference between the two halves of the incident beam only around 1530 nm wavelength. Away from this wavelength, the available amplitude change for a given phase change reduces, leading to reduced modulation depth.

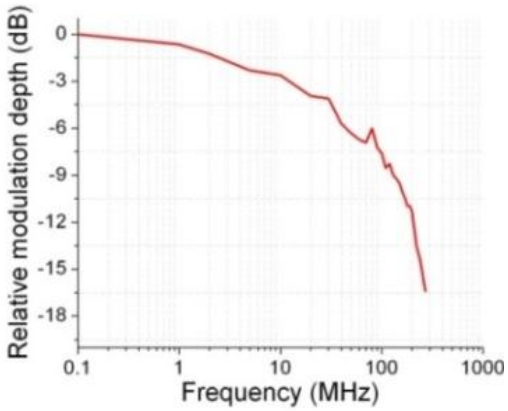

Fig. 3.17 Frequency response of the modulator

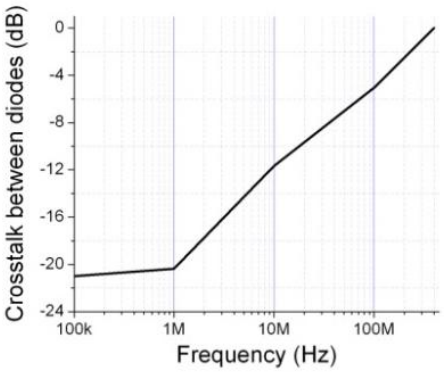

Fig. 3.18 Power coupled in diode 2 relative to power delivered to diode 1

The frequency response of the modulator is shown in Fig. 3.17. The relative modulation depth is measured by comparing the amplitude of the detected optical signal at higher frequencies compared to that at 100 kHz. We observe a 3-dB bandwidth of ~20 MHz and a maximum speed of operation of ~270 MHz. At higher frequencies, the modulation depth is too weak to be detected by the set-up. The degradation in the frequency response of the modulator beyond 20 MHz is attributed to poor RF isolation between the two diodes, which is confirmed by measuring the crosstalk between the two *pin* diodes versus frequency as shown in Fig. 3.18. The figure shows the relative power

parasitically coupled in to the neighboring diode versus input frequency. Below 20 MHz, the isolation between the two diodes is >-10 dB. However, at higher frequencies, more power from one diode leaks into the other, which results in the reduction of phase difference between the two halves of the incident light beam leading to the substantial drop in the observed frequency response.

The fabricated device has split beam geometry to reduce the dominant thermal effect observed at low frequencies. By operating the two diodes out of phase and with similar average currents, contribution of thermal effect to phase change can be made similar in both halves of the beam. To verify the hypothesis, the frequency response of the modulator was tested at low frequencies with single-arm and dual-arm drive configurations. As can be seen in Fig. 3.19, the response in the dual arm case is uniform over 50 Hz to 100 kHz compared to the steep fall in the frequency response of the single arm case. In the case of single arm operation, the refractive index in one of the device arms changes with the temperature of the active region determined by the instantaneous value of the current through the diode. For GaAs, the temperature coefficient of the refractive index (dn/dT) is ~2.24×10^{-4} K^{-1} [24], which can lead to up to 90% modulation depth as observed, for only ~25°C change in the junction temperature.

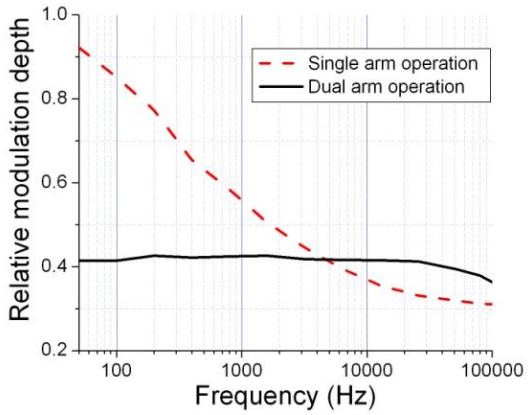

Fig. 3.19 Thermal effect cancellation by dual arm operation

3.6. Discussion

The measured results for the modulator frequency response are not in agreement with performance expected based on the simulations due to device parasitics. One of the main contributing factors to the device parasitics is the poor RF isolation between the two

diodes in the fabricated device. Better RF isolation requires better control over the etch profile of the isolation trench, which has an aspect ratio >2 due to a depth of ~4.5 μm and width of only 2 μm. A taper in the profile of the isolation trench can lead to higher capacitive coupling between the two diodes. Strong evidence is not available to verify this hypothesis due to the small size of the isolation trench. However, the tapering of the isolation trench can be attributed to the complex dependence of etch profiles on process parameters in dry etching.

The observed peak modulation depth of ~43% is in agreement with the expected modulation depth calculated from simulations. Calculations suggest observation of ~0.56 radians peak phase shift between the two arms of the modulator and the experimental data corresponds to ~0.46 radians. The variation can be attributed to the residual reflection from the AR coating interface. Larger modulation depth can be achieved by increasing the intrinsic region thickness. For example, simulations suggest that by increasing the device intrinsic region thickness to 6 μm, ~75% modulation depth can be achieved in theory. However this would result in a significant increase in epi-wafer costs.

The observed wavelength response of the modulator is strongly dependent on the spectral characteristics of the single layer AR coating deposited on the device. For device insertion losses of ~4 dB, analytical calculations suggest that when the front face reflectivity of the device exceeds ~20%, the un-modulated component in the reflected light is stronger and subsequently the observed modulation depth falls below 3 dB from the maximum. The 3-dB wavelength cutoff can be made larger by using broadband multilayered TiO_2/MgF_2 AR coating. The wavelength of operation for the modulator observed to be from 1200-2400 nm is limited by the properties of the SMF. The designed modulator consists of the *pin* junction device that produces a differential phase shift in the incident light beam, and the SMF provides subsequent phase modulation to amplitude modulation conversion. Hence, even though the *pin* device may produce a phase shift on the incident light beam at wavelengths down to the bandgap of GaAs (~870 nm) and beyond 2400 nm, amplitude modulation cannot be observed at these wavelengths due to the multimode behavior at shorter wavelengths and the high absorption at longer wavelengths in standard SMF. In the absence of the AR coating response and wavelength-dependent SMF properties such as mode field diameter and absorption, Eq.

(3.1) indicates that the phase shift due to free carriers should increase with wavelength. However, calculations suggest that due to the ~56 nm phase bias etch in the device design, the increased phase shift should not result in an appreciable increase in the observed modulation depth. For example, at 2.4 μm wavelength the phase-bias between the two halves of the beam is ~1 radian instead of the optimal $\pi/2$ radians necessary for maximum amplitude change for a given phase change. As a result, the expected modulation depth at 2.4 μm would increase only marginally to ~52% compared to ~50% at 1.55 μm in the presence of an ideal AR coating. However, due to the larger mode field diameter in SMF at 2.4 μm, the device insertion loss is also expected to be much higher. The analysis suggests that the wavelength response of the modulator should be largely governed by the spectral characteristics of the coating and the fiber properties.

Several feasible improvements would make the device attractive for practical applications in communication networks. The insertion loss of the modulator can be reduced by designing devices on semi-insulating substrates. Absorption loss in a 100 μm substrate with ~10^{16} cm^{-3} doping concentration should be less than 1 dB compared to ~2.6 dB in the ~1-4x10^{18} cm^{-3} n-type doping concentration of the substrate used in our fabrication. Better frequency response of the modulator can also be achieved by locating all contact pads onto a semi-insulating surface rather than highly doped GaAs substrate to reduce parasitic capacitance [19]. Vertical etch profiles in the isolation trench need to be achieved in order to minimize the crosstalk between the two *pin* diodes, which requires greater process control.

3.7. Summary

In summary, I have demonstrated an optical modulator with surface-normal geometry in GaAs based on the FCE. The modulator demonstrates a maximum modulation depth of ~43% obtained by varying the free carrier density across only 3 μm long device intrinsic region. The 3-dB modulation bandwidth is measured to be ~20 MHz and operation is demonstrated in conjunction with a broadband SC laser over a wavelength range of 1200-2400 nm.

Compared to a surface-normal modulator in Si, we observe ~1.8 times more modulation depth in half the interaction length in a GaAs modulator, largely due to the

superior electrical properties of GaAs as pertinent to FCE. Simulations suggest better speed performance for GaAs-based modulators compared to Si. However, higher modulation speeds could not be demonstrated due to poor RF isolation between the two differentially modulating *pin* diodes.

The modulator can be a potential low-cost solution for access systems with >50 nm centralized light sources. With colorless modulators that operate over a broad wavelength range, more channels can be provided by a single central office and hence lead to higher capacity systems with potentially lower costs. The modulator can also lead to applications in free-space communication systems where 2-2.4 μm wavelengths are used due to higher penetration of these wavelengths through the atmosphere, smoke and fog.

References

[1] J. Prat, P. E. Balaguer, J. M. Gené, O. Díaz, S. Figuerola, *Fiber-to-the-home Technologies*, Kluwer Academic Publishers (Boston, MA 2002)

[2] N.J. Frigo, P.P. Iannone, P.D. Magill, T.E. Darcie, M.M. Downs, B.N. Desai, U. Koren, T.L. Koch, C. Dragone, H.M. Presby, and G.E. Bodeep, "A wavelength-division multiplexed passive optical network with cost-shared components," IEEE Photon. Tech. Lts., Vol. 6, No. 11, November 1994

[3] B.C. Collings, M.L. Mitchell, L. Boivin, W.H. Knox, "A 1021 channel WDM system," IEEE Photon. Tech. Lts., Vol. 12, No. 7, July 2000

[4] K.-M. Choi, J.-S. Baik and C.-H. Lee, "Color-free operation of dense WDM-PON based on the wavelength-locked Fabry-Perot laser diodes injecting a low-noise BLS," IEEE Photon. Tech. Lts, Vol. 18, No. 10, May 2006

[5] T.-Y. Kim, S.-K. Han, "Reflective SOA-based bidirectional WDM-PON sharing optical source for up/downlink data and broadcasting transmission," IEEE Photon. Tech. Lts., Vol. 18, No. 22, November 2006

[6] E. Wong, X. Zhao, C.J. Chang-Hasnain, W. Hofmann, M.C. Amann, "Optically injection-locked 1.55-μm VCSELs as upstream transmitters in WDM-PONs," IEEE Photon. Tech. Lts., Vol. 18, No. 22, November 2006

[7] A. Garreau, J. Decobert, C. Kazmierski, M.-C. Cuisin, J.-G. Provost, H. Sillard, F. Blache, D. Carpentier, J. Landreau, P. Chanclou, "10Gbit/s amplified reflective electroabsorption modulator for colorless access networks," in Indium Phosphide and Related Materials Conference Proceedings, 2006 International Conference on, Publication Date: 7-11 May 2006

[8] S. Manipatruni, Q. Xu, and M. Lipson, " Breaking the Tradeoff between Speed and Extinction Ratio in Silicon Electro-Optic Modulators," in *Conference on Lasers and Electro-Optics/Quantum Electronics and Laser Science Conference and Photonic Applications Systems Technologies*, OSA Technical Digest Series (CD) (Optical Society of America, 2007), paper CTuG6

[9] N. C. Helman, J. E. Roth, D. P. Bour, and D. A. B. Miller, "Misalignment-tolerant surface-normal low-voltage modulator for optical interconnects at 1.55μm," in *Conference on Lasers and Electro-Optics/International Quantum Electronics Conference and Photonic Applications Systems Technologies*, Technical Digest (CD) (Optical Society of America, 2004), paper CThH4

[10] G. C. Gilbreath, W. S. Rabinovich, T. J. Meehan, M. J. Vilcheck, R. Mahon, R. Burris, M. Ferraro, I. Solkolsky, J. A. Vasquez, C. S. Bovais, K. Cochrell, K. C. Goins, R. Barbehenn, D. S. Katzer, K. Ikossi-Anastasiou, and M. J. Montes, ''Large-aperture multiple quantum well modulating retroreflector for free-space optical data transfer on unmanned aerial vehicles'', Opt. Eng., vol. 40, pp. 1348-1356, 2001

[11] B. Noharet, Q. Wang, S. Junique, D. Ågren, and S. Almqvist, "Multiple quantum well spatial light modulators for optical signal processing," Integrated Optical Devices, Nanostructures, and Displays, Proc. of SPIE, Vol. 5618, pp. 146-155, 2004

[12] H. Liu, C. C. Lin, and J. S. Harris, “High-speed, dual-function vertical cavity multiple quantum well modulators and photodetectors for optical interconnects,” Opt. Eng., vol. 40, pp. 1186–1191, 2001
[13] Y. Ding, R. M. Brubaker, D. D. Nolte, M. R. Melloch, and A. M. Weiner, “Femtosecond pulse shaping by dynamic holograms in photorefractive multiple quantum wells,” Opt. Lett., Vol. 22, pp. 718–720, 1997
[14] A. Arnulf, J. Bricard, E. Curé, and C. Véret, "Transmission by haze and fog in the spectral region 0.35 to 10 microns," J. Opt. Soc. Am., Vol. 47, pp. 491-497, 1957
[15] T. H. Stievater, D. Park, M. W. Pruessner, W. S. Rabinovich, S. Kanakaraju, and C. J. K. Richardson, "A microelectromechanically tunable asymmetric Fabry-Perot quantum well modulator at 1.55 μm," Opt. Express Vol. 16, pp. 16766-16773, 2008
[16] H. Mohseni, W. K. Chan, H. An, A. Ulmer, D. Capewell, “Tunable surface-normal modulators operating near 1550 nm with a high-extinction ratio at high temperatures,” IEEE Photonic. Tech. Lett., Vol. 18, No. 1, pp. 214-216, 2006
[17] O. Solgaard, A.A. Godil, B.R. Hemenway, D.M. Bloom, “All-silicon integrated optical modulator,” IEEE J. Sel. Area Comm. Vol. 9, No. 5, pp. 704-710, 1991
[18] B. R. Hemenway, “Integrated silicon light modulator for fiber-optic interconnects at 1.3 micron wavelength,” Stanford University dissertation, Ginzton Lab. Report #4703, May 1990
[19] R. E. Williams, *Gallium arsenide processing techniques* (Dedham, MA: Artech House, Inc. 1984)
[20] S. L. Chuang, *Physics of optoelectronics devices*. Wiley-Interscience publication 1995
[21] Sulur, T. Koonen, I. T. Monroy, H. de Waardt, “Combined modulation formats for IP over WDM networks supported by GMPLS,” International Union of Radio Science (URSI), General Assembly 2002, Session C4i.O.2 (1526)
[22] C. Xia, M. Kumar, M. –Y. Cheng, O. P. Kulkarni, M. N. Islam, A. Galvanauskas, F. L. Terry, Jr., M. J. Freeman, D. A. Nolan, and W. A. Wood, "Supercontinuum generation in silica fibers by amplified nanosecond laser diode pulses," IEEE J. Sel. Top. Quant. Elect. Vol. 13, No. 3, pp. 789-797, 2007
[23] W. G. Spitzer and J. M. Whelan, “Infrared absorption and electron effective mass in n-type gallium arsenide,” Phys. Rev. Vol. 114, pp. 59-63, 1959
[24] J. A. McCaulley, V. M. Donnelly, M. Vernon, and I. Taha, “Temperature dependence of the near-infrared refractive index of silicon, gallium arsenide, and indium phosphide,” Phys. Rev. B 49, 7408 - 7417 (1994)

Chapter IV

Optical Probe for Porosity Defect Detection on Inner Diameter Surfaces of Machined Bores

Porosity defects are formed during metal casting processes due to non-optimal process conditions such as casting pressure, cooling rates and parts geometry. Pockets of air-bubbles trapped inside the casting when exposed during a machining process appear as a surface deformity and pose a quality issue in cast components. Specifically, in the case of sealing surfaces such as spool bores in a transmission valve body, tight tolerances of within tens of microns need to be maintained between the bearing surfaces to provide isolation between adjacent channels [1]. As a result, surface macro-porosities with dimensions typically in the few hundreds of microns range are unacceptable to ensure good quality of manufactured parts. In addition, the occurrence of porosity on bearing surfaces can cause increased friction and wear, leading to adverse performance implications and even operation failure of automotive parts [2].

Currently, automotive manufacturing plants use manual inspection techniques on sampled parts for finding porosity defects [3]. Manual inspection is time and labor intensive, and also prevents any quantifiable data collection for studying trends in the porosity defects for manufactured batches. The inability to characterize the impact of porosity on proper part functioning leads to scrapping parts with any level of porosity present and hence, increased wastage of resources.

A number of non-contact techniques for porosity detection on machined surfaces have been demonstrated in the past. X-ray based techniques can be used to detect porosity on the surface as well as inside the bulk metal [4]. However, the technique is very expensive to implement on the plant floor and detection of inner porosity is not currently considered responsible for breakdown of parts, which makes the technique

excessive. Other non-destructive techniques such as eddy current based sensing ultrasonic testing, and pneumatic sensors have also been investigated in the past [2,5]. In comparison, optical techniques provide the ability to not only detect defects on the surface but also provide qualitative information on the nature of the defect with the help of image processing. For example, an optical inspection technique for detecting porosity on flat surfaces has been demonstrated [6] where images of suitably illuminated metal surfaces are captured, and processed using suitable algorithms to detect dark spots corresponding to porosity. The technique also uses detectors at two different angles to determine depth of the defect, thereby providing qualitative defect analysis and reducing system false alarm rates.

Detection of surface defects inside small bores using optical techniques presents unique challenges due to limited working space and non-flat inspection geometry. In the past, a computer vision based technique equipped with a robotic arm has been demonstrated for inspection inside bores [7]. More recently, an optical system utilizing a 360°-view line-scan algorithm and capable of in-line inspection speeds has also been presented to identify pores over 500 μm within 8-15 mm diameter bores [3]. However, computer vision based techniques are limited by the two-dimensionality of the acquired images. As a result, a qualitative distinction of detected surface defects becomes difficult, which can lead to high false alarm rates [2].

In this chapter, I present results on an optical-scattering based surface defect detection probe for small bores, which can also distinguish between porosity versus bump-type defects. The technique uses the spatial coherence of the light beam exiting a standard SMF at 1.55 μm wavelength. The ability to transport and focus the beam on to a tight spot provides a convenient tool for detecting surface defects and in addition allows for characterization of the defect based on a reproducible scattering signature. Specifically, the probe uses the difference in the scattering signature from a surface defect compared to the background surface and, hence, is applicable to most metal parts with surface roughness less than the wavelength of the incident light. In my approach, I use a focused beam of laser light at 1530 nm to illuminate the surface under inspection, and by using synchronous detection the effect of ambient light can be nullified. Based on the scattering signature in the specular and grazing directions, surface defects can not only be detected,

but also classified as entering into the metal surface or protruding out from the metal surface. The small cross-section of the probe allows for inspection of bores down to 5 mm diameter. Also, porosity as small as 50 μm in lateral dimension and ~40 μm deep can be detected with greater than 3-dB contrast to the background scattering intensity variation. The ability of the demonstrated system to detect porosity and distinguish it from bump-type defects can help to reduce the occurrence of false alarms during detection.

4.1. Experimental configuration and methodology

The probe uses a two-detector methodology to distinguish between porosity and bump defects. The system can integrate light scattering information along the specular and grazing directions to ascertain the nature of a defect on machined metal surfaces. Typical requirements for in-line inspection systems require ability to detect presence of porosity and provide location and dimensional information. The demonstrated system can provide such information and in addition can distinguish porosity from dust or metallic dirt particles on the metal surface to help reduce the occurrence of false alarms on the plant floor and increase robustness over current optical inspection techniques.

The probe consists of a fiber coupled 1530 nm distributed feedback laser diode as the light source. The choice of wavelength is determined by the root mean squared (RMS) roughness of a machined bore surface, which is typically specified between 0.01-0.8 μm [8]. At 1530 nm, the wavelength of the incident light is larger than the surface RMS roughness and, hence, a strong specular component in the reflection is observed at this wavelength from typical machined surfaces. Although cheaper light sources are available in the visible regime, light will scatter profusely for $\sigma/\lambda > 0.3$, where σ is the RMS roughness of the surface and λ is the wavelength of light [9], thereby reducing reflection in the specular direction for shorter wavelengths. On the other hand, telecom lasers also provide the convenience of being fiber coupled and, hence, can be located remotely with delivery provided by standard single mode fiber. In addition, they are available commercially and their eye-safe wavelength of operation allows for in-plant installation without causing operation hazards at milliwatt levels of powers.

A schematic of the designed probe is shown in Fig. 4.1. The light emerging from the fiber is collimated using a fused silica lens, and the beam is split using a beam splitter to allow for spatial separation between the incident light and the specularly reflected light, as shown in Fig. 4.1. A chopper assembly is introduced in the beam path to allow for reliable signal detection of the weakly scattered light in the grazing direction. The collimated light beam is focused onto a graded-index (GRIN) relay rod. The choice of the focusing lens in the set-up is based on the required Rayleigh range of the focal spot. Since the diameter of typical spool bores varies between 5-15 mm, a Rayleigh range of ~5 mm ensures that the beam spot incident on the ID surface is within square root of 2 times the spot at focus, thus eliminating the need for refocusing and motion of the probe relative to the bore axis. A Rayleigh range of 5 mm requires a spot size of ~50 μm at 1530 nm wavelength, which can be achieved by a lens with 50 mm focal length for a ~3 mm collimated beam. The relay rod is ~6 inches in length and 2.7 mm in diameter. By focusing the beam spot just inside one end of the lens, a similarly focused spot is obtained just outside the other face of the lens. A 90° prism is mounted at the end of the relay rod to deflect the beam and make it incident on the ID surface under inspection. The prism has a front face of 3.5 mm x 3.5 mm and is glued on to the GRIN relay rod using UV-cured optical adhesive. The GRIN lens rod is mounted at the center of a rotation stage to allow for 360° rotation about its axis, thereby eliminating the need to rotate the fiber and focusing lens assembly. The entire probe set-up is mounted on a translation stage to allow for motion in and out of the spool bores.

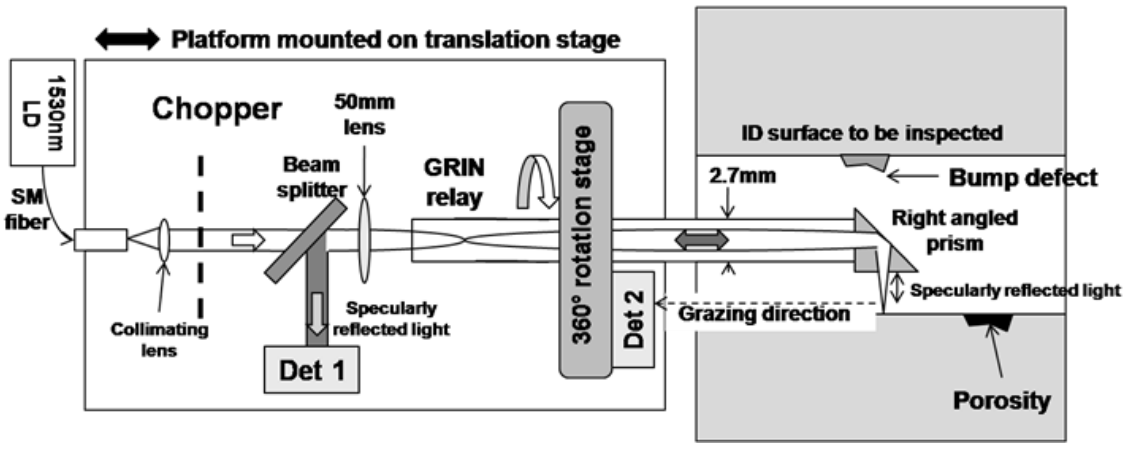

Fig. 4.1 Schematic of the designed probe

The detection scheme is shown in Figs. 4.1 and 4.2. Two detectors are used for measuring the light scattered from the machined surface. Light reflected specularly from the metal surface is coupled back into the GRIN lens rod through the right-angle prism and deflected onto detector 1 by the beam splitter (Fig. 4.1). Detector 2 is placed at the base of the GRIN lens rod at ~5 mm from the lens rod axis and faces perpendicular to the direction of the incident beam. The light scattered along the grazing direction (>85°) that escapes from the mouth of the bore gets collected at detector 2. In the grazing direction, a small area detector (~4 mm^2) is used to minimize detection of stray light, while for the specular direction a large area detector (~130 mm^2) is used to capture as much light as possible, since directional filtering of the specular light is already provided by the GRIN lens rod. Figure 4.2 shows the actual probe used for measurements.

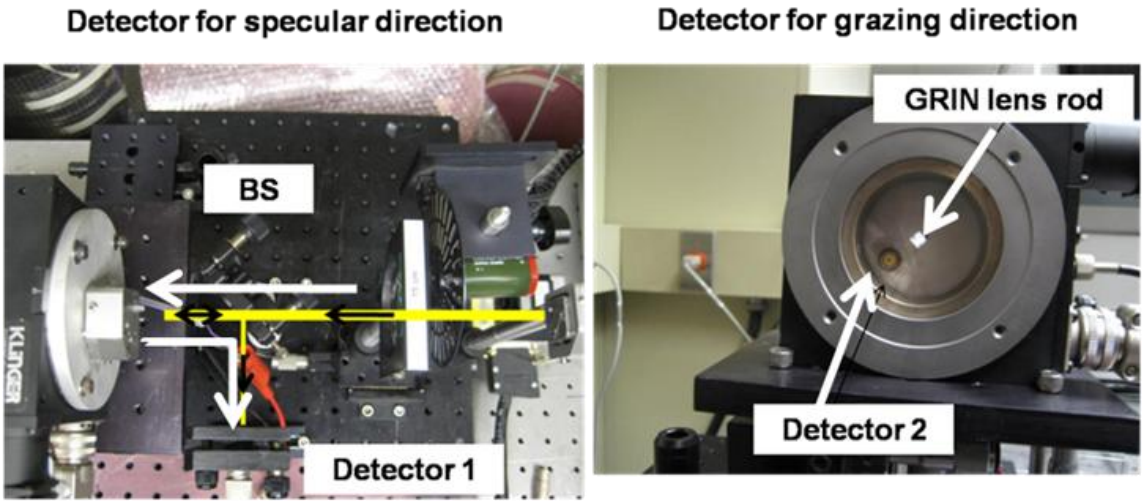

Fig. 4.2 The implementation of the probe showing detectors mounted for gathering light scattered in the specular and grazing directions from the metal surface (BS: beam splitter)

Three different kinds of samples were used in my experiments. Type I samples include surface defects on a flat metal surface (Fig. 4.3) and were used to determine distinguishing scattering signatures for porosity versus metal chips or dirt particles. Type II samples include actual spool bores in rejected transmission valve bodies detected with porosity defects obtained from Ford Motor Company (Fig. 4.4). Type III samples were used to determine the minimum detectable porosity defect by the probe. The porosity samples were made using silicon fabrication technology. The unpolished backside

surface of a silicon wafer with RMS roughness of ~0.4 μm was used to resemble a typical machined surface. Holes of different sizes ranging from 25 μm to 1 mm were etched on the surface. The inside surface of the holes was then roughened using a tungsten-carbide scribe tool to replicate the rough interiors of typical porosity defects. The entire surface was subsequently coated with Titanium metal to give it a metal finish similar to automotive parts. Figure 4.5 shows two such samples with 300 μm and 50 μm dimensions.

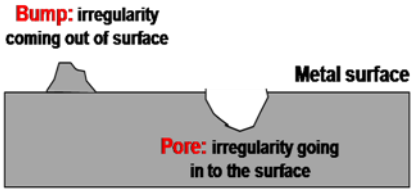

Fig. 4.3 Bump vs. porosity defect definition

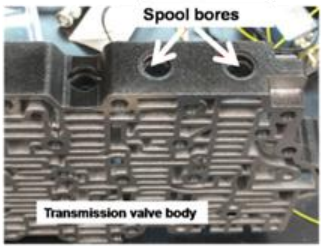

Fig. 4.4 Actual spool bores on a transmission valve body

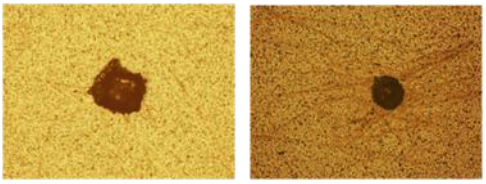

Fig. 4.5 Porosity samples fabricated on rough silicon wafer

4.2. Experimental results

In our experiments, type I samples were used to determine the distinguishing signature between porosity and metal chip or bumps. Figure 4.6(a) shows the measured intensity from a metal sample with bumps and porosity in the specular (detector 1) and grazing directions (detector 2). The results show that for near normal incident angles, the presence of both the porosity and bump leads to change in the intensity of the specularly reflected light. Thus a surface defect can be detected by monitoring the intensity of specular reflection from the metal surface. However, since the intensity drops for both the

bump and porosity, it is difficult to distinguish between defects that project out of the surface, such as the metal bump and defects such as porosity that go into the surface. The distinguishing feature in the case of bumps versus porosity, as seen in the data, lies in the grazing directions. The bumps appear as a peak in the scattered intensity, whereas the porosity leads to a valley. Each of these features stand out compared to the background fluctuations caused by the background roughness of the metal surface. The magnitude of the contrast of the defect over the background scattering fluctuations depends on the nature of each individual defect. The results were also verified to be reproducible for a number of similar defects with random surfaces as shown in Fig. 4.6(b), where the contrast of the defect feature to the background fluctuations is found to be a function of lateral dimension and the depth of the defect being measured.

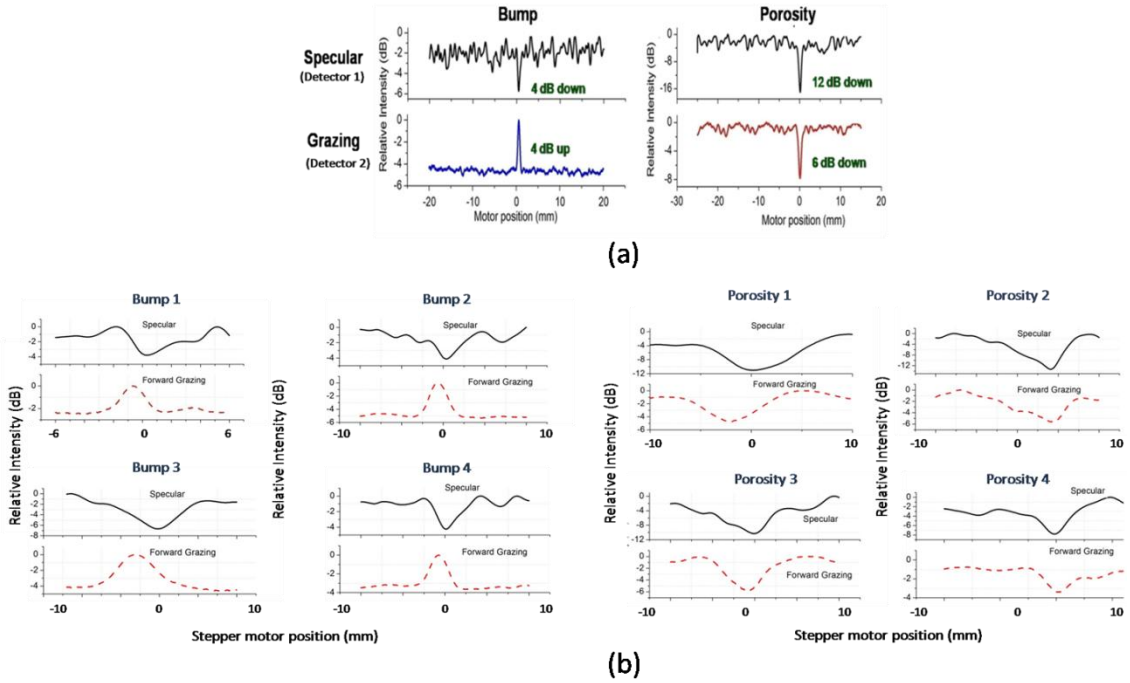

Fig. 4.6 (a) Typical type I sample results showing different scattering signatures for bump and porosity in the grazing directions (b) Reproducibility of the scattering signature for four different bumps and porosity defects on type I sample

Porosity and metal chip defects were measured inside spool bores (Fig. 4.4) of 5 mm diameter. Figures 4.7(a) and 4.7(b) show the scattered intensity from porosity and bump defects respectively, inside the spool bore of a rejected transmission valve body. The probe was manually aligned to traverse along the axis of the bore and was stepped by 50 μm along the axis of the bore and 1° angular increments, corresponding to ~45 μm steps

along the circumference of the bore. Although the probe can scan over the entire 360° range, the plot shows a 180° scan around the observed defect. The scattered light intensity from each point was measured at the two detectors in the specular and grazing directions. The plot shows the relative intensity of scattered light from the ID surface normalized to the average background intensity, with higher intensity represented by lighter shades and lower intensity by darker shades of a gray scale with 8 levels.

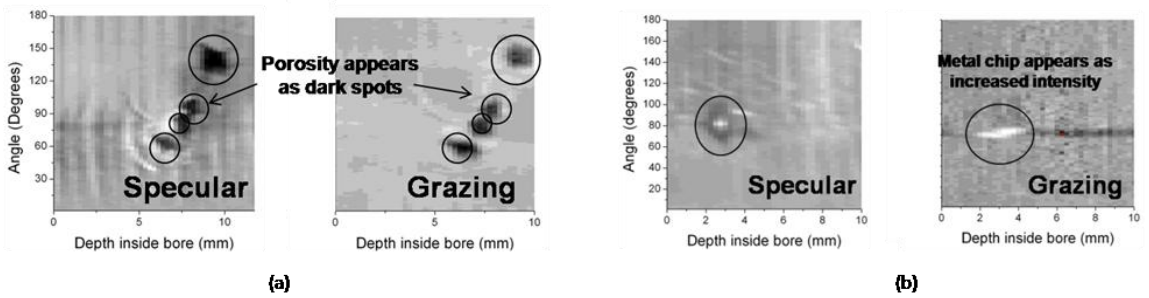

Fig. 4.7 (a) Normalized scattered intensity from a porosity defect on the inner surface of a 5 mm diameter spool bore (b) Normalized scattered intensity profile from a metal chip inside a 5 mm diameter spool bore

As can be seen in Fig. 4.7(a), porosity appears as dark spots, suggesting decrease in scattering intensity in both the specular and grazing directions. Figure 4.7(b) shows the results obtained for a metal chip inside the spool bore. In the grazing direction, the defect clearly shows up as a bright spot. The dark region on the sides of the bright spot is caused by shadowing due to the metal chip, since it protrudes out of the surface unlike porosity. Figure 4.8 shows the intensity profile in the grazing direction (det 2) for both the porosity and the metal chip. Similar to the case of flat surfaces, presence of porosity leads to decrease in scattering intensity along grazing directions and a metal chip shows up as a peak. The results confirm that the hypothesis of detecting porosity, and the ability to distinguish from bump-type defects based on the scattering signature in the grazing direction holds for a cylindrical bore geometry as well. The probe can therefore detect porosity inside spool bores, and by comparing the scattered intensity changes in the specular and grazing directions, it is possible to distinguish porosity from metal chips.

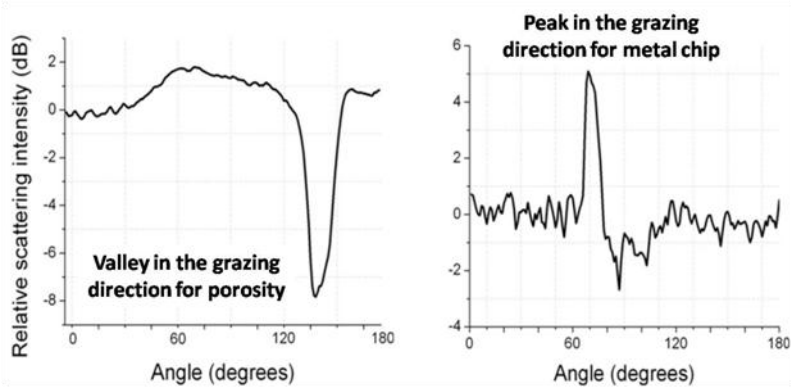

Fig. 4.8 Scattering profile in the grazing direction for porosity and bump-type defects inside a cylindrical bore

The minimum detectable porosity was determined using a range of Type III samples with varying defect sizes, fabricated as mentioned in Section 4.1. Table 4.1 summarizes the change in scattered intensity along specular and grazing directions for porosity-type defects varying from 1 mm down to 25 μm lateral size. The lateral dimension of the defect was determined by the masks used in the fabrication process, and their depth was measured using a profilometer. For the larger defects (300 μm and larger), there is greater than 6 dB of contrast to background in the specular direction and more than 5 dB of contrast in the grazing direction. In general, for the range of defect sizes measured, the contrast is observed to increase with increasing lateral dimension and depth of the defect. The data suggests that deeper defects tend to rob more power from the grazing direction. In the case of the specular direction, the change in the scattered signal is attributed to the increased roughness inside the defect. For defects down to 50 μm dimension, the contrast to the background intensity is greater than 3 dB, as seen in Table 4.1. For smaller porosity, the contrast falls to below 3 dB. The limit on the ability to detect a defect is determined by the variations in the background intensity due to the machined nature of the bores used in automotive parts. Most bores have inherent honing marks on the inner surface to help retain lubricants used to reduce friction, which invariably lead to a ripple on the background scattered intensity in the absence of defects. Misalignment of the probe with respect to the bore axis also adds to variation in the background intensity. IT is also observed that the scattered signal in the grazing direction is less sensitive to the random surface variations than in the specular direction, as can be seen in Fig. 4.6(a). Based on these observations, the threshold of defect detection is set to be 3-dB in the

grazing direction. From Table 4.1, we can see that defects with 25 µm lateral dimension and ~27 µm depth fall below the threshold in the grazing direction and hence deemed undetectable by the system. The set threshold may vary based on the factory floor setting and the background roughness of the surface under inspection. In such a case, one could expect to increase the detection threshold and be able to only detect correspondingly larger defects on the surface as suggested in Table 4.1.

Lateral size (µm)	Pore depth (µm)	Contrast in grazing	Contrast in specular
1000	**~240**	**6 dB**	**8 dB**
500	**~170**	**5.5 dB**	**6.5 dB**
300	**~140**	**5 dB**	**6.2 dB**
50	**~37**	**3.4 dB**	**3.8 dB**
25	**~27**	**2.9 dB**	**3.2 dB**

Table 4.1 Contrast to background for defect sizes ranging from 1 mm down to 25 µm

4.3. Simulation results

To verify the applicability of the demonstrated technique to most machined surfaces, simulations were performed to predict scattering patterns from an ideal reflecting surface with features resembling bump and porosity defects. In the case of calculation of scatter pattern from random surfaces, it is important to consider the roughness of the surfaces compared to the source wavelength [10]. Since the experimental samples were machined surfaces with RMS roughness on the order of few hundreds of nanometers, the Kirchhoff diffraction theory is used to model scattering of incident light at 1530 nm wavelength. In this approach, a one-dimensional surface with bump and porosity defect is used as the scattering source. The light source is assumed to be a beam with 50 µm FWHM at the scattering surface, incident at -5° to the normal to resemble near-normal incidence. The scattering pattern in the specular (3°-7°) and grazing (85°-90°) directions with respect to the normal is computed using the Fresnel-Kirchhoff's integral,

$$\left|E_p\right| = \int_x E_{inc}(x).\gamma(x).\frac{e^{-i\beta z}}{z}.dx \qquad (4.1)$$

where, the integral is computed over all points on the scattering surface. E_{inc} corresponds to the amplitude profile of the electric field of the incident Gaussian beam and z represents the distance travelled by the light wave from the source to the detector for every point on the scattering surface. β is the propagation constant and $\gamma(x)$ represents the shadow factor, which is set to 0 for the set of points on the surface that do not contribute to the scattering pattern due to absence of direct line-of-sight from the point to the detector and 1 for others.

The goal of the simulations is to determine the applicability of the proposed technique for typical polished metal samples with respect to the background surface roughness. To this effect, the relative specular and grazing scattering intensity from three identical surfaces, one without any defect, second with a porosity-type defect and third, with a bump defect, is computed for 10nm-1000nm RMS roughness of the background surface. Both the porosity and the bump are assumed to be rectangular with 300 μm each side length. The inside surface of the bump and porosity is modeled 20 times more rough than the background to resemble a defect.

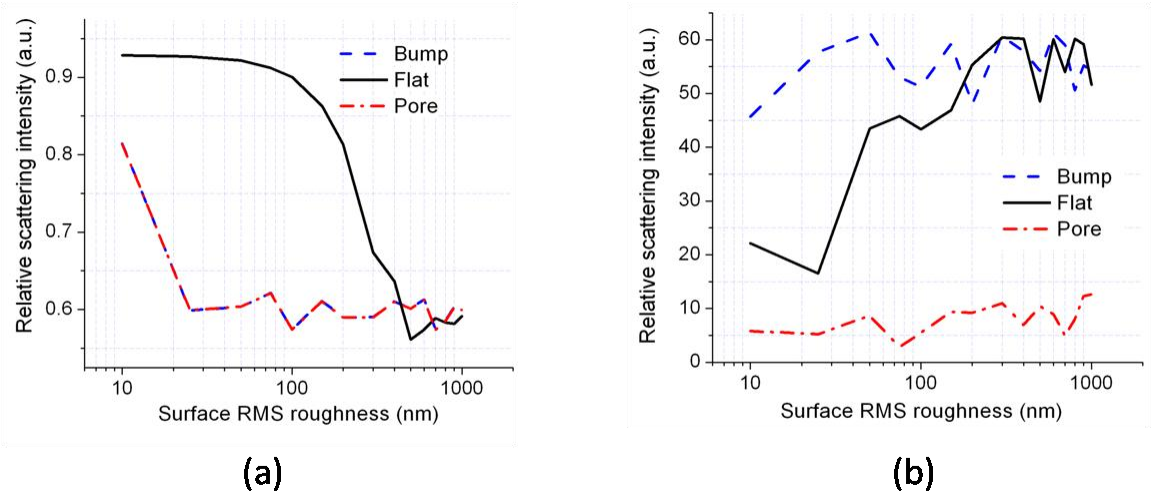

Fig. 4.9 Simulation results for relative scattering intensity in the (a) specular, and (b) grazing directions from a flat surface, metallic bump and porosity defects as a function of the RMS roughness of the background surface

The simulation results for relative scattered intensity from the three different surface types in the specular and grazing directions are shown in Figs. 4.9(a) and 4.9(b) respectively. As can be seen, a surface defect can be detected by a drop in the specular signal intensity (Fig. 4.9(a)). However, for the case of bump and pore type defects, the

scattering pattern in the specular direction is identical since the surface of the bump and the pore is the same except for the difference in height. As a result for a beam size much smaller than the defect width, the bump and pore seem identical surfaces in the specular direction.

In the grazing direction (Fig. 4.9(b)), bump-type defects show scattering patterns similar to a flat surface, thereby allowing the distinction between porosity and bump-type defects possible. The simulation results show that the technique for porosity versus bump classification in the grazing direction is applicable over a broad range of RMS surface roughness. For practically observed RMS values ranging from 0.01 to 0.8 μm for typical polished surfaces [8], the porosity should give much reduced scattering in the grazing direction compared to a flat surface or bump-type defect (Fig. 4.9(b)). For the case of bumps, as the background surface roughness becomes comparable to the inspection wavelength, 1530 nm in our case, the distinction between bump and flat reduces in both the specular (Fig. 4.9(a)) and grazing (Fig. 4.9(b)) directions. As a result, simulations suggest the probe cannot detect bumps on surfaces with RMS roughness larger than the wavelength of incident light.

4.4. Discussion

The experimental results provide evidence of the ability to distinguish between porosity and bump defects by simultaneously monitoring the change in scattering intensity along the specular and grazing directions. In the case of the metal chip inside the spool bore, the specular scattering profile consists of randomly bright and dark spots depending on the actual profile of the metal particle being inspected. However, in the grazing direction the location of the defect identifies as a bright spot, indicating an increase in scattering intensity and, hence, a bump-type defect. The porosity defects show up as dark spots in both the specular and grazing directions, thus confirming the hypothesis. The ability to distinguish between porosity from metal chips on the surface can help reduce false alarm rates in the detection scheme and at the same time increase confidence in the detected porosity by combining data collected independently from the two detectors.

The demonstrated probe can measure porosity defects down to 50 μm lateral dimension and ~40 μm depth with >3 dB contrast to the background fluctuations in

intensity. The smallest detectable defect by the system is determined by the spot size of the light beam incident on the metal surface. In my experiments, the smallest spot size is ~50 μm, determined by the choice of the focusing lens in the system. A 50 mm focal length lens was chosen to provide a Rayleigh range of 5 mm to suit the varying diameters of the spool bores in typical transmission valve bodies. Smaller defect sizes can be detected by using a tighter focal length lens. For example, a GRIN lens rod based endoscopic probe has been demonstrated in the past with spot sizes as small as 11 μm [11]. However, a tighter focus also leads to higher sensitivity of the specularly reflected light intensity to misalignment of the probe from the cylinder axis. I could not determine the influence of defect depth on contrast to background due to lack of multiple samples with similar lateral dimensions and different depths.

The observed experimental results shown in Fig. 4.6(a) for defects on a flat metal surface are in agreement with the simulation results. The RMS roughness of the metal sample used in the experiments is measured to be ~93 nm, averaged over five different points. At this RMS value, simulations for the grazing direction (Fig. 4.9(b)) indicate a decrease in scattered light intensity for the pore and increased intensity for the bump compared to a surface with no defect, similar to the observed experimental results.

Even though the demonstrated porosity detection system is used to measure porosity inside spool bores of transmission valve bodies, bores in the range of 5-15 mm diameter on a number of other manufacturing parts such as steering gears, fuel injection systems, etc. can also be inspected using this technique.

The amount of power required for reliable defect detection is determined by the sensitivity of the detector placed in the grazing direction, due to the weak nature of scattering in the grazing direction from most polished surfaces. The amount of light scattered in the grazing direction in turn depends on the RMS roughness of the surface under inspection. All the experimental samples had RMS roughness values on the order of 0.1 μm, and light signal scattered in the grazing direction were consistently observed to be ~20 dB lower than the specular signal. As a result, for a detection sensitivity of -24 dBm (Noise equivalent power = ~4 μW), the signal source needs to be >5 mW to have a signal-to-noise ratio greater than 10 dB at the grazing angle detector. For inspection of smoother surfaces, higher laser powers would be required to maintain the large signal-to-

noise ratio and calibration runs could be performed to adjust the signal level, based on the roughness of the each individual bore.

For potential in-line implementation, the system can incorporate faster mechanical and data acquisition schemes. Ball and screw type actuators can achieve rotation speeds of up to 4000 rpm and with data acquisition systems sampling at 15 ksamples/second, the inner circumference of a 20 cm long and 10 mm diameter bore can be inspected in 20 seconds with a circular spot resolution of 150 μm diameter. Since optical detectors in the 1550 nm region are available with down to nanoseconds of response times, the inspection speed limitation of the probe is expected to be primarily mechanical. For example, with a 100 kHz bandwidth detector, the probe would have to rotate at >9600 rpm to be unable to detect a change in intensity, while traversing a 50 μm diameter spot.

The 360° rotation of the probe about its axis can complicate the mechanical design of the system, including the coupling of the electrical and optical signals in high speed in-line systems. In my design, the mechanical motion of the GRIN lens rod and the delivery optical fiber are decoupled by using free space coupling into the lens rod rotating about its axis. The electrical signal coupling however, would require a slip ring type of arrangement to maintain electrical contact with the data acquisition system in the set-up. In terms of structural stability, the probe used in the experiments has a length of ~15 cm, which limits the depth of penetration inside transmission valve bodies to about 10 cm. For measurement of deeper bores up to 21 cm in transmission valve bodies, two or more GRIN lens rods would have to be cascaded with anti-reflection coatings on the end faces. A longer probe will reduce the resonance frequency of vibrations of the rod [12], and require more careful mechanical design. For example, the resonant frequency for a 21 cm long and 2.7 mm diameter circular glass rod with a typical Young's modulus of 50 GPa and a density of 2800 kg/m^3 is ~6000 rpm, which would be the upper limit of operation speed for the probe.

The demonstrated probe gathers scattering information from the surface under inspection in the specular and grazing directions to detect defects and classify them as porosity versus bump-type defects. Such qualitative distinction provides information that is important to reduce the false alarm rates for in-line inspection systems operating on the plant floor, which cannot be achieved by 2D imaging based systems. Based on the

simulation results, porosity defects can be detected on the surface over a broad range of surface RMS roughness encountered in automotive machined parts. However, at surface roughness comparable to the wavelength of the incident light, the signature associated with the detection of bump-type defects is expected to disappear. In cases where bump-type defect detection on rough surfaces is required, a longer wavelength light source can be used.

4.5. Summary

In this chapter, I have demonstrated a standard SMF based novel optical probe for detection of porosity inside bores down to 5 mm diameter. The probe uses a GRIN lens relay rod to focus a beam of near-infrared laser light, and surface defects are detected based on the change in the scattering intensity due to the high spatial coherence of the incident beam. Based on the difference in the scattering signatures in the specular and grazing directions, I have shown that the probe can distinguish between bumps versus porosity type defects. For both the porosity and bump-type defects, there is reduced scattering in the specular direction making them difficult to distinguish using a single detector. However, in the grazing direction, the porosity and bump provide different signatures and can be distinguished. We also tested the set-up for defect sizes ranging from 1 mm down to 25 μm and confirmed detection of defects down to ~50 μm lateral dimension and ~40 μm deep with greater than 3-dB contrast to the background intensity fluctuations.

Inspection of bores in power train parts is of importance to prevent malfunction and early breakdown of mechanical systems. Challenges to porosity detection include difficulty to inspect small bores down to 5 mm diameter and that 100% parts inspection is time-consuming and expensive. The designed probe can detect porosity and distinguish from bump type defects due to metal chips, thereby reducing the chances of false alarms. The probe is less than 4.5 mm in diameter and can be up to 21 cm long, making it suitable for inspection of a variety of automotive parts such as fuel injection systems, transmission valve bodies and engine cylinder parts where effective sealing surfaces are important and surface defects such as porosity affect quality of manufacturing.

References

[1] Herbert E. Merritt, *Hydraulic control systems*, (*Wiley-Interscience*, 1967)

[2] I. Menzies, P. Koshy, "In-process detection of surface porosity in machined castings," International Journal of Machine Tools & Manufacture, **49**, 530-535 (2009)

[3] E. Hong, R. Katz, B. Hufnagel, J. Agapiou, "Optical method for inspecting surface defects inside a small bore," Measurement Science and Technology, **21**(1), 5704 (2010)

[4] Y. Q. Fu, C.H. Ji, A. W. Batchelor, N. H. Loh, "X-ray imaging of metal injection moulding parts," Journal of Materials Science Letters, **16**, 1873-1875 (1997)

[5] H. K. Tonshoff, I. Inasaki (Eds.), *Sensors in manufacturing*, (Wiley-VCH Verlag GmbH, Weinheim, 2001)

[6] D. Steiner, R. Katz, "Measurement techniques for the inspection of porosity flaws on machined surfaces," Journal of Computing and Information Science in Engineering, **7**, 85 (2007)

[7] G. Biegelbauer, M. Vincze, "3D vision-guided bore inspection system," Proceedings of the Fourth IEEE International Conference on Computer Vision Systems, 2006

[8] American National Standard, ASME/ANSI B46.1-1985, Surface Texture (American Society of Mechanical Engineers), New York, 1985

[9] T.V. Vorburger, E. Marx, T.R. Lettieri, "Regimes of surface roughness measurable with light scattering," Applied Optics, **32**(19), 3401 (1993)

[10] John C. Stover, "Scatter calculations and diffraction theory," Chap. 3 in Optical Scattering: Measurement and Analysis, McGraw-Hill Inc. (1990)

[11] T. Xie, S. Guo, Z. Chen, D. Mukai, and M. Brenner, "GRIN lens rod based probe for endoscopic spectral domain optical coherence tomography with fast dynamic focus tracking," Optics Express, **14**, 3238-3246 (2006)

[12] A.I. Munitsyn, "Nonlinear bending vibrations of a rotating rod," Journal of Machinery Manufacture and Reliability, **37**(2), 110-113 (2008)

Chapter V

Summary and future work

5.1 Optical probe for porosity detection in bores

In the previous chapter, I have demonstrated a novel scattering based porosity detection system for defect inspection on the inner surfaces of bores down to 5 mm diameter. The technique uses scattering along the grazing and specular direction from the surface under inspection in a very tight geometrical space to not only detect defect, but also provide classification information on the depth of the defect. This is of significance in practical implementation of defect detection systems on the plant floor, since false alarm-rates can be reduced. For example, in most 2-D imaging approaches to defect detection, due to lack of any depth information on an encountered surface anomaly, even metal chips or detergent particles as a result of the manufacturing process gets classified as a defect.

High rate of occurrence of false alarms deters the implementation of 2D systems for inline applications [1]. Also, manual inspection is tedious for the case of parts such as transmission valve bodies where small diameter bores of up to 20 cm length make visual inspection difficult and unreliable. As a result, currently no inline inspection technique for porosity detection in transmission valve bodies exist and a human inspection on sampled parts is practiced [2]. This approach has drawbacks since porosity defect occurrences are random and due to the high required quality on parts specifications, detection of porosity on the sampled part leads to rejection of the entire batch without individual part inspection [3]. Conversely absence of porosity on the sampled part does not guarantee quality of the non-sampled parts and hence 100% inline inspection can greatly improve the reliability of the manufacturing process. In addition, occurrence of porosity defects is high during the ramp-up time of casting processes and ~5% output of

every manufacturing cycle are initially discarded without inspection [3]. An inline technique can help better understand the ramp-up process and help reduce the wastage associated with lack of such inspection tools.

Using the designed probe, I have demonstrated ability to detect porosity defects down to ~50 μm lateral dimension. Typical requirements on acceptable defects are currently estimated at ~500 μm [3]. In comparison, my system could detect defects ~10 times smaller. If such resolution is not required, the field of view of the probe while measuring a single pixel can be increased thus increasing the speed of inspection of the system. Currently estimated required inspection time for a single part is ~20 s [2]. Specific improvements required for increasing the speed of inspection in the assembled probe to meet inline implementation requirements are as described in the discussion section of Chapter 4. In addition, given the large number of bores in a single part, inspecting multiple bores simultaneously would be required. A proposed system to achieve this end is shown in Fig. 5.1, where the part is held stationary, while multiple probes move in and out of the bores for quick inspection of the part. To speed up the travel time and rotation of the probe, better mechanical stages than those used for the prototype demonstration will be required.

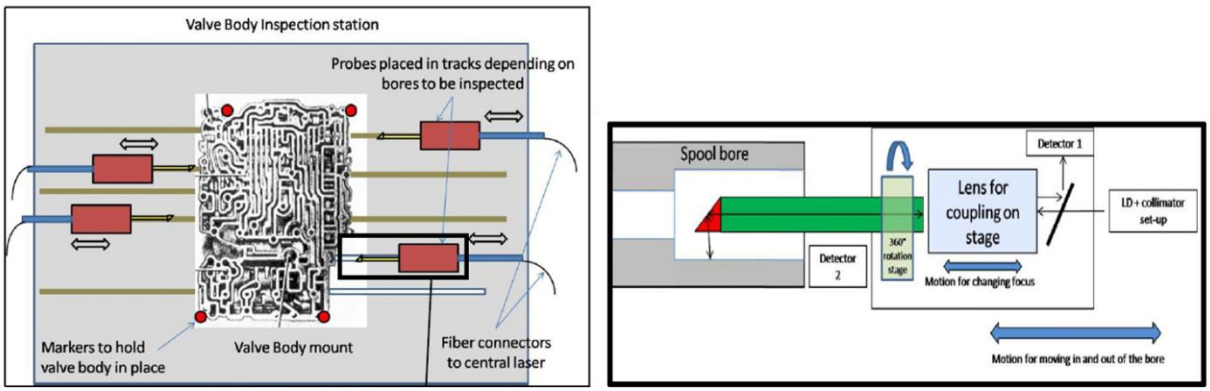

(a) (b)

Fig. 5.1. (a) Envisioned valve-body inspection station, (b) Individual probes will consist of rotation and motion stages with light coupled through fiber

5.2 Higher efficiency mid-IR Supercontinuum Generation

The main focus of my thesis work has been in the generation of mid-infrared supercontinuum laser (MISCL) with higher efficiency. The approach used in my work is

based on modulation-instability initiated spectral broadening starting from near-IR telecommunication wavelengths.

In the Tm-based MISCL system demonstrated in my thesis, the initial motivation for switching from a Er:Yb-based power amplifier stage to a Tm-based final amplification stage was largely influenced by two factors. First, by shifting the pump of the SC generation process from 1.55 to ~2 μm, extension in the long wavelength edge can be expected in the nonlinear medium. Secondly, Tm-amplifiers have been demonstrated to achieve higher pump-to-signal conversion efficiencies compared to Er:Yb amplifiers. For example, slope efficiencies of ~56% have been achieved with large mode area Tm-doped gain fibers [4] compared to only ~38% slope efficiency for Er:Yb co-doped gain fibers with similar geometry [5] operating in continuous-wave master-oscillator power amplifier configuration.

Advantage in terms of higher efficiency in mid-IR light generation has been demonstrated through both of these factors in the generation of wavelengths beyond 3.8 μm with ~2.5 times higher optical efficiency than Er:Yb systems. In addition, several other benefits are also provided by the system from a practical system implementation stand point.

1. Shorter length of ZBLAN fiber (~8.5 m) required for ~0.5 W light generation in wavelengths 3.8 μm compared to Er:Yb based systems (>12 m) [6].
2. Due to a large wavelength separation between the pump and the signal wavelengths in the Tm-doped power amplifier stage, backward pumped amplifier configuration is implemented without apparent damage to the 790 nm pump lasers from high peak power 2 μm light leaking into the pump ports. In the Er:Yb case, additional 1.55 μm wavelength blocking filters are required to prevent damage to the 976 nm pump diodes.
3. Higher long wavelength generation efficiency results in operation of the system at an overall lower average power in the power-amp stage. For example, in the Er:Yb system, ~55 W of average pump power is required at the gain fiber to pump-combiner fiber splice for generating 0.5 W in wavelengths beyond 3.8 μm [6], compared to ~23 W for the Tm-based MISCL. The lowering of the system average

power results in the ease of requirements on the quality of the splice between the pump combiner to gain fiber.

4. The 25 μm large mode area core diameter gain fibers are commercially available for Tm-systems, whereas only 15 μm core Er:Yb co-doped fibers are available [7]. The larger core diameter allows for lower nonlinearity in the Tm-doped power amplifier and increases the threshold of saturation effects in the amplifier.
5. Lower nonlinearity also allows for possibility of forward pumping in the power amplifier and reducing the thermal load on the gain fiber to output pump combiner fiber splice.
6. Higher long wavelength generation efficiency with respect to the SC pump also means lower required average powers at the output of the power amplifier stage for the mechanical splice from the fused silica to ZBLAN fiber. For example, for 0.5 W light generation beyond 3.8 μm, only ~8 W of average power output from the Tm-amplifier is required compared to ~13 W from the Er:Yb stage [6]. The lower power should lead to more thermal stability of the mechanical splice.
7. By switching the amplifier system, the chain of increasing spontaneous emission in the output is broken and the ASE source in the system is reset.

In the new Tm-based MISCL system, a novel demonstration of splitting of the SC generation process is used to generate mid-IR SC in two distinct nonlinear broadening stages compared to previously demonstrated MI-based systems (Fig. 5.2). First, in low near-IR loss standard fused silica SMF, moderately amplified 1.55 μm laser diode pulses are used for SC generation beyond 2.1 μm. Compared to other pulsed 2 μm sources, the demonstrated wavelength shifting approach using standard SMF is also attractive due to its open-loop operation configuration. Starting the SC generation process from 1.55 μm eliminates the need for 2 μm fiber coupled components such as DFB, isolators, WDMs, etc. which are currently customized products and expensive.

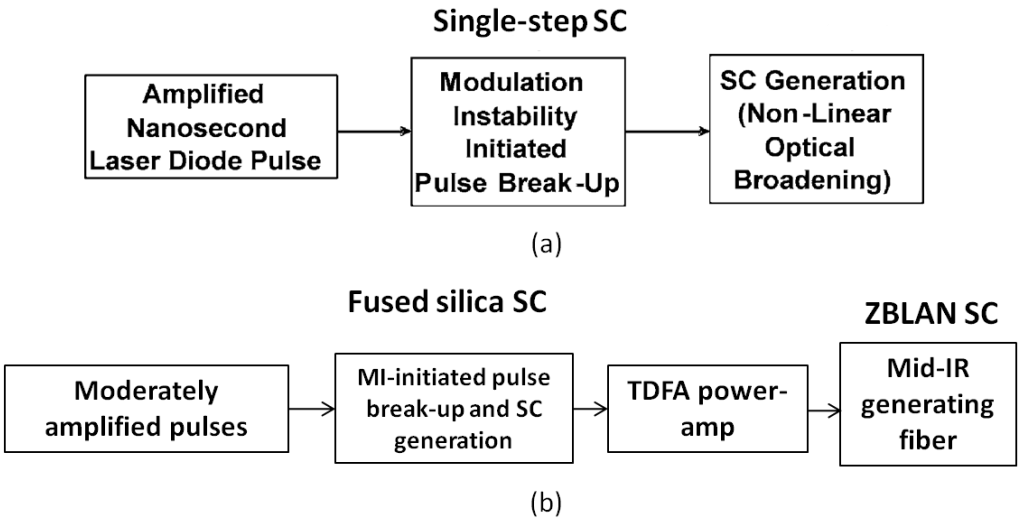

Fig. 5.2. (a) Previously demonstrated single-step SC architecture based on MI-initiated pulse break-up followed by nonlinear broadening, (b) Novel two-step SC generation architecture using Tm-based fiber amplifiers

In terms of electro-optic conversion efficiency of the pump lasers used in the power amplifier stages, Er:Yb systems have a slight advantage currently due to the maturity of processing of InGaAs quantum wells over the years. 976 nm pump lasers fiber coupled in to 100 µm core fibers with ~46% electro-optic conversion efficiency are commercially available currently [9]. In comparison, 790 nm pumps with typically 39-41% electro-optic conversion efficiency were used in my experiments. The relatively lower efficiency of 790 nm diodes is attributed to the higher intrinsic photon energy and material-related issues of comparatively newer InGaAsP fabrication [8]. However, with interest in high power 2 µm Tm-based systems pumped at 790 nm, pump diode technology should catch up with state-of-the-art performance from 976 nm diodes. Another disadvantage of 790 nm pump lasers from a practical standpoint is the higher current requirements for these lasers. For example, the 790 nm pumps need ~50 A current for generating 35 W pump power output coupled in to a 100 µm core fiber compared to ~12 A required for commercially available 976 nm pumps. Such disparity arises possibly from the electrical connection of the laser bars inside the pump package. The higher current requirement needs additional circuitry to protect the pumps from damage due to rapidly switching high currents as demonstrated in my experiments.

Future work:

I have demonstrated mid-IR SC generation with ~9% optical efficiency in conversion from the 790 nm pump to the mid-IR output with ~2.35% efficiency in generation of wavelengths beyond 3.8 μm. However, there exists some scope of further improvement in the efficiency of the Tm-based MISCL system and are discussed as possible future work.

Higher repetition rate scaling: The efficiency of the system can be increased by operating at higher pulse repetition rates due to higher 790 nm pump power in the system. Also the duty cycle of the input pulses increases with increase in system repetition rate leading to lower losses of the 790 nm pump to spontaneous emissions in the amplifier. Both factors combined, still higher efficiency in mid-IR SC generation should be possible in the Tm-based MISCL.

It is important to note that higher pulse repetition rate would also require system operation at higher average powers. Hence better cooling and thermal management schemes need to be implemented in the system. One approach to keeping the thermal load in the system within the current levels is to reduce the duty cycle of the pump modulation signal. Currently, the system operates at 50% modulation duty cycle of the pumps at 500 kHz repetition rate. By doubling the repetition rate to 1 MHz and simultaneously reducing the pump modulation duty cycle to 25%, similar average powers can be maintained in the system while making the amplifier more efficient through increase of the pulse repetition rate. This would require more pumping power in the system than currently available and electronics to adjust the duty cycle of the modulation signal to the pump drive circuit.

Fused silica to ZBLAN splice: In my experiments, I have used a mechanical splice to couple light output from the TDFA in to the ZBLAN fiber. Such a scheme results in a coupling loss of ~45%, which is a large fraction of the current system inefficiency. Recently, some preliminary work has been demonstrated in [10] with fused silica to fluoride fiber mechanical splices with losses as low as 0.8 dB at 1550 nm. Such a scheme uses a CuAlBe alloy shape memory connector to hold the ZBLAN and fused silica fibers butted against each other, while maintaining low coupling losses. Incorporation of such a

splice would increase the efficiency of the system by ~1.3 times. The high power handling capability of such a splice would have to be tested before implementing it in the MISCL system.

The mechanical splice loss is also currently high due to the mode mismatch between the fused silica and ZBLAN fibers used in my experiments. The 2 μm light at the output of the 10 μm core, 0.15 NA fused silica fiber has a mode-field diameter of ~11 μm and yields higher coupling losses in to a 8 μm core, 0.27 NA ZBLAN fiber. The loss can be reduced by using larger core ZBLAN fibers. For example, fibers with ~10 μm core diameter can be tested to achieve lower coupling losses from the fused silica to ZBLAN fiber through better matching of the 2 μm fundamental mode in either fibers. However, a trade-off exists whereby increasing the fiber core diameter results in an increase in the fiber cut-off wavelength, all other parameters remaining the same, and would result in higher levels of multi-moded behavior in the fiber at ~2 μm.

Large-mode area fiber splicing: In my experiments, a two-arc fusion splicer was used to splice the 25/250 μm core/cladding diameter gain fiber to geometrically patched passive fibers on the combiner/mode adapter. An estimated splice loss of ~0.6 dB is observed by optimizing the splice time and current. The two-arc splicer does not typically do not provide much control on the splicing conditions with similar splice quality over a range of splice parameters. In addition, the Tm-gain fiber achieves large mode area operation by using a high refractive index pedestal layer, which makes the splice to the combiner fiber typically lossy. The poor quality of the splice degrades the system performance in a couple of ways: a) in the power handling capability of the splice and, b) in the degradation of the single mode beam quality of the 2 μm light in the 25 μm fiber core.

By using more sophisticated equipment and better splice recipes, lower loss and better quality splices can be achieved. For example, in the case of the Er:Yb based MISCL system, ~1.25 times higher amplifier efficiency was achieved by optimizing arc power and time parameters of the splice. In addition, better quality splices are expected by offsetting the splicing arc away from the gain fiber [11].

Higher nonlinearity fiber: In the Tm-based MISCL system, mid-IR light generation is achieved to ~4.5 μm. The long wavelength edge of the generated SC is limited by the

properties of the ZBLAN fiber (material loss and mode-field dispersion). At wavelengths beyond 4.5 μm, the loss in the ZBLAN fiber increases to beyond ~1 dB/m and mode-field diameter increases to above 12 μm. As a result, the Raman gain generated by the ZBLAN fiber at these wavelengths cannot compensate for the linear loss in the fiber and SC generation process ceases to generate longer wavelengths.

Longer wavelength generation is possible using higher nonlinearity fibers such as tellurites. Particularly, a photonic crystal fiber with ~1.7 μm^2 mode area and ~10x higher Raman gain coefficient [12]. Using ~17 kW peak power pulses at 1.55 μm, SC generation out to 4.8 μm has been demonstrated in just 0.8 cm length of the fiber [13]. The higher Raman gain coefficient allows for using small lengths of the tellurite fiber and hence the long wavelength edge is not expected to be limited by the material absorption.

Some concerns about implementing a tellurite PCF include the limitation of results with tellurite fibers to low average powers. Only up to ~1.2 W of average output power has been demonstrated to date with tellurite fibers indicating difficulty in achieving high quality fiber fabrication [14].

Cascaded SC generation: The demonstrated Tm-based MISCL results confirm the ability to cascade nonlinear media separated by wavelength-offset amplifier stages to sustain longer wavelength generation. Particularly in the mid-IR, with emergence of Er-doped ZBLAN fibers pumped at 976 nm for 2.7-3 μm light amplification [15], a similar architecture can be implemented for long wavelength generation in ZBLAN by shifting the SC pump further to around 2.7 μm. This can lead to further extension of the long wavelength generation efficiency and allow for higher power scaling in the wavelength range beyond 3.8 μm based on improvements in the Er-doped ZBLAN fiber performances.

5.3 Broadband surface-normal optical modulator

One application of a broadband supercontinuum light source spanning several hundred nanometers in wavelength is the ability to provide higher throughput in communication systems. For example, in the case of wavelength-division multiplexed (WDM) optical networks, each user is assigned a separate wavelength channel for communication allowing for parallel communication pathways on a single physical medium such as fiber

or free-space. Another advantage of WDM systems is the variable speed and transparent operation of users with respect to others on the network eliminating any bottlenecks in the system due to the presence of a large number of users. However, implementing WDM networks is expensive due to the requirement of dedicated components for every channel in the system. For instance, on a network with 12 channels, 12 different wavelength light sources are required along with components such as filters and WDMs for the specific wavelength channel to prevent any cross-talk between users. Hence WDM systems are typically implemented only in the long-haul sections where higher component costs can be justified.

One technique to implement WDM networks on the end-user level is the implementation of architectures with cost-shared components [16]. For example, by replacing the light source with a broadband single supercontinuum laser, the need for individual lasers can be eliminated. The system would still requires devices at the end-user premise for relaying information back to the central office without requiring wavelength specific equipment at the user end. Such systems are termed as colorless optical networking units and can help increase the throughput, while reducing the component cost in the system.

In my thesis, I have demonstrated a colorless modulator for application in a broadband light source based WDM network. The modulator operates over 1200 nm wavelength range with surface-normal geometry for easy coupling of light into the device and potentially low fabrication costs. The modulator is passive and based on a non-resonant free-carrier effect in semiconductors with wavelength properties largely determined by the optical characteristics of the anti-reflection coating. Hence it can be suited to most wavelength ranges in the near-IR for telecommunication applications, or the near-IR (1.7 μm) and mid-IR (2-2.4 μm) free-space communication windows.

Operation in conjunction with a supercontinuum laser was demonstrated in my experiments with the fabricated modulator as a probable application for SC lasers in broadband communication system. However, there are several shortcomings that need to be overcome before such systems can be practically implemented. Firstly, the pulse profile at the output of the SC source is largely noisy and hence higher penalty in terms of bit-error rates could be encountered. Secondly, the high peak power used in the pulse

generation can lead to higher nonlinear effects during propagation through the medium and lead to inter-channel cross-talk. Also, the demonstrated properties of the modulator are not up to the current telecommunication equipment standards. For example, a contrast ratio of only ~43% was demonstrated for the GaAs-based modulator and an insertion loss of ~4-dB is measured in the device. Improving the performance of the modulator requires substantial improvement in the fabrication methodology and higher fabrication costs as discussed in Chapter 3. For example, the insertion loss can be reduced by using a semi-insulating substrate in fabrication, which would require additional fabrication steps. The modulation depth can be improved by increasing the thickness of the intrinsic layer, which would increase the epi-wafer cost. Also, the theoretically predicted modulation bandwidth for the GaAs-based modulator is ~450 MHz, and is limited by the RC-time constant of the device diffusion capacitance, which serves as a trade-off between higher modulation depths and speeds.

One approach to using SC sources in a communication system would be to tailor the pulses so as to generate a broad continuum extending 100-200 nm in a single pulse [17]. In conjunction with the demonstrated surface-normal modulator, a potentially low-cost, higher capacity system implementation with few MHz bandwidth can be implemented in a fiber-based system. The key advantage of the system would be the larger number of users and hence lower cost per user.

To conclude, I have demonstrated three optical systems as part of my PhD thesis with applications in different fields ranging from communication to spectroscopy to metrology of automotive parts. Particularly in the field of defect inspection, the demonstrated probe can help improve the quality standards of automotive parts manufacturing using non-contact, inline parts inspection. In the case of mid-IR light sources, by achieving higher optical conversion efficiency, SC lasers can rise to the forefront of mid-IR applications with their ability to generate several octaves of wavelength simultaneously. With a thorough analysis through simulations and extensive experiments, I believe both these technologies can serve as disruptive solutions for future applications.

References

[1] Discussion with *Ghazi Rayes*, Manufacturing Engineer at Ford Motor Company ATO plant

[2] Discussion with *Gordon Scudder*, Process Engineer at Ford Motor Company, Van Dyke Transmission plant

[3] Discussion with *Dwight Carlson*, Founder, Chairman and CEO of Coherix, Inc.

[4] G. P. Frith and D. G. Lancaster, "Power scalable and efficient 790-nm pumped Tm^{3+}-doped fiber lasers", Proc. SPIE 6102, 610208 (2006)

[5] A. Carter, J. Farroni, K. Tankala, B. Samson, D. Machewirth, N. Jacobson, W. Torruellas, Y. Chen, M. Cheng, A. Galvanauskas, and A. Sanchez, "Robustly Single-Mode Polarization Maintaining Er/Yb Co-Doped LMA Fiber for High Power Applications," in Conference on Lasers and Electro-Optics/Quantum Electronics and Laser Science Conference and Photonic Applications Systems Technologies, (Optical Society of America, 2007), paper CTuS6

[6] M. Kumar, V. Alexander, M. J. Freeman, M. N. Islam, F. L. Terry, Jr., in preparation, 2011

[7] Nufern website (http://www.nufern.com/whitepapers.php)

[8] J. Wang, L. Bao, M. DeVito, D. Xu, D. Wise, M. Grimshaw, W. Dong, S. Zhang, C. Bai, P. Leisher, D. Li, H. Zhou, S. Patterson, R. Martinsen and J. Haden, "Reliability and performance of 808nm single emitter multi-mode laser diodes," white-paper by *n*Light Corp., WA, USA

[9] IPG Photonics website (http://www.ipgphotonics.com/09_micron_diodes.htm)

[10] D. Faucher, A. Fraser, P. Zivojinovic, X. P. Godmaire, É. Weynant, M. Bernier, and R. Vallée, "High power handling shape memory alloy optical fiber connector," Appl. Opt. 48, 5664-5667 (2009)

[11] Discussion with *Clyde Troutman*, Engineering Manager, 3SAE Technologies, Inc.

[12] M. D. O'Donnell, K. Richardson, R. Stolen, C. Rivero, T. Cardinal, M. Couzi, D. Furniss, A. B. Seddon, "Raman gain of selected tellurite glasses for IR fibre lasers calculated from spontaneous scattering spectra," Optical Materials, Volume 30, Issue 6, February 2008, Pages 946-951

[13] P. Domachuk, N. A. Wolchover, M. Cronin-Golomb, A. Wang, A. K. George, C. M. B. Cordeiro, J. C. Knight, and F. G. Omenetto, "Over 4000 nm bandwidth of mid-IR supercontinuum generation in sub-centimeter segments of highly nonlinear tellurite PCFs," Opt. Express **16**, 7161-7168 (2008)

[14] K. Li, G. Zhang, L. Hu, "Watt-level ~2 μm laser output in Tm^{3+}-doped tungsten tellurite glass double-cladding fiber," Opt. Letts., Vol. 35, No. 24, 4136-4138, (2010)

[15] S. Tokita, M. Murakami, S. Shimizu, M. Hashida, S. Sakabe, "Liquid cooled 24 W mid-infrared Er:ZBLAN fiber laser," Opt. Letts., Vol. 34, No. 20, 3062-3064, (2009)

[16] N.J. Frigo, P.P. Iannone, P.D. Magill, T.E. Darcie, M.M. Downs, B.N. Desai, U. Koren, T.L. Koch, C. Dragone, H.M. Presby, and G.E. Bodeep, "A wavelength-division multiplexed passive optical network with cost-shared components," IEEE Photon. Tech. Lts., Vol. 6, No. 11, November 1994

[17] C. Xia, M. Kumar, M. –Y. Cheng, O. P. Kulkarni, M. N. Islam, A. Galvanauskas, F. L. Terry, Jr., M. J. Freeman, D. A. Nolan, W. A. Wood, "Supercontinuum generation in silica fibers by amplified nanosecond laser diode pulses," IEEE J. of Sel. Top. In Quant. Elect., Vol. 13, No. 3, May/June 2007